Probing Operando Mixed Ionic/Electronic Transport in Conjugated Polymers: From Molecular Level to Device Performance

Jiajie Guo

A dissertation

submitted in partial fulfillment of the

requirements for the degree of

Doctor of Philosophy

University of Washington

2023

Reading Committee:

David S. Ginger, Chair

Samson A. Jenekhe

Bo Zhang

Program Authorized to Offer Degree:

Molecular Engineering

University of Washington

Abstract

Probing Operando Mixed Ionic/Electronic Transport in Conjugated Polymers:
From Molecular Level to Device Performance

Jiajie Guo

Chair of the Supervisory Committee:
David S. Ginger
Department of Chemistry

Mixed ionic-electronic transport in conjugated polymers significantly impacts the performance of organic electronics, ranging from organic electrochemical transistors (OECTs) to next-generation neuromorphic computing architectures. The exceptional performance of conjugated polymers in these applications stems from their remarkable ability to efficiently accommodate counterions throughout the entire device volume during electrochemical redox processes. The dynamic changes in the electrical and chemical environment that occur during this process necessitate the utilization of operando characterization. In this dissertation, we present a series of comprehensive studies employing operando measurements to probe the intricacies of mixed ionic-electronic transport in OMIECs and their direct impact on device performance. First, we delve into the

molecular-level structural changes of a n-type ladder OMIEC material upon the electrochemical process and found a unique mechanism which might provide crucial insights into next generation material design. Next, we focus on comprehending the switching dynamics of OECTs and identifying the speed limitations. Through this investigation, we explain the asymmetric accumulation mode OECTs switching behavior, which cannot fit in existing models. Also, we gain valuable knowledge on the interplay between electronic and ionic transport, shedding light on potential strategies for optimizing OECT switching characteristics. Finally, we target the root sources of OECT degradation over repeated cycling. With the operando tools, we decouple the contribution from ionic and electronic transport to the degradation. Together, our research highlights the power of operando characterization in unveiling the fundamental processes of mixed ionic-electronic transport and providing valuable insights for application-oriented molecular design and device optimization.

TABLE OF CONTENTS

LIST OF FIGURES

LIST OF TABLES

ACKNOWLEDGEMENTS

First and foremost, I am deeply thankful to my advisor, Dr. David S. Ginger, for his unwavering guidance, mentorship, and encouragement throughout this research journey. His expertise, patience, and dedication have been instrumental in shaping the direction of this work and fostering my academic growth.

I extend my sincere appreciation to the members of my dissertation committee, Dr. Samson A. Jenekhe, Dr. Bo Zhang, and Dr. Bruce J. Hinds, for their valuable insights, constructive feedback, and critical evaluations that have greatly enriched the quality of this research.

I am also indebted to my lab mates, Dr. Rajiv Giridharagopal, Dr. Lucas Q. Flagg, Dr. Connor G. Bischak, Dr. Dean A. Waldow, Shin Ya Emerson Chen, and Ramsess Quezada, for their camaraderie, stimulating discussions, and willingness to lend a helping hand whenever needed. Your support and collaborative spirit have made this research experience truly enjoyable and rewarding.

I am profoundly grateful to my dear friends Wenjia, Fangyuan, Kiki, Victoria, Junxi, Huiyun, Rene, Xudong, Hao, and many others, who have been by my side throughout this journey. Your presence has made a world of difference, and I am incredibly blessed to have you in my life.

Last but not least, I am immensely grateful to my family for their unwavering love, understanding, and encouragement throughout this challenging academic pursuit. Their constant support and belief in my abilities have been a source of strength and motivation. Without their unwavering encouragement, this accomplishment would not have been possible.

Chapter 1. INTRODUCTION

1.1 BACKGROUND AND MOTIVATION

Organic electronics have emerged as a compelling alternative to traditional inorganic semiconductors due to their unique properties, such as solution processability, mechanical flexibility, tunable characteristics, lightweight, and low cost. These features make organic semiconductor materials highly attractive for a wide range of applications, including organic light-emitting diodes (OLEDs), organic photovoltaics (OPVs), organic field-effect transistors (OFETs), organic electrochemical transistors (OECTs), and more recently, neuromorphic computing architectures.

A remarkable family of organic semiconductor materials is called organic mixed ionic-electronic conductors (OMIECs). In contrast to conventional organic semiconductors, where charge carriers are exclusively electrons or holes, OMIECs can also support the migration of ions. This coupling of electronic and ionic transport facilitates the interface between OMIECs and electrolyte environments, thereby bridging the gap in ionic-electronic signaling. Thus, this feature introduces exciting possibilities for applications, including actuators,[1] electrochromic displays (ECDs),[2] chemical sensors,[3] sensing and stimulating bioelectronic probes,[4] ion pumps,[5] and logic circuit elements[6] and neuromorphic computing applications[7].

The mixed ionic-electronic transport in organic electronics plays a crucial role in shaping the operational characteristics of devices, including biosensor and neuromorphic computing architectures. In biosensors, the presence of specific ionic transport enables efficient modulation of electronic conductivity by tuning the ion concentration at the polymer/electrolyte interface. Furthermore, in neuromorphic computing architectures, the dynamic interplay between ionic and

electronic transport provides a pathway for emulating complex biological neural networks, enabling low-power and brain-inspired computation. To fully harness the potential of these emerging technologies, a deep understanding of the underlying mixed ionic-electronic transport processes is essential.

In light of these considerations, the investigation of *operando* mixed ionic-electronic transport in conjugated polymers becomes indispensable. By studying these materials under working conditions, *operando* characterization techniques can provide valuable insights into the structural, morphological, and kinetic changes occurring during device operation. This approach is critical for deciphering the fundamental processes governing mixed ionic-electronic transport and unlocking the full potential of organic electronic devices for practical applications.

In this thesis, we present our comprehensive exploration of *operando* measurements to comprehend the structural and morphological changes at the molecular level, along with the operational mechanisms affecting device kinetics in organic electrochemical transistor devices. Through our research, we aim to shed light on the power of *operando* characterization in unveiling the complex interplay between ionic and electronic transport and how this understanding can drive application-oriented molecular design and device engineering.

1.2 ORGANIC MIXED IONIC-ELECTRONIC CONDUCTORS (OMIECS)

Like conventional organic semiconductors, OMIECs generally consist of a π-conjugated backbone for electronic transport. The properties of electronic transport are strongly influenced by the polymer structure, which can be tailored through chemical design and morphology engineering. In order to facilitate ionic conduction, OMIECs usually require the presence of specific functional groups, composite or dopants that allow for ion incorporation and diffusion. So the OMIECs systems can be categorized into (at least) six types:[8] Type I, heterogeneous complexes of a π-

conjugated polymer and a polyelectrolyte; Type II, heterogeneous complexes of a π-conjugated polymer and solid polymer electrolyte; Type III, heterogeneous block co-polymers, which contain an electronic conducting segment and a polyelectrolyte segment; Type IV, heterogeneous block co-polymers, which contain an electronic and ionic conducting segments; Type V, homogeneous single-component conjugated polymer with charged sidechains; Type VI, homogeneous single-component conjugated polymer without charged sidechains. In this thesis, we focus on homogeneous, single-component systems operating in aqueous electrolyte.

1.2.1 *Molecular design for OMIECs*

The single-component OMIECs require careful consideration of molecular design, primarily achieved through backbone and sidechain engineering. OMIECs offer a diverse range of electronic and ionic transport properties, making them versatile for various organic electronic applications. (**Figure 1.1**) Besides, solvent and additive engineering are also common strategies to improve OMIEC properties, which is beyond the discussion in this thesis. In this section, we explore the main strategies and design rules for achieving tailored performance in OMIECs.

Main Strategy: Backbone and Sidechain Engineering

Backbone engineering in conjugated polymer has been well studied for the past four decades. According to the Heeger's clasisification,[9] OMIECs, based on their backbones, can be categorized into second-generation, which is mainly the polythiophene derivatives, and third-generation, including donor-acceptor (D-A) polymers, acceptor-acceptor polymers and some ladder polymers. Over the recent years, the appealing chemical structures, easily adjustable energy levels, and high-charge carrier mobilities of D-A conjugated polymers have rendered them highly desirable in the field of organic electronics.

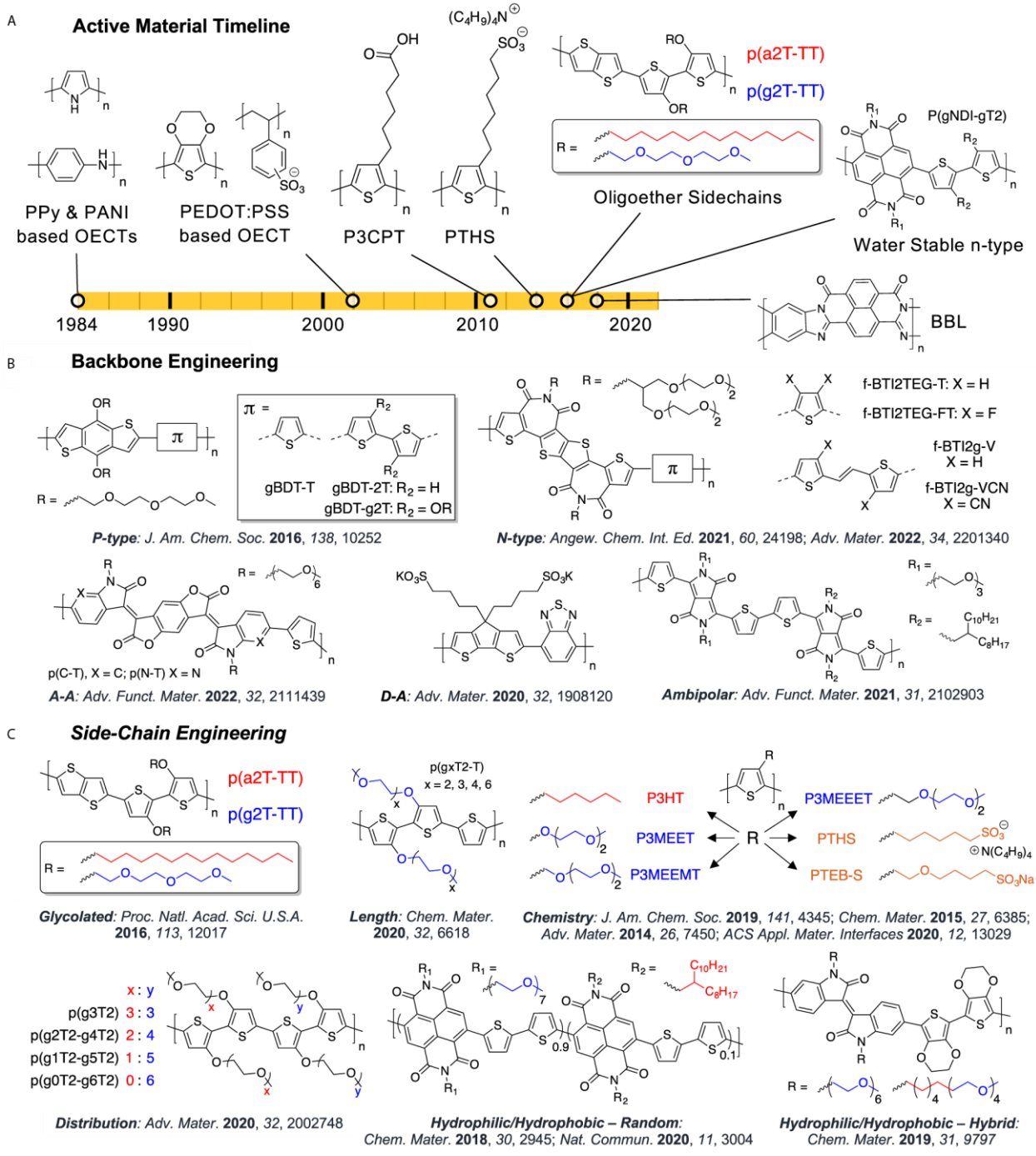

Figure 1.1 Molecular design of OMIECs. (A) Historical development of OMIEC active materials, highlighting seminal studies introducing important design principles. (B and C) Representative chemical structures demonstrating recent examples of (B) backbone engineering and (C) side-chain engineering to enhance active material performance. Reproduced from Ref.[10] with permission from Elsevier.

In 2016, Giovannitti et al.[11] introduced a new design principle that significantly influenced subsequent research in the field. This principle involved the incorporation of glycolated side chains. Many studies have been done with glycolated side-chain functionalization and prove that the sidechains play a crucial role in OMIECs by serving as: i) solvating media for the electrolyte,[12] ii) key components in the crystallization process,[13, 14] and iii) agents for tuning the energy level.[15] However, glycolated side-chain functionalization is not the only direction to improve the ionic transport in the OMIECs. We will discuss this in detail later in Chapter 2.

Design Considerations for Ionic and Electronic Properties

For tailored mixed ionic-electronic transport, specific design rules are considered:

1. Energy level

Similar to other organic semiconductors, the energy level, including the highest occupied molecular orbital (HOMO) and the lowest unoccupied molecular orbital (LUMO), play a critical role in charge transport. For p-type (hole transport) OMIECs, it requires a shallower HOMO for efficient charge injection and facile electrochemical oxidation. While for n-type (electron transport) OMIECs, a deeper LUMO is preferred to achieve a lower operational voltage. Since the most applications of OMIECs operate in ambient conditions, ensuring the stability of the materials via avoiding the side redox reactions of water and oxygen is an important consideration. And this is the main challenge for n-type OMIECs design. The rule of thumb for stable n-type device is a LUMO level more negative than 4.0 eV.[16] With the third-generation OMIECs, one can tailor the energy level of the materials simply via alternating the donor and acceptor units.[17, 18]

2. Planarity

The effective π-conjugation length is essential for realizing disorder-free transport and high charge carrier mobility.[19] Improving the planarization of the backbone can extend the conjugation length

and enhance intrachain charge delocalization. For example, benzodithiophene is a good planar building block for conventional polymers. And recently, the conjugated ladder polymers, due to its restricted torsional angel along the backbone, has been attractive for use as OMIECs.[20]

3. Paracrystallinity

As a semicrystalline, OMIECs overall charge transport depends on the crystalline structural features, including the size, fraction, and orientation of ordered regions, as well as the interconnectivity between them. The principle in OFET mobility is to improve the degree of crystallinity. Interestingly, when OMIECs operating in aqueous environments, higher crystallinity leads to a decreased electronic mobility, since the hydration disrupts the intercrystalline transport.[14] Thus, the optimized paracrystallinity of OMIECs is required to achieve the good device performance.

4. Hydrophilicity

Modulating the hydrophobicity of OMIECs influences the interaction between polymer and electrolyte. Previous study in our group found that the degree of hydrophilicity is correlated with ionic transport when using kosmotropic ions.[13] However, increasing the hydrophilicity is not always beneficial for OMIECs. The excess water uptake might negatively impact the cycling stability due to the overswelling and delamination. Therefore, a balanced combination of hydrophobic and hydrophilic sidechains is required when designing the OMIEC molecules.[21]

1.2.2 *Electrochemical processes in OMIECs*

In OMIECs, the most important phenomena are the charging and discharging processes. However, the terminology might be confusing. Some call the processes as redox (reduction/oxidation) reactions (**Figure 1.2 a**) based on the electron transport from the view of electrochemistry, while some borrow the term from inorganic semiconductor field and name it as doping/dedoping

processes according to the change of conductivity. The unique property of OMIECs charging process is that the processes occur in bulk film, and result to a (psudeo)capacitive box-like I-V curve with redox peaks when measuring cyclic voltammogram. Thus, this charging is also referred to volumetric capacitive doping. (**Figure 1.2 b**) It involves (i) dopant ion injection and transport, (ii) electronic carrier injection and transport, (iii) electronic/ionic coupling.

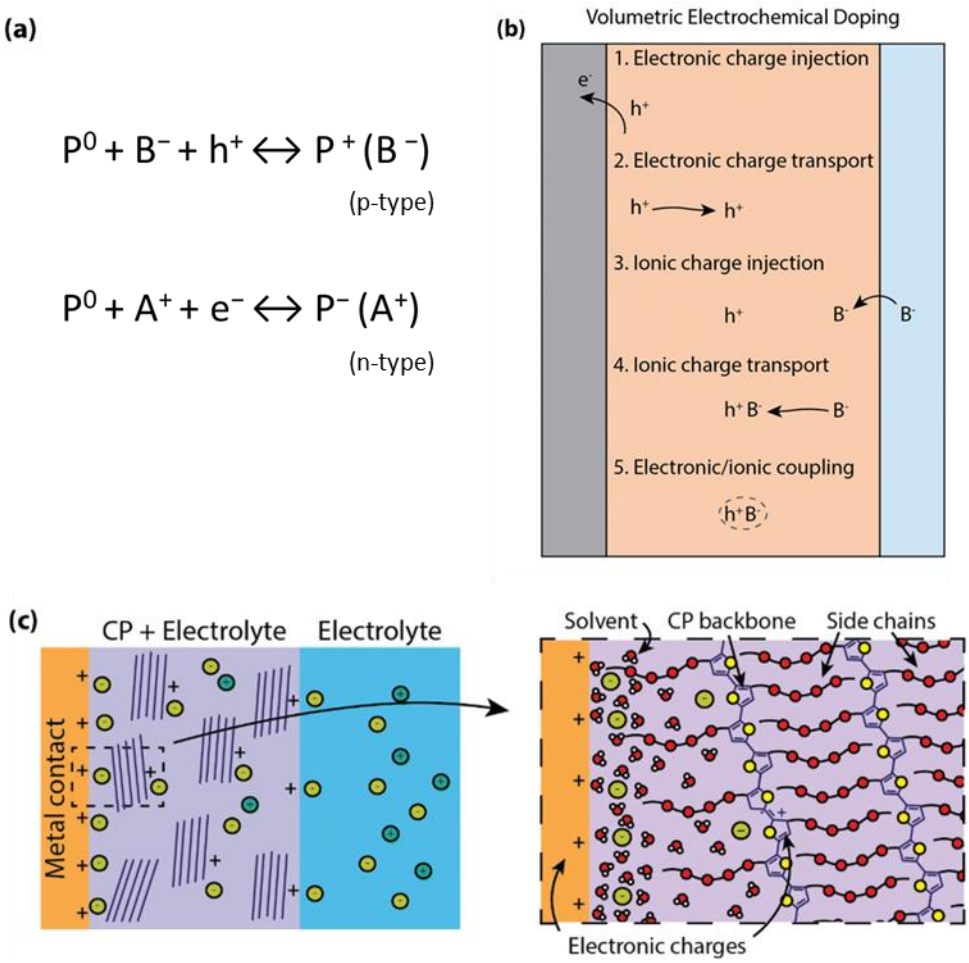

Figure 1.2 Charging in OMIECs. (a) Faradaic charging description. (b) Schematic of volumetric doping processes. (c) Schematic structure near the OMIEC interface showing the ions, solvent, and polymer. Adapted from Ref.[22] with permission from the PCCP Owner Societies.

When OMIECs operate in aqueous medium, the injected ions covered by a hydration shell in the electrolyte get involved in the above process which leads to a swelling of the OMIEC film. It

has been directly observed by various characterization methods, such as thickness increase in atomic force microscopy (AFM),[23] and mass uptake in quartz crystal microbalance (QCM),[24] etc. This charging process can also induce significant structural changes in nanoscale. In our previous study, we have seen several different patterns upon electrochemical doping. i) gradual lamellar expansion, such as poly(3-hexylthiophene-2,5-diyl) (P3HT);[25] ii) minimal lamellar change during the doping, but extreme swelling when hydrated such as poly(3-{[2-(2-methoxyethoxy)ethoxy]methyl}thiophene-2,5-diyl) (P3MEEMT);[25] iii) reversible discontinuous lamellar expansion at critical potential, such as poly[2,5-bis(thiophenyl)-1,4-bis(2-(2-(2-methoxyethoxy)ethoxy)ethoxy)benzene] (PB2T-TEG); [25] iv) irreversible lamellar expansion during the first doping, followed by minimal lamellar change in the subsequent cycles.[26] (see Chapter 2)

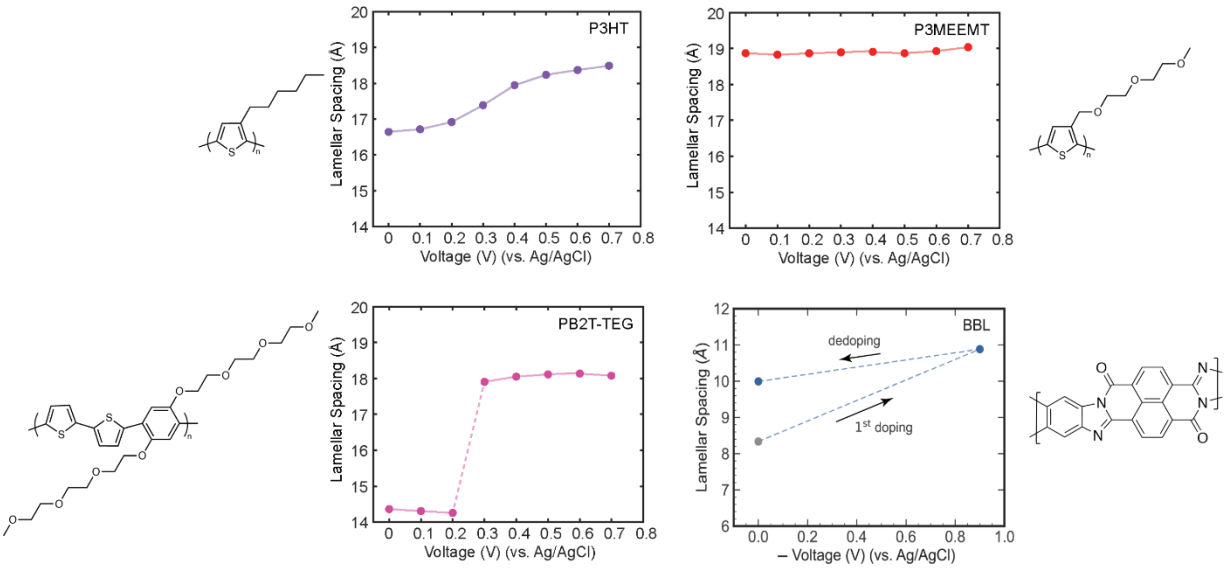

Figure 1.3 Different structural changes upon electrochemical charging in OMIECs. Adapted with permission from [25] Copyright 2020 American Chemical Society.

1.3 ORGANIC ELECTROCHEMICAL TRANSISTORS (OECTS)

As its name suggests, the ionic and electronic transports in OMIECs are normally coupled. To understand each process during electrochemical doping, we need a testbed to decouple the two transport pathways, that is, organic electrochemical transistors (OECTs). OECT is a three-terminal transistor device, utilizing OMIECs as active materials. (**Figure 1.4 a**) Typical characterization of an OECT is known as a transfer curve, shown in (**Figure 1.4 b**) When a doping gate voltage (V_G) is applied to the gate electrode, the OMIEC undergoes the electrochemical reaction we discussed before. The doping-induced changes in electronic conductivity decrease the channel's resistance between the source and the drain (ON state, doped). When a dedoping gate voltage is applied, the changes in the channel are removed and the channel resistance goes back to the initial state (OFF state, neutral). As a result, the gate voltage controls the current flow through the OECT, acting as a transistor. One essential figure of merit for evaluating the performance of OECTs is the transconductance:

$$g_m = \frac{\partial I_D}{\partial V_G} = \frac{Wd}{L}\mu C^*|V_G - V_T| \qquad \textbf{(1-1)}$$

where W is the width of the channel, d is the thickness of the active layer, L is the length of the channel, μ is the electronic carrier mobility, C^* is the volumetric capacitance, and V_{th} is the threshold voltage.[27] Besides the amplitude modulation, the switching speed of turning an OECT on/off can also be a critical property, especially for real-time sensing or time-dependent neuromorphic computing. Additionally, some applications like energy storage or long-term memory neuromorphic element require OMIECs to be stable over thousands of cycles.

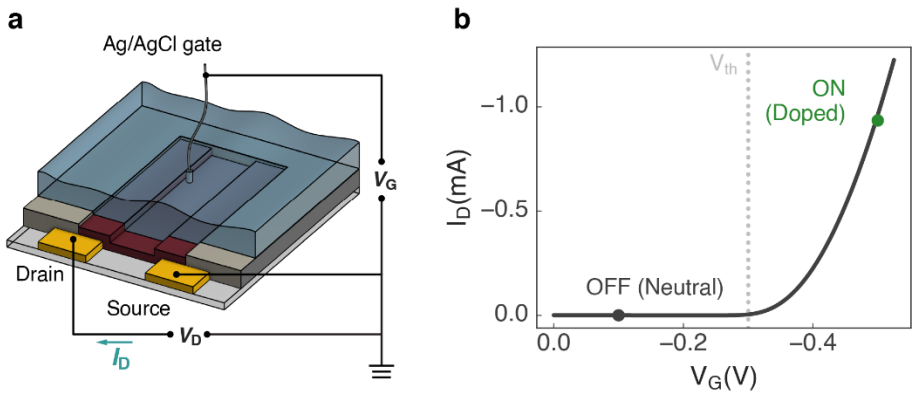

Figure 1.4 Schematic of an organic electrochemical transistor (OECT). a) Schematic of the device structure showing the three-terminal structure. The OMIEC material serves as an active channel across the source and drain electrodes. b) Typical transfer curve of an p-type (hole-transport) OECT, where the drain current is modulated by the Ag/AgCl gate potential.

In order to improve the OECT performance for each specific application requirement, we not only need to understand the mixed transport in thin films, but also need to take the device geometry and operation conditions into account. In contrast to the 2-electrode geometry widely used in electrochemical and spectrometry measurements, the 3-electrode geometry in OECTs introduces a potential gradient across the channel, leading to nonuniform ion/electron distribution which has been predicted by numerical models.[28] As we discussed in the previous section, the hydrated ion uptake leads to extensive compositional and structural changes. This non-uniform ion/electron distribution will contribute to the complexity to understand the structure-property relationship in OMIEC devices.

1.4 OPERANDO CHARACTERIZATION TECHNIQUES

Operando characterization techniques are powerful tools used to study materials and devices under realistic operating conditions. These techniques allow researchers to gain insights into the dynamic changes occurring during the functioning of a system, maintaining the chemical environment and electric field, which are essential for understanding the true behavior of the materials. *Operando*

("during operation") is district from *ex-situ* ("off-site') or *in-situ* ("on the site"). In OMIEC field, *ex-situ* characterizations are normally performed on pristine or pre-doped dry films in ambient environment or even under vacuum. Some techniques are not compatible with aqueous electrolyte environment, such as X-ray photoelectron spectroscopy (XPS). While *in-situ* characterizations typically maintain the OMIEC materials in the electrolyte but might remove the external electric potential. For example, Surgailis *et al.* conducted *in-situ* AFM scans in electrolyte immediately after electrochemical doping/dedoping with no external potential applied.[23]

However, to understand the mixed ionic-electronic transport during the charging/discharging, both the chemical and the electric environments matter. Without either of them, the results might be inaccurate and some key information will be overlooked. For example, as we discussed in the previous section, the swelling degree of OMIECs in the electrolyte impacts both ionic and electronic transports, as well as the switching speed and stability in the OECTs. However, Szuumska *et al.* have demonstrated with a series of NDI-T2-based OMIECs swollen in the electrolyte that drying in the air results in the swollen film thickness shrinkage back to the pristine thickness.[29] This means the ex-situ measurements performed outside the electrolyte probably overlook the most important information of OMIECs swelling. Similarly, the external electrical field is also necessary to unveil the mixed ionic-electronic transport coupling. For instance, due to their energy level, OMIECs generally undergo a dramatic color change after electrochemical reactions, which provides us a direct way to track the charge level by spectrometry. When studying the stability of an electrochromic device, Skene *et al.* indicated that, after the OMIEC disconnected the external potential circuit, the transmission decayed back to 80% in 30 min.[30] This observation suggests that the charged OMIEC is hard to maintain the doping level without the external potential, which is also known as self-discharge in the battery field. Furthermore, within the identical

environment to the real device operation, *operando* measurements enable the time-resolved studies, which are essential to capture the dynamics and kinetics. In Chapter 3, we will present a showcase how operando characterization helps us understand device kinetics and even provide engineering strategy to improve the transient performance.

So far, we have emphasized the importance of operando characterizations in OMIEC studies. However, no single characterization will provide a full picture of the mixed ionic-electronic transport. Therefore, with the goal of establishing structure-property relationship, researchers need a combination of methods across different level scales. (**Figure 1.5**) According to the OMIECs operation properties, characterization focus on ionic transport, electronic transport and ionic-electronic coupling determination at both nonequilibrium and steady-state.

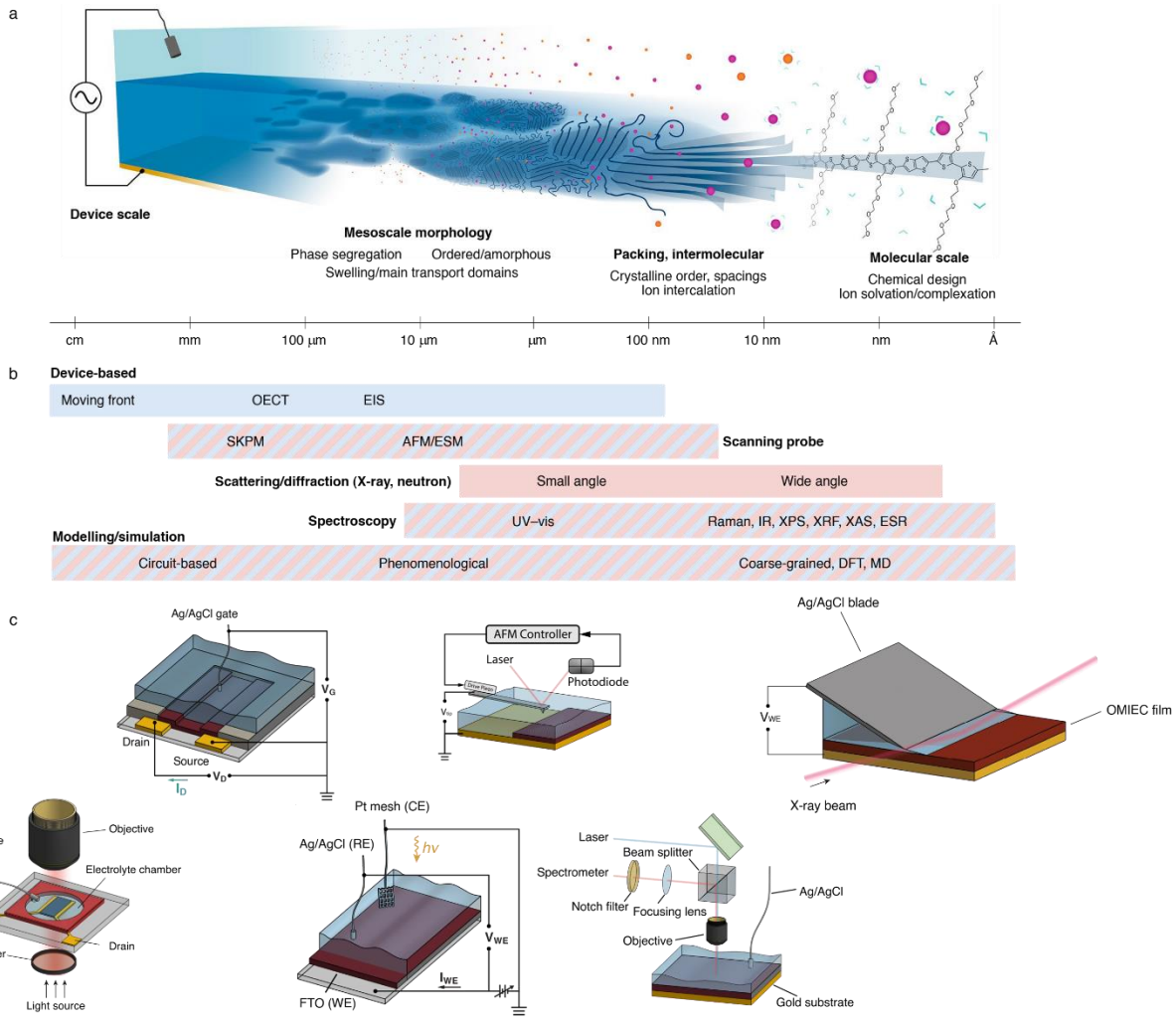

Figure 1.5 Multi-scale microstructure and associated techniques for studying OMIECs. Device to molecular scale microstructure and interactions with an electrolyte. Magenta denotes anion, orange denotes cation. (b) Classes of characterization, and examples of specific techniques for probing transport and structure across these size scales. Blue denotes techniques that provide information about electronic/ionic transport. Pink denotes structural characterization. Reproduced with permission from Ref [8] Copyright 2020 Springer Nature. (c) Schematic examples of operando characterization techniques covered in this dissertation.

1. Electrical and electrochemical characterization

Assessment of mixed ionic and electronic transport in OMEICs primarily involves electrical characterization, with a particular focus on current-voltage measurements and electrochemical

techniques. As mentions in 1.3, OECT is a good testbed to understand the mixed transport across a range of conditions, such as ion species,[31, 32] ion concentrations,[33] and voltage potentials.[34] Leveraging the capabilities of simulation models, valuable information can be extracted from OECT devices concerning ion diffusion type[25] and coefficient[35], electronic mobility[34], energy density of states, and the degree of material disorder.[36] These simulation models allow researchers to gain deeper insights into the complex transport processes occurring within OMIECs, providing a comprehensive understanding of their behavior and performance in various device configurations.

Traditional electrochemical characterization methods are also helpful to characterize the OMIEC mixed transport. Cyclic voltammetry (CV) is the most common technique employing linear potential sweeps. In the context of OMIECs, CV provides valuable insights into their redox behaviors reflecting the "pseudocapacitive" (dis)charging process. By analyzing their peaks, researchers can gain information about the ion migrations in organic semiconductors.[37]Anothoer common technique is electrochemical impedance spectroscopy (EIS), which extracts the impedance under various frequencies of applied potential. With the frequency sweep, one can split the capacitor-like behavior in OMIECs from the resistor-like portion in the circuit. Considering the volumetric doping properties, the volumetric capacitance C^*, which indicates the charge storage capability of OMIECs, is typically calculated from EIS data. In addition, coulometry is an alternative to characterize the charging process by measuring the current over time after applying a potential step.

2. Spectroelectrochemistry

Spectroelectrochemistry is a powerful and versatile technique that combines the advantages of both spectroscopy and electrochemistry, providing real-time and *operando* insights into the

dynamic behavior of materials during electrochemical processes. This cutting-edge approach enables researchers to investigate the simultaneous changes in electronic and ionic properties, shedding light on the intricate interplay between charge transport and redox processes within OMIECs under realistic operating conditions.

Among the diverse spectroscopic methods available, UV-Vis spectroscopy is commonly used in operando studies of OMIECs. This technique provides information on the transition of electrons in the frontier orbitals of molecules, as well as the conformational and structural information.[38] One important ability of UV-Vis spectroscopy is that it can capture both the equilibrium states[39] (steady-state) and the intermediate states[40] (kinetics) during the electrochemical process.

Another valuable tool in spectroelectrochemistry operando studies is Raman spectroscopy. Raman spectroscopy enables the investigation of molecular vibrations, offering insights into schemical reactions and structure changes occurring within OMIECs during electrochemical cycling.[41] The Raman insensitivity to water in the spectral range between 1000 and 2000 cm^{-1}, where normally the C═C and C═O stretching peaks are located, renders it valuable for investigating OMIEC materials operating in aqueous electrolytes. However, due to the weak Raman signal, the long integral time makes it difficult to track the microsecond to millisecond scale transient behaviors in OMIECs.

3. X-ray Scattering

X-ray scattering has been applied in operando characterization in OMIECs to reveal the structural information according to different length scales by changing the collection angle of the X-ray scattering. It is divided into two categories: small-angle X-ray scattering (SAXS) and wide-angle X-ray scattering (WAXS). Since OMIECs are typically fabricated as a thin film, X-ray scattering is often performed in a grazing incidence.

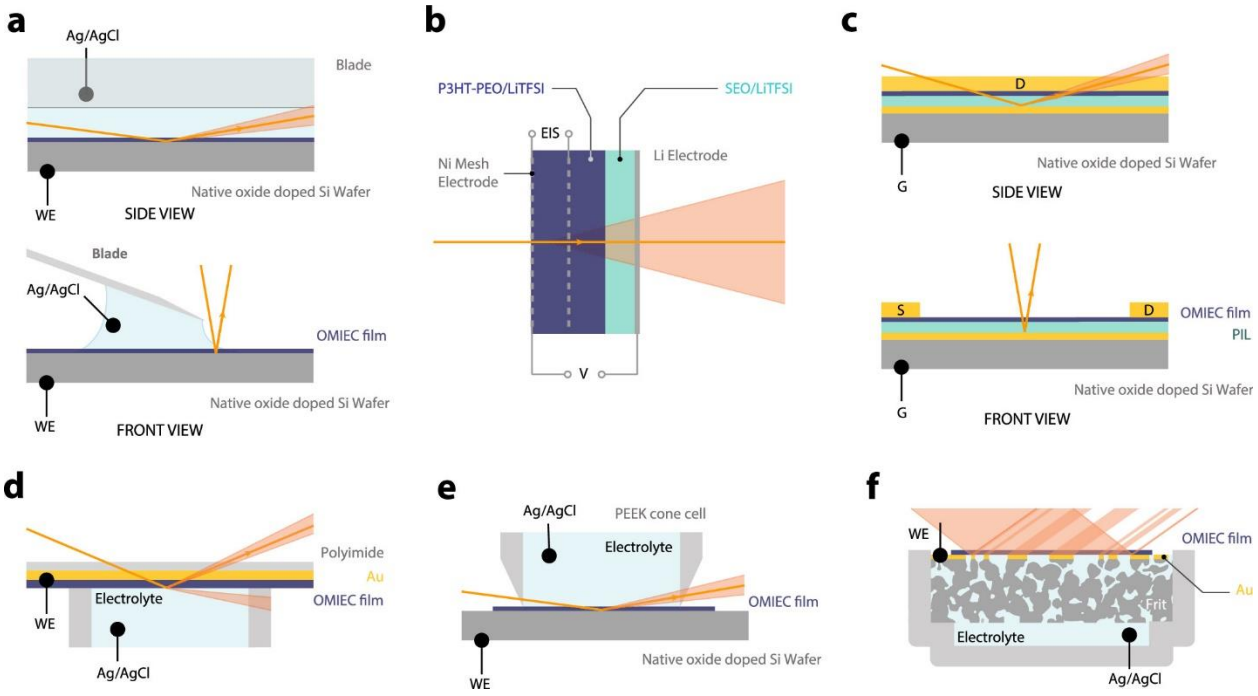

Figure 1.6 Schematic operando GIWAXS test cells. (a) Blade coating setup. (b) In situ electrochemical cell for WAXS measurement reported by Thelen et al.[42] (c) The polyionic liquid (PIL) device setup reported by Thomas et al.[43] (d) The polyamide cell reported by Bischak et al.[25] (e) The cone cell reported by Paulsen et al.[44] (f) The frit cell reported by Paulsen et al. Reproduced with permission from Ref[45]. Copyright 2022 American Chemical Society.

Scattering techniques have provided valuable insights into various structural properties of materials, such as intermolecular spacings, crystallite size, paracrystallinity, phase separation, domain size, shape, and spacing.[46]In the crystalline domain of most OMIECs, polymer chains stack in three dimensions and form lamellar stacks (h00), π stacks (0k0), and backbone repeating structures (00l) that can be identified by their GIWAXS pattern. These structural spacing will change during the electrochemical process, inferring the interaction between the electrolyte and OMIECs, as well as mixed ionic-electronic transport. Besides, the coherence length and degree of crystallinity (DOS) related to the highly-ordered crystalline/disordered amorphous domain relationship, which is a great interest in OMIECs material design.[14, 40]The main challenge in

operando X-ray scattering is the design of the setup cell. Many efforts have been done and shown in **Figure 1.6**.

4. Scanning Probe Microscopy

Scanning microprobe techniques offer the unique capability of providing spatially resolved information on various aspects of OMIEC materials. These techniques, including atomic force microscopy (AFM) and its derivatives, have successfully studied microstructure,[25] film swelling,[47] and ion distribution[40] and local conductivity[48] of OMIEC operation. *Operando* scanning probe microscopy requires the electrical potential, which can be applied from external potentiastat, or internal biased AFM tip. Among the prominent operando scanning probe techniques are atomic force microscopy (AFM) and electrochemical stain microscopy (ESM). Except AFM and ESvarious advanced AFM techniques can offer valuable insights into OMIEC materials as ex-situ methods. Techniques such as Kelvin probe force microscopy (KPFM) can probe the local surface potential and work function; Photo-induced force microscopy (PiFM) combines the capabilities of AFM with infrared spectroscopy, allowing for the characterization of local chemical composition and molecular orientation; Conductive AFM (cAFM) enables the imaging and quantification of local electronic conductivity variations in OMIEC films. However, the compatibility of these AFM techniques with the electrolyte can present a significant challenge when conducting operando studies.

In addition to the previously mentioned operando techniques, several other methods can be highly beneficial in the researchers' toolbox for studying OMIECs and other materials: *e.g.*, Quartz crystal microbalance (QCM), nuclear magnetic resonance (NMR).Combined different operando techniques at different scales enable a comprehensive exploration of OMIEC materials at various length and time scales. Although challenges related to electrolyte compatibility exist, the

integration of multiple operando and ex-situ techniques offers a holistic approach to advance the design and optimization of OMIECs for diverse organic electronic applications. With their combined capabilities, operando techniques continue to drive breakthroughs in materials science and foster innovations in organic electronics.

1.5 SUMMARY

This dissertation describes three studies which seek to show the power of operando characterization involved in OMIECs from the molecular to the device scale. In these cases, we focus on different aspects of OMIEC behavior and properties during electrochemical doping.

In Chapter 2, we delve into understanding the structural crystalline changes occurring during the electrochemical doping process. Specifically, we focus on elucidating the unknown mechanisms governing a n-type ladder conjugated polymer. Through operando GIWAXS characterization, we investigate the unique hydration mechanism during the first doping cycle and seek to gain insights into next generation OMIECs.

Chapter 3 takes a closer look at the switching behavior of OECTs, which is important in real-time sensing and signal recording, as well as neuromorphic computing. With direct probing of OECT switching dynamics, we uncover the limitations of the switching speed and identify factors that contribute to these constraints. Subsequently, we propose engineering strategies to enhance the switching speed of OECTs, aiming to optimize their performance for specific application requirements.

Finally, in Chapter 4, we stusy the root sources of OECT instability during cycling operations. Employing operando techniques, we investigate the underlying factors that lead to performance degradation and instability in OECTs over repeated cycling. By gaining a comprehensive

understanding of these factors, we aim to propose mitigation strategies to enhance the long-term stability and reliability of OECT devices.

Overall, this dissertation showcases the remarkable capabilities of operando characterization techniques in unraveling the intricate electrochemical processes of OMIECs. By examining these processes at different levels, from the molecular to the device scale, we contribute valuable knowledge to the field of organic electronics. The insights gained from our three studies not only advance the fundamental understanding of OMIEC behavior but also pave the way for improved device design and performance optimization for diverse organic electronic applications.

Chapter 2. HYDRATION OF A SIDE-CHAIN-FREE N-TYPE SEMICONDUCTING LADDER POLYMER DRIVEN BY ELECTROCHEMICAL DOPING

Adapted with permission from Jiajie Guo, Lucas Q. Flagg, Duyen K. Tran, Shinya E. Chen, Ruipeng Li, Nagesh B. Kolhe, Rajiv Giridharagopal, Samson A. Jenekhe, Lee J. Richter, and David S. Ginger. "Hydration of a Side-Chain-Free n-Type Semiconducting Ladder Polymer Driven by Electrochemical Doping" Journal of the American Chemical Society 2023 145 (3), 1866-1876 DOI: 10.1021/jacs.2c11468 Copyright 2023 American Chemical Society.

2.1 OVERVIEW

We study the organic electrochemical transistor (OECT) performance of the ladder polymer, poly (benzimidazobenzophenanthrolinebenzimidazobenzophenanthroline) (BBL) in an attempt to better understand how an apparently hydrophobic side-chain-free polymer is able to operate as an OECT with favorable redox kinetics in an aqueous environment. We examine two BBLs of different molecular masses from different sources. Regardless of molecular mass, both BBLs show significant film swelling during the initial reduction step. By combining electrochemical quartz crystal microbalance gravimetry, *operando* atomic force microscopy, and both *ex-situ* and *operando* grazing incidence wide-angle X-ray scattering (GIWAXS), we provide a detailed structural picture of the electrochemical charge injection process in BBL in the absence of any hydrophilic side-chains. Compared with *ex-situ* measurements, *operando* GIWAXS shows both more swelling upon electrochemical doping than has previously been recognized and less contraction upon dedoping. The data show that BBL films undergo an irreversible hydration driven by the initial electrochemical doping cycle with significant water retention and lamellar expansion that persists across subsequent oxidation/reduction cycles. This swelling creates a hydrophilic environment that facilitates the subsequent fast hydrated ion transport in the absence of the

hydrophilic side-chains used in many other polymer systems. Due to its rigid ladder backbone and absence of hydrophilic side-chains, the primary BBL water uptake does not significantly degrade the crystalline order, and the original dehydrated, unswelled state can be recovered after drying. The combination of doping induced hydrophilicity and robust crystalline order leads to efficient ionic transport and good stability.

2.2 INTRODUCTION

Conjugated polymers showing mixed ionic-electronic transport,[29, 47, 49, 50] more generally organic mixed-ionic electronic conductors (OMIECs), have emerged in the past few decades as promising materials for applications in bioelectronics,[51-54] energy storage,[55, 56] logic circuit elements,[20, 57] and neuromorphic computing.[58-60] Organic electrochemical transistors (OECTs) are widely used as a model testbed to study mixed ionic-electronic transport in OMIECs.[31, 61, 62] Unlike conventional organic field-effect transistors (OFETs), an OECT's source-drain current (I_D) is modulated by the gate (V_G) through voltage-driven redox processes and associated ion uptake from the electrolyte into the entire volume of the semiconductor channel, resulting in bulk doping/dedoping. Hence, the efficiency of this modulation, described by the transconductance ($g_m \equiv \partial I_D / \partial V_G$), is governed by the carrier transport mobility (μ) and the volumetric capacitance (C^*) in the channel.[27] Tremendous progress has been achieved in developing high-performance p-type (hole transport) materials, with μC^* value on the order of hundreds of F cm^{-1} V^{-1} s^{-1}.[21, 63] However, n-type organic materials have generally lagged behind.[16, 64-67] The lack of n-type materials limits applications such as biosensors involving cations, complementary circuit logic, and electrochemical energy storage.

In recent years, considerable effort has been devoted to the design and synthesis of novel n-type OMIECs, mainly based on donor-acceptor (D–A) copolymers.[16] The most popular molecular design strategy is to use hydrophilic side-chains to help ionic transport in aqueous electrolyte, for

both p-type[68-71] and n-type[29, 64, 71, 72] materials. However, studies suggest that excessive water uptake harms the electronic mobility and stability when adding hydrophilic glycol side-chains.[14, 29, 33] In this context, the polymer poly(benzimidazobenzophenanthroline) (BBL, structure shown in **Figure 2.1 A**), stands out as a notable exception that functions without glycol side-chains.[20, 23, 73] Indeed, its electron mobility in OECTs has been reported as an order of magnitude higher than D–A-based n-type polymers, presumably due to the planar, rigid BBL backbone.[6] Recently, Fabiano *et al.* demonstrated that increasing the molecular mass yields an improvement of electronic mobility.[73] Furthermore, Inal *et al.* reported that the side-chain-free BBL accommodates a higher density of cations and water, compared to the more conventional naphthalenediimide(NDI)-based glycolated polymer, P-90.[23] As a result, BBL shows a record high volumetric capacitance in n-type OMIECs and somehow overcomes the ubiquitous μ-C^* trade-off, that commonly plagues p-type materials. Nevertheless, a detailed understanding of how water and cations are able to enter such a hydrophobic film is still lacking.

Here, we explore the electrochemical doping process using a wide range of complementary analytical methods on both commercial low molecular mass BBL (**BBL$_\mathbf{L}$**) and in-house synthesized high molecular mass BBL (**BBL$_\mathbf{H}$**). In both versions of BBLs, we observe an irreversible water mass uptake during the first electrochemical doping step via electrochemical quartz crystal microbalance (eQCM), which agrees with the *operando* atomic force microscopy (AFM) film thickness change. Furthermore, we probe the nanoscale structure change by electrochemical strain microscopy (ESM) *operando*. Finally, we characterize the BBL crystalline structure changes using both *ex-situ* and *operando* grazing incidence wide-angle scattering (GIWAXS). In contrast to previously reported *ex-situ* GIWAXS which showed minimal structure changes,[23] we observe significant lamellar expansion using *operando* GIWAXS. By combining

these complementary results, we propose a unique film hydration behavior in the side-chain-free ladder polymer BBL during the electrochemical reduction. In the absence of the electrochemical bias, the hydrophobic BBL film shows resistance to water uptake in both crystalline and amorphous regions. However, during the initial electrochemical doping, BBL undergoes an ≈31% lamellar expansion upon water injection, which remains persistent across the subsequent doping/dedoping cycles. We propose this retention of water between the lamellar structure creates a hydrophilic microenvironment for fast ion movement at the molecular level, changing our understanding of how BBL incorporates water from being one of microvoids to being one that also includes significant changes to the molecular packing to the incorporation of waters into the crystalline regions of the film. Importantly, this expansion is not observed in *ex-situ* samples, which suggests the water uptake is reversible upon film drying. These results provide guidance for designing new OMIEC polymers that can overcome the trade-off between ionic and electronic transport and achieve a high μC^*.

2.3 RESULTS AND DISCUSSION

Figure 2.1 A shows the chemical structure of the BBL polymer we studied. In this report, we studied two different BBLs, one synthesized in house by the Jenekhe group (**BBL$_H$**, M_v = 60.5 kDa),[50] and one purchased commercially from Sigma-Aldrich (**BBL$_L$**, M_v = 6.15 kDa). The molecular mass difference was also observed by dynamic light scattering (DLS) as shown in **Figure A.2**.

First, we evaluated the OECTs performance of both versions of BBLs. In these OECT measurements, we used a Ag/AgCl pellet as the gate electrode, and 100 mmol/L degassed aqueous potassium chloride (KCl) as the electrolyte. **Figure 2.1 B,C** show a typical transfer curve along with transconductance, g_m, and output curves for both **BBL$_L$** and **BBL$_H$**, respectively. The drain

current and transconductance of the **BBL$_H$** OECTs are consistently 2 orders of magnitude higher than the **BBL$_L$** OECTs, and the peak transconductance, $g_{m,\,\mathrm{peak}}$, appears at a lower gate voltage for the **BBL$_H$**. Also, the threshold voltage is slightly more negative (≈100 mV) for the **BBL$_H$**. (**Figure A.3**) A similar threshold voltage shift was observed in other BBL OECT studies.[73] The shift in both peak transconductance and threshold voltage suggests that the **BBL$_H$** is energetically easier to be electrochemically doped in KCl. This difference also agrees with the observed onset voltage difference in cyclic voltammetry (CV) measurements of the two BBLs (**Figure A.4**).

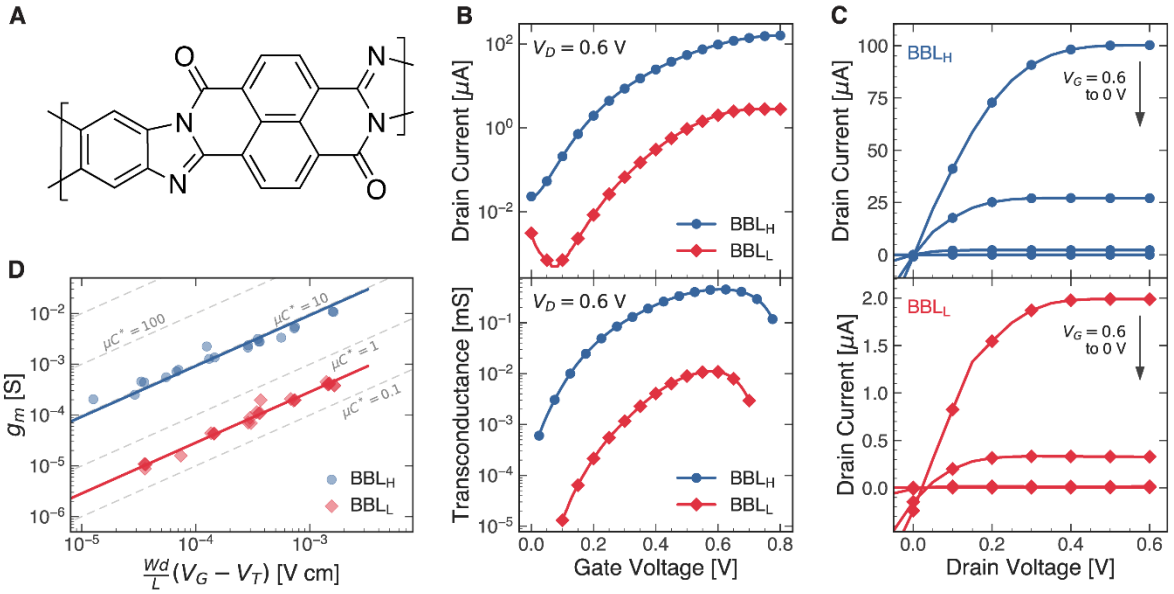

Figure 2.1 OECT performance of two BBLs. (A) The chemical structure of BBL repeat unit. (B) Typical OECT transfer curves with calculated transconductances and (C) output curves for both BBLL and BBLH OECTs in 100 mmol/L KCl. (channel width = 100 μm, channel length = 10 μm, channel thickness ≈120 nm) (D) The peak transconductance $\boldsymbol{g_{m,\,\mathrm{peak}}}$ of BBL OECTs as a function of operating conditions and channel geometry. Each data point represents one OECT measurement. The linear slope of the data determines the OECT figure of merit μC^*. Dashed lines denote constant μC* product.

Compared to OFETs, OECTs have the advantage of volumetric capacitance, wherein the entire bulk of the active OMIEC film, instead of the surface, can accommodate ions and electronic carriers.[74] After rewriting the conventional field-effect transistor equation to replace the gate

capacitance, *C*, with the effective volumetric capacitance, *C**, the transconductance of OECTs in the saturation regime, is given by[27]:

$$g_m = \frac{\partial I_D}{\partial V_G} = \frac{Wd}{L}\mu C^* |V_G - V_T| \quad \textbf{(2-1)}$$

where W, d, and L are the channel width, thickness, and length, respectively, μ is the OECT channel carrier mobility, C^* is the OECT channel volumetric capacitance, V_G is the operating gate voltage, and V_T is the threshold voltage. Following **Equation (2-1)**, we extracted the μC^* products of the two different BBLs from a linear regression between peak transconductance $g_{m,\,\text{peak}}$ and $\left(\frac{Wd}{L}\right)|V_G - V_T|$ obtained from a series of devices with different *Wd/L* ratios. **Figure 2.1 D** shows that our BBL OECT data are well fit to **Equation (2-1)**, with μC^* increasing more than 30 times going from **BBL$_\mathbf{L}$** (0.28 ± 0.01 F cm^{-1} V^{-1} s^{-1}) to **BBL$_\mathbf{H}$** (9.27 ± 0.03 F cm^{-1} V^{-1} s^{-1}).

For an OECT, especially in the applications of sensors and complementary circuits, response time is also a crucial property, which relates to the ion migration from the electrolyte to the active polymer film. With such high volumetric capacitance, the BBL transistors can still be switched ON/OFF in tens of milliseconds, which suggests an unexpectedly fast ion transport in such hydrophobic films (**Figure A.5**). In addition, we also examine the stability of both BBL devices with continuous pulse gate potential over 100 cycles, and both BBLs show a good stability without significant current degradation. (**Figure A.6**) Compared to other n-type polymers with glycol side-chains,[29] the side-chain-free backbone structure avoids possible film degradation even doped to bipolaron region (detailed calculation in **Appendix A** about UV–vis spectra).

To further study the contribution of the carrier mobility (μ) and volumetric capacitance (C^*) separately, we next measured the volumetric capacitance using electrochemical impedance spectroscopy (EIS). We fit the EIS spectra using a modified Randles circuit: R_s(CPE//R_{ct}), where R_s is the electrolyte resistance, CPE is a constant phase element, and R_{ct} is the charge transfer

resistance. (**Figure A.7** and **Figure A.8**) The constant phase element (CPE) can be interpreted as arising from the distribution of counterion−polaron pairs in the bulky polymer films.[75] We observed an improvement in the volumetric capacitance C^* with the **BBL$_H$**, which suggests that the **BBL$_H$** film has a higher density of ion-accessible sites. (**Figure A.8**) Taking the threshold voltage shift into account to get a fair comparison, the **BBL$_H$** and **BBL$_L$** films show average C^* values of 1007.1 ± 172.8 F/cm^3 and 539.8 ± 85.8 F/cm^3 at 0.7 and 0.8 V, respectively. The higher C^* of **BBL$_H$** is also consistent with its higher CV current level, indicating more electronic charge injection (**Figure A.4**). Based on the μC^* from the transistor measurements and the C^* from EIS, we determined the electron mobilities of both BBLs. We calculate that **BBL$_H$** ((9.2 ± 1.6) × 10^{-3} cm^2 V^{-1} s^{-1}) has a mobility that is over an order of magnitude higher than that for **BBL$_L$** ((0.52 ± 0.08) × 10^{-3} cm^2 V^{-1} s^{-1}). Notably, considering the presence of water in the films, which may hinder electronic transport, the polymer OECT mobility is normally lower than its OFET mobility. Therefore, the mobility we measure for BBL is in good agreement with the mobility of 10^{-2} to 10^{-3} cm^2 V^{-1} s^{-1} previously reported for both solid-state OFETs[76, 77] and wet OECTs.[20, 23, 73] The difference in mobility implies that the **BBL$_H$** with a higher molecular mass results in an enhanced electron transport process.[73] In conjugated polymers, the relationship between mobility, molecular mass, and morphology is complicated,[78-80] but the enhanced mobility of BBL follows the trend seen for many other materials.[73, 81, 82] A comparison of the OECT performance of two BBLs is summarized in **Table 2.1** and additional discussion in **Appendix A.1**. We note that, in addition to higher mobility and volumetric capacitance, **BBL$_H$** shows faster switching times both turning ON and turning OFF processes.

Table 2.1 Summary of BBL OECTs Performance.[c]

	ON/OFF ratio [b]	V_T [b] [V]	g_m [b] [mS]	τ_{on} [b] [ms]	τ_{off} [b] [ms]	μC* [c] [F cm^{-1} V^{-1} s^{-1}]	C* [d] [F cm^{-3}]	μ [e] [cm^2 V^{-1} s^{-1}]
BBL_H	1.59×10^4	0.17	10.8	80.3	6.5	9.27 ± 0.03	1007.1 ± 172.8	$9.2 \pm 1.6 \times 10^{-3}$
BBL_L	1.23×10^4	0.28	0.41	142	181	0.28 ± 0.01	539.8 ± 85.8	$0.52 \pm 0.08 \times 10^{-3}$

[a] All error bars represent standard error of the mean. [b] Average data extracted from a channel with a width of 4000 μm and a length of 10 μm. [c] Extracted from **Equation (2-1)** with peak $g_{m,\,peak}$ (shown in **Figure 2.1 D**). [d] Obtained from EIS measurements for various electrode areas. [e] Obtained via dividing μC* by C*.

To further understand the difference in volumetric capacitance values, we used spectroelectrochemistry and coulometry to characterize the polaron/bipolaron formation. The pristine films show similar UV−vis absorption spectra, while the π–π* transition peak (≈560 nm) redshifts as the molecular mass increases (**Figure A.9**). This peak shift suggests that the **BBL_H** has a longer effective conjugation length, which agrees with the electronic mobility enhancement in **BBL_H**.[83-85] **Figure A.10–Figure A.12** show the spectra change for the two polymers upon the electrochemical doping process under different bias. When a positive bias is applied to the gate, the BBL films are electrochemically reduced. The π–π* transition of the ground state intensity first quenched at a low voltage (below 0.5 V) in the range of 450 to 650 nm, accompanied by two isosbestic points at 435 and 670 nm. Simultaneously, a broad absorption peak grows in the range of 700 to 900 nm, indicating a transition from the neutral BBL into a charged BBL.[23, 76] Following previous studies, we assign the peak around 880 nm (labeled as B) as a polaron and the peak around 460 nm (labeled as A) as a bipolaron.[50] At the same potential, the polaron and bipolaron densities formed in the **BBL_L** are always lower than the **BBL_H**, which is consistent with the smaller volumetric capacitance value of **BBL_L** (**Figure A.11**). We also cross-checked these doping densities determined via spectroelectrochemistry by using coulometry. Although the

spectroelectrochemistry measurement was carried out in a degassed electrolyte, the whole setup is exposed to ambient air during measurements. Since the oxygen reduction reaction (ORR) may then contribute to the current,[23, 86] we note that the electron densities in BBLs via coulometry need to be interpreted with caution. To minimize the impact of ORR, we calculated the number of electrons in the reduced BBL by integrating the dedoping current after the UV–Vis spectra measurements were taken and normalized it to the film volume. (See detailed discussion on the impact of ORR on the electrochemical doping in **Appendix A.2**) With this coulometry approach **BBL$_H$** shows an ≈2-fold higher doping level than the **BBL$_L$**, reaching 2 electrons per repeat unit at 0.9 V shown in **Figure A.11**. This result agrees with our volumetric capacitance data from the EIS fitting.

When interacting with aqueous solutions, the swelling of conjugated polymer films is commonly divided into two classifications: (1) *passive swelling*: the hydration of a dry film by the electrolyte without applied potential; (2) *active swelling*: water injection that occurs during active redox processes. Previous work has shown that polymers with a large fraction of glycol side-chains can undergo significant water uptake and retention, even in the absence of applied potential.[14, 21, 29, 61] On the other hand, more hydrophobic polymers with few hydrophilic side-chains, which can behave like OECTs, often only exhibit active swelling.[14, 29, 87] As mentioned, BBL lacks such side-chains, therefore the conventional description of aqueous operation does not apply. We therefore need to understand what physical processes allow BBL to operate as an OECT as well as what doping mechanisms are affected by molecular mass.

In this context, we further investigate the film swelling of the two BBLs during the electrochemical doping process using gravimetric measurements with an eQCM. We first probe the *passive* swelling, which relates to the film hydration after contact with the aqueous solution

without bias. The mass of the BBL film is determined by the Sauerbrey equation in both air and aqueous solution since BBL films are sufficiently thin and exhibit a low degree of swelling (less than 0.1% change of the resonance frequency) such that viscoelastic corrections are not needed.[23, 88-90] It is not surprising that without any hydrophilic side-chains, both BBL films show minimal swelling, whereas other n-type polymers with alkyl-glycol side-chains show massive swelling, up to ≈100 %.[29]

We then characterized *active* swelling. In previous p-type polymer studies, it is known that the ions are injected into (or removed from) the film surrounded by a hydration shell with some number of water molecules and perhaps additional bulk water.[29] With the simultaneous recording of current, we calculate the mass of the injected cations by integrating the charges, assuming these are the only charged species getting into the film. We then calculate the water mass by subtracting the cation mass from the total mass, thus providing an estimate of the number of waters dragged into the film during cation injection. Interestingly, in contrast to other OMIEC polymers with alkyl-glycol side-chains showing continuous retention of mass accumulation during active swelling,[69, 91] the mass change in BBL shows two distinct phases. During the very first cycle from neat wet films, both molecular mass versions BBL films show a dramatic mass retention (82% for **BBL$_H$** and 74% for **BBL$_L$**) that is not reversible upon subsequent cycles (**Figure 2.2 A**). However, the mass of ions remaining in the dedoped films after the first cycle is only about 3.4% for **BBL$_H$** and 2.8% for **BBL$_L$**, respectively. Thus, we propose that the electrochemically irreversible mass gain is mainly caused by water molecules, not the cations. Notably however, this electrochemically-irreversible first step water uptake could be regenerated on the same crystal after drying under a vacuum, suggesting that it does not permanently change the film morphology.

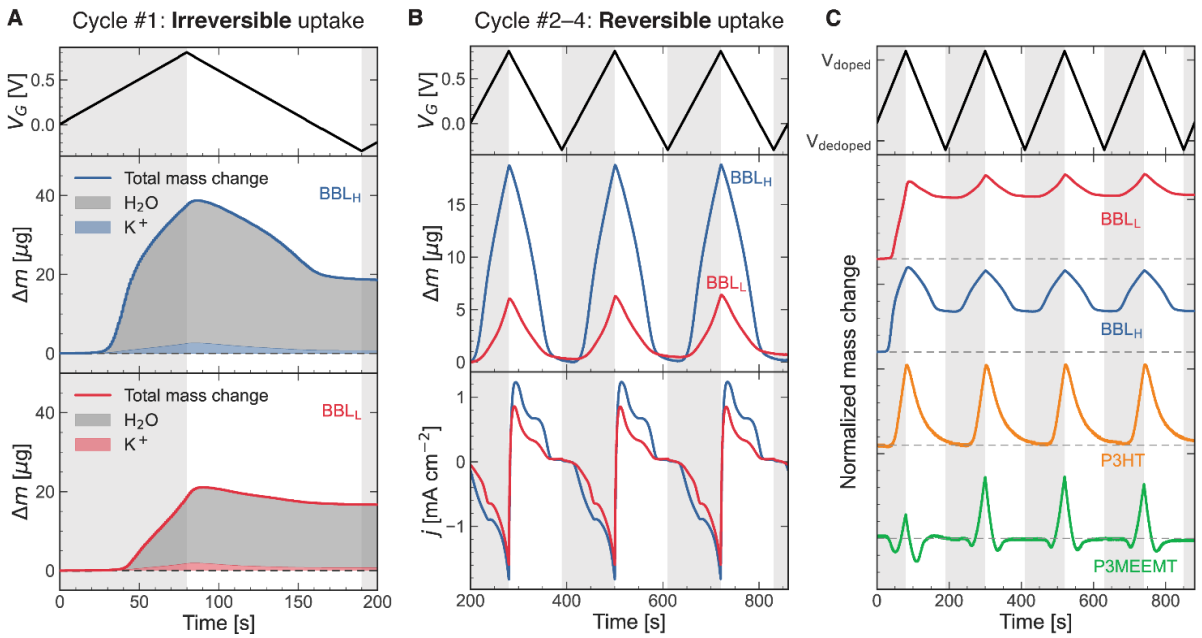

Figure 2.2 Mass uptake upon electrochemical process. (A) The *irreversible* total mass uptake measured by QCM during the *first* cycle of CV sweep (solid lines), the mass of potassium cations estimated from charge accumulated in the film (colored area), and the difference attributed to water uptake (gray area). (B) The *reversible* mass changes measured by gravimetry during subsequent doping/dedoping cycles. Top: Voltage profile of scan cycles. Scan rate: 10 mV/s; the shadowed sections indicate the doping process. Middle: Mass changes of both BBL films. Bottom: Current density during CV cycles. (C) The normalized mass change of **BBL$_L$**, **BBL$_H$**, P3HT and P3MEEMT over the first four doping/dedoping cycles. Each polymer mass change was normalized to its maximum mass change and offset by 1.1.

During subsequent electrochemical cycles, the film shows a reversible mass change with a stable baseline (**Figure 2.2 B**). As expected, **Figure A.14** shows that upon electrochemical doping the **BBL$_H$** incorporates more charges, along with more mass uptake, which agrees with the volumetric capacitance difference. In addition, **BBL$_H$** takes up not only more cations (16% for **BBL$_H$** and 7.7% for **BBL$_L$**), but also more water molecules compared to the **BBL$_L$**. We convert this mass into the number of water molecules per cation. Considering the onset shift between two BBLs, we still observe that more water molecules are dragged into the film per cation in the **BBL$_H$** (20 to 30 waters) than in the **BBL$_L$** (5 to 7 waters) at a doped state. According to previous studies of the hydration shell in aqueous solutions,[92, 93] a potassium ion normally has a shell of ≈6 waters.

From this we conclude that the mass uptake in **BBL$_H$** must involve free/bulk water uptake upon doping, apart from the waters in the cation hydration shells.

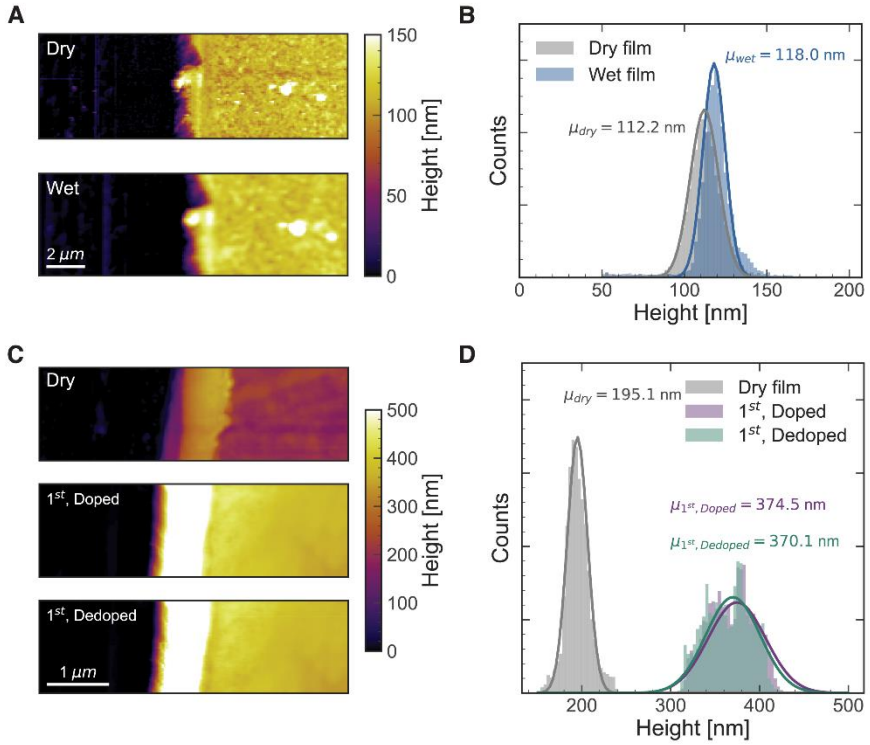

Figure 2.3 Operando AFM thickness determination upon the electrochemical process. (A) AFM height images and (B) height histogram of the **BBL$_H$** dry film (top) and wet film (bottom) of the same area at the scratch edge on Au substrates (left side) (C) AFM height images and (D) height histogram of the **BBL$_H$** dry film (top), *operando* doped film (middle, 500 mV), and *operando* dedoped film (bottom, −300 mV) of the same area during the first doping/dedoping cycle at the scratch edge on Au substrates (left side). The dry films were measured in air. The wet and *operando* doped/dedoped films were measured in 100 mmol/L KCl electrolyte. All height profiles were fitted to Gaussian distributions. Note that: AFM images (A) and (B) were measured on different samples, which introduces the thickness variance of dry films.

Furthermore, we investigate the same process in two other conjugated polymers, poly(3-hexylthiophene-2,5-diyl) (P3HT) and poly(3-thiophene-2,5-diyl) (P3MEEMT) (**Figure 2.2 C**). We choose P3HT and P3MEEMT to exemplify the typical swelling behavior: P3HT has been reported as an OECT material without hydrophilic side-chains in chaotropic anion electrolytes,[14, 31] while P3MEEMT is a derivative with the same backbone with glycol side-chains which exhibits

appreciable passive swelling.[14, 61, 94] In contrast to BBLs, neither P3HT nor P3MEEMT shows an irreversible mass retention after its first doping/dedoping cycle, even though maximum mass uptake of P3MEEMT in the first cycle is slightly different from the others.

Thus far, we have shown that both the commercial lower molecular mass and in-house synthesized higher molecular mass BBL polymers facilitate a fast, efficient bulk electrochemical doping along with a drastic ion/water mass uptake. Additionally, both BBLs, regardless of molecular mass, undergo a film hydration step driven by the first electrochemical doping cycle that is irreversible upon subsequent doping cycles but that is reversible upon drying the films. It is likely that BBL, as a side-chain-free ladder polymer, undergoes a unique hydration mechanism to overcome the trade-off of ionic and electronic transport. To further investigate the morphology and structural changes that accompany the hydration process of BBL, we focus on the high-performing **BBL$_H$** and employed both AFM-based techniques and GIWAXS measurement. First, we measured the film thickness changes with *operando* AFM upon *passive* and *active* swelling. **Figure 2.3 A,B** show the AFM images and height histograms of the pristine film before and after exposure to the electrolyte solution, without external bias. As probed via tapping mode AFM on the **BBL$_H$** under liquid, we observe negligible (≈5 %) swelling. This result of minimal swelling agrees with the previous QCM data showing a small, if any, mass change. However, on the other hand, **Figure 2.3 C,D** show that when the doping potential (500 mV) is first applied during the initial cycle, the film swells over ≈90% and becomes rougher. After dedoping the film back to the neutral state at −300 mV, the height of the film only decreases minimally by a few nanometers. Based on our previous eQCM result, we believe that the dramatic thickness increase observed here is a result of the initial film hydration during the first cycle, and the minimal shrinkage corresponds to the reversible active swelling.

Next, we investigate nanoscale morphology changes during active swelling using the AFM-based technique known as electrochemical strain microscopy (ESM). ESM has been used for probing nanoscale swelling due to the ion uptake in systems ranging from Li-ion battery materials[95-97] to conjugated polymers.[31, 47] We have previously applied it to reveal the spatial anticorrelation between ion uptake and the local crystallinity in p-type materials.[47] In ESM, an AC voltage is applied between the conductive tip and the polymer film in an electrolyte solution. Ion uptake due to the reduction/oxidation results in a local swelling, which is monitored at the contact resonance of the tip-sample interface. Because the frequency of the applied AC drive voltage is usually much faster than the full doping time for films, the observed local swelling under AC ESM is smaller than the swelling under DC conditions.[98-100] However, we can use ESM to probe the films under dynamic AC ion uptake at a range of different DC offset voltages.

Figure 2.4 A and **Figure A.16** show the ESM amplitude of the **BBL$_H$**, along with its topography image. Around the reduction onset potential, both films barely swell with an average amplitude of ≈500 pm. As we increase the tip bias, the ESM amplitude exhibits a larger swelling due to the ion/water injection into the film (**Figure 2.4 B**). At the highest potential (300 mV over threshold), the **BBL$_H$** swells by an average amplitude of 5.83 nm (4.9% swelling), which is a relatively large amount of AC swelling compared to other hydrophobic polymers like P3HT.[47] After doping at positive bias, then we scanned the DC tip bias offset to the dedoping condition and observed the amplitude decreasing back to a low level (<1%). This strong asymmetry in the ESM signal as a function of DC offset potential (i.e., swelling is observed only when the AC voltage takes the sample into a regime of electrochemical doping at one sign) confirms that the induced swelling is indeed the result of redox processes. Furthermore, we also operated the ESM measurements under different ionic concentrations (**Figure 2.4 C** and **Figure A.17**). As expected, the swelling tends to

be greater (larger ESM amplitude) in a more concentrated electrolyte. The swelling over the film becomes large and more heterogeneous with increasing bias, but the distribution of swelling volumes remains unimodal at all biases (**Figure 2.4 B**). This behavior contrasts notably with our previous study on P3HT films, which showed heterogeneous swelling according to the local degree of crystallinity and a clear bimodal distribution of swelling heights.[3] We interpret this result as a reflection of both more consistent uniformity in BBL films and penetration of water and ions into the film on the nano- to molecular scales.

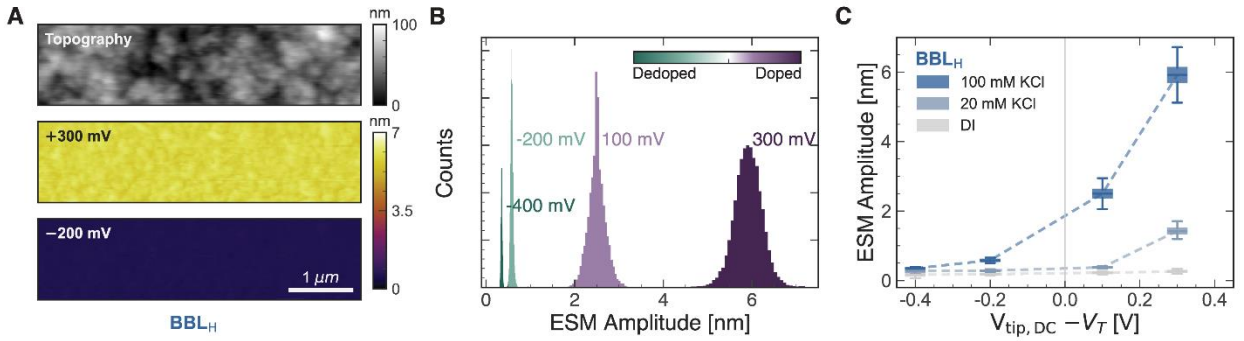

Figure 2.4 Film swelling upon electrochemical process via ESM. (A) Topography and ESM amplitude images of the **BBL$_H$** films in 100 mmol/L KCl at a 500 mV AC drive voltage. ESM images were taken with the tip at different DC potentials over the threshold (as labeled). The measurements were taken in a random potential order to avoid artificial shift of the baseline. (B) Histograms of the ESM amplitude of the same area under different bias conditions. (C) The ESM amplitude of **BBL$_H$** as a function of $V_{DC} - V_T$ taken in difference electrolyte concentrations. The dashed lines are used to guide the eye. The error bars represent one standard deviation of ESM amplitude distribution.

To probe molecular-level changes in film morphology upon ion-injection and water-uptake, we next carried out GIWAXS on **BBL$_H$** samples. Previous research by Inal and co-workers has explored the structural changes that occur upon doping with *ex-situ* GIWAXS.[23] However, Paulsen *et al.* and Flagg *et al.* have revealed that *ex-situ* GIWAXS, which probes the crystal structure under a dry film condition, may not capture the details of electrolyte swelling during operation.[44, 101, 102] Based on our previous eQCM data, we observed that BBL film undergoes a unique film swelling

compared to typical conjugated polymers, which is exactly why electrochemical doping mechanism remains unresolved.

Thus, we investigate the crystalline structure changes using *operando* GIWAXS on **BBL$_H$**. We utilized a modified blade coater to apply a potential and draw electrolyte across the sample as described elsewhere.[102] In **Figure 2.5 A**, we show the (100) lattice peaks as a function of electrolyte exposure and doping state. Before applying a bias, we first took the GIWAXS on the dry and wet BBL films after electrolyte exposure. The black trace ("dry") shows the initial out-of-plane (OOP) scattering of the dry film. Next, we performed one rolling drop passage while applying zero bias. As seen by the gray trace ("exposed"), exposure to the 100 mmol/L KCl does not change the lamellar spacing. However, upon application of a doping bias the lattice constant expands dramatically (≈31%), from 8.3 to 10.9 Å. This expansion is consistent with both our eQCM and *operando* AFM measurements showing that significant film swelling only occurs upon doping, not due to initial electrolyte exposure. Continued cycling of the film between doped (purple traces) and dedoped (green traces) does modulate the lamellar spacing, where the doped form of the polymer has a more expanded lattice than the undoped form, which is consistent with other doped polymers.[25, 102] Also, the lamellar spacing change between the doped and dedoped states in multiple cycles is reversible and reproducible (**Figure 2.5 C**). Nevertheless, as long as the films remain wet, the (100) spacing never returns to the spacing of the initial exposed film, again consistent with the eQCM data, which suggests irreversible water uptake on the first cycle. We note that the π–π lattice only minimally changes during this process (see **Figure A.18** and **Figure A.19**). Quantifying the swelling, we see the crystals only swelling ≈31 % volume by crystal expansion. However, we know the whole film is swelling ≈90 % in thickness; we therefore conclude that the majority of the swelling must be in the more amorphous regions of the BBL that

are not scattering strongly. In contrast to *operando* GIWAXS, we also operated *ex-situ* GIWAXS on the **BBL$_H$** (**Figure 2.5 C**, also **Figure A.20**). The d-spacing values extracted from both *ex-situ* and *operando* GIWAXS are summarized in

Table 2.2. The *ex-situ* GIWAXS results show minimal structural change (<5% expansion/contraction), which agrees with previous study on the commercial BBL.[23, 103] Obviously, the *ex-situ* GIWAXS significantly underestimates the lamellar expansion upon doping and fails to observe the ≈2.5 Å expansion due to water injection.

Table 2.2. The d-spacings measured via *ex-situ* and *operando* GIWAXS. (Unit: Å)

	pristine	**doped**	**dedoped**
In-plane (010)			
ex-situ	3.4	3.3	3.4
operando	3.4	3.3	3.3
Out-of-plane (100)			
ex-situ	8.3	8.5	8.3
operando	8.3	10.9	10.0

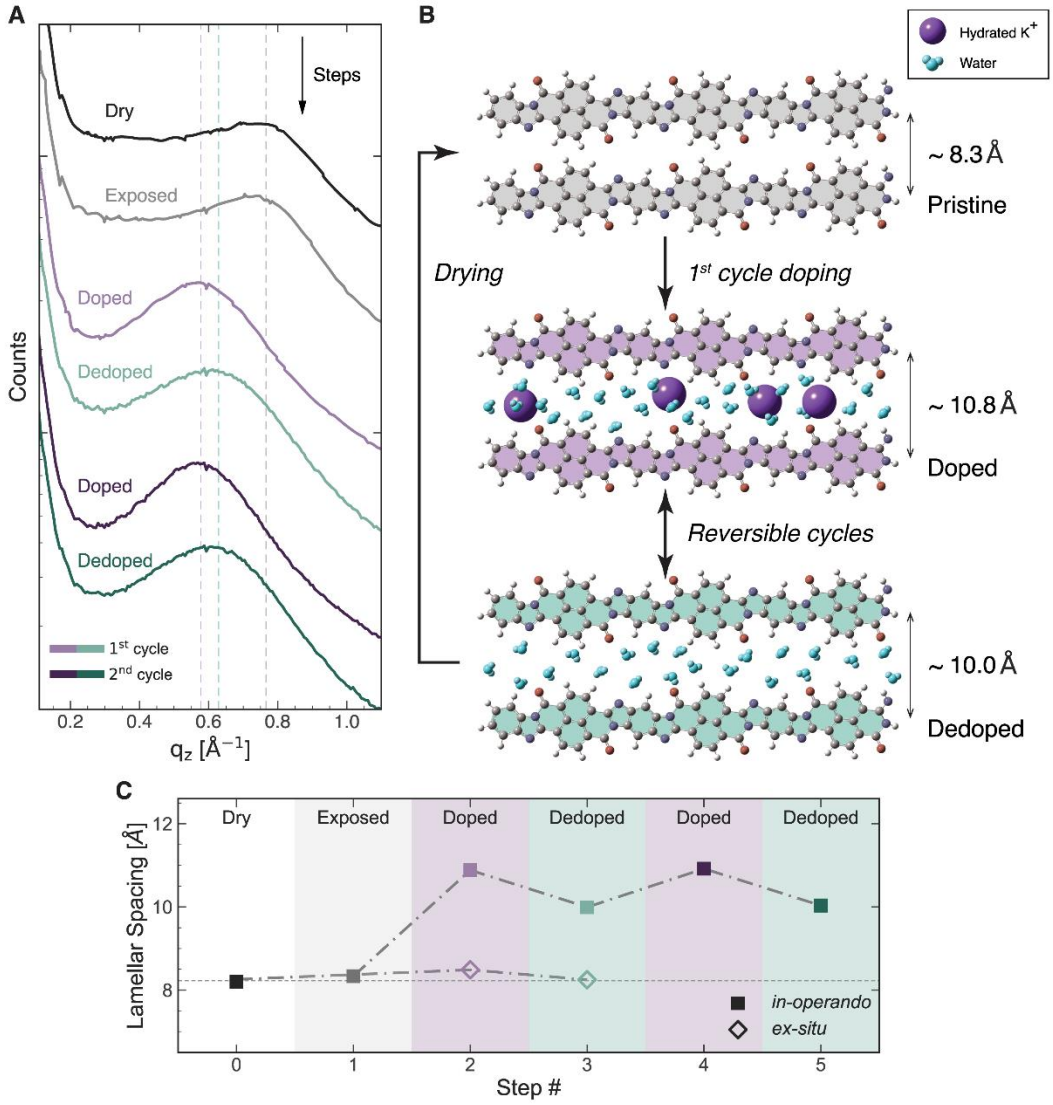

Figure 2.5 The structural change in BBL upon electrochemical process. (A) Out-of-plane (OOP) linecut profiles of *operando* GIWAXS patterns of **BBL$_H$** thin films under different film conditions. The dashed lines are used to guide the eye. (B) Schematic showing the polymer hydration mechanism during the electrochemical doping for BBL. The purple spheres are hydrated K^+, and cyan molecules are free waters. (C) The (100) lamellar spacing changes along the *operando* (solid) and *ex-situ* (open) GIWAXS doping/dedoping cycle steps. Purple traces/markers: doped states; green traces/markers: dedoped states.

Taking all these data together, we now propose a mechanism for how a hydrophobic ladder polymer like BBL performs as a fast operational OMIEC material (**Figure 2.5 B**). Upon exposure to the electrolyte, the hydrophobic BBL is resistant to water uptake and undergoes little if any

passive swelling. However, when the film is electrochemically doped under an applied potential for the first time, the counterions are accompanied by a large number of free water molecules and injected into both crystalline and amorphous domains in the film. Specifically in the crystalline regions, the lamellar spacing expands (≈31 %) much more than has been previously realized in BBL (≈1.1%),[23] facilitating ion and water injection. When the film gets dedoped, the cations leave the films, along with some of the water molecules. However, a large amount of the water remains in the film, resulting in an irreversible mass gain, film thickness increase, and crystalline lamellar spacing expansion. We further performed *operando* Raman spectroscopy to probe the chemical structure changes of BBL films during and after the first doping/dedoping cycle (**Figure A.21**). No significant peak change was found after the first doping/dedoping cycle, which indicates that the BBL backbone does not occur any chemical reactions with remaining waters. This model suggests that due to the hydrophobic backbones and absence of side-chains, BBL film first needs to get hydrated with the help of the cation movement driven by an electric field. After the waters are dragged in by cations, the carbonyl and amine groups along the backbones are sufficiently polar to retain the free water upon dedoping, which may not occur in a less polar backbone polymers. Even though the remaining waters slightly decrease the electronic mobility as verified by the OFET study in **Figure A.22**, they create a more hydrophilic microenvironment, facilitating a fast ion/water migration during the following doping/dedoping cycles. As a result, we see the switch ON or OFF time in milliseconds (**Table 2.1**). Furthermore, due to the rigid backbone of the ladder polymer, even after ≈31% lamellar expansion, the crystal structure is not significantly damaged such that the crystalline order is preserved on cycling to the dehydrated state after dedoping and drying, which enables good charge transport in a swelled film condition and good

stability (**Figure A.6**). To our knowledge, this is the first report of the unique film hydration activation process in a ladder polymer.

2.4 CONCLUSIONS

We explore the electrochemical doping process of the side-chain-free n-type ladder polymer BBL, comparing two different molecular mass versions: in-house synthesized **BBL$_H$** and commercial **BBL$_L$**. Like other conventional hydrophobic polymer films, BBL shows a minimal passive swelling when in contact with electrolytes. Surprisingly, without side-chains, BBL facilitates cation injection along with significant water uptake during active swelling. This water uptake occurs via a unique electrochemically irreversible swelling during the first doping step, followed by a reversible swelling/deswelling accompanying the subsequent doping/dedoping cycles. With the combination of *operando* AFM and *ex-situ* and *operando* GIWAXS, we studied the detailed structural change that occurs during electrochemical redox reactions in BBL. Importantly, these data provide concrete evidence that BBL incorporates water directly into the crystalline regions of the film via significant lamellar expansion of the BBL. We propose that, during the first doping step, the BBL film hydrates with the help of ion movement and then maintains a hydrophilic environment due to the water retention in both amorphous and crystalline domains. The first hydration step of BBL helps explain why the hydrophobic BBL polymers could still allow ion injections during doping. Except for the first cycle, the mass uptake in the following cycles shows no retention. As a result, BBL retains advantages of good reversibility and connectivity due to the lack of large-volume water-side-chain interactions. We also propose that some modest film swelling, separated from hydrated ion injection, may be beneficial for overcoming the trade-off between ionic and electronic transport for many applications ranging from biosensor to

neuromorphic computing devices and thus may provide a design template for the synthesis of next-generation OECT materials based on the lessons of BBL.

2.5 MATERIALS AND METHODS

2.5.1 *Materials*

Materials, including potassium chloride (KCl, Sigma-Aldrich, >99%), methanesulfonic acid (MSA, Sigma-Aldrich, > 99%), fluorine-doped tin oxide-coated glass (FTO, Sigma-Aldrich, 7 Ω/square), indium tin oxide-coated glass (ITO, Thin Film Devices), and commercial low molecular weight poly(benzimidazobenzophenanthroline) (BBL, Sigma-Aldrich) were purchased from the supplier noted and used as received. The in-house synthesized high molecular weight BBL was synthesized by Jenekhe Group, as detailed in previous studies.[104] The electrolyte was degassed by sparging N_2 into the solution for at least 10 min prior to all measurements in the aqueous solution. The BBL molecular weight was calculated from the intrinsic viscosity as reported before.[105]

2.5.2 *Sample preparation*

Both the commercial and in-house synthesized BBL were dissolved in MSA at 70 ℃ overnight with a concentration of 20 mg mL^{-1} and 4 mg mL^{-1}, respectively, to keep a similar film thickness. The polymer film was spin-coated at 1000 rpm (1 rpm = $2\pi/60$ rad s^{-1}) for 45 s from this hot solution in ambient air on a substrate. After spin-coating, the wet BBL films were immersed overnight in deionized water to remove the MSA residue. Then the films were transferred to a vacuum oven for 8 h at 60 ℃ to remove residual water.

2.5.3 *Dynamic light scattering (DLS)*

To estimate the molecular size, DLS measurements were performed with a Zetasizer Nano ZS analyzer (Malvern, UK, λ = 632.8 nm, θ = 175°). **BBL$_L$** and **BBL$_H$** samples were dissolved in MSA with a concentration of 0.4 mg mL^{-1}. A solvent viscosity of η_{MSA} = 11.7 mPa s and a refractive index n_{MSA} = 1.429 were used in the software calculations. All measurements were carried out at 25 °C and the results reported are averages of ten readings.

2.5.4 *Organic electrochemical transistor (OECT) devices*

OECT electrode substrates were fabricated using a photolithography process with a fixed channel length of 10 µm and channel widths ranging from 100 µm to 4000 µm (See **Figure A.1** for channel pattern geometries and dimensions). BBL films were prepared as above, via spin-coating, deionized (DI) water washing, and vacuum oven drying. After that, the polymer films were carefully removed via Texwipe and cotton tips under a microscope, leaving the coating only on the active channel area. The electrodes were subsequently insulated by a clear nail polish (Sally Hansen Insta-Dri Top Coat) to suppress the capacitance between the metal/electrolyte surface, as described in previous works.[49, 50] The measurement setup, including the OECT device, the PDMS reservoir, and the electrical connectors, were assembled via a custom 3D printed holder (**Figure A.1**). A standard Ag/AgCl pellet electrode (A-M Systems, Catalog # 550015) was used as a non-polarizable gate.

The OECT devices were measured using two Keithley 2400 source-measure units controlled by our custom Python code. 100 mmol/L aqueous KCl electrolyte was degassed by sparging with N_2 for at least 10 min, and all devices were cycled three times prior to measurement. The sweep rate was carefully selected to ensure steady-state doping conditions were achieved. Analysis was performed using our custom Python code.[49] The threshold voltage was extracted from the x-

intercept of the linear fitting of $I_D{}^{1/2}$ versus V_G as shown in **Figure A.3**. The transconductance values (g_m) were calculated from first derivative of the transfer curve. Python codes are available for download from the Ginger Group GitHub repository: *https://github.com/GingerLabUW/oect_processing* and *https://github.com/GingerLabUW/oect_control*.

The OECT transient behaviors were measured by pulsing the gate voltage between 0 V (OFF state) and 0.6 V (ON state). The drain current over time was fit to the biexponential function:

$$I_D = A_1\left(1 - e^{-t/\tau_1}\right) + A_2\left(1 - e^{-t/\tau_2}\right) \quad \textbf{(2-2)}$$

The switch OFF drain current over time was fit to the biexponential function:

$$I_D = A_1\left(e^{-t/\tau_1}\right) + A_2\left(e^{-t/\tau_2}\right). \quad \textbf{(2-3)}$$

We define the switch time constant as $A_1\tau_1 + A_2\tau_2$.

2.5.5 *Electrochemical Analysis*

Electrochemical analysis, including spectroelectrochemistry, electrochemical impedance spectroscopy (EIS), quartz crystal microbalance (QCM) and cyclic voltammetry (CV), were conducted with a three-electrode system, using Ag/AgCl as the reference electrode and a Pt mesh as the counter electrode. We used a Metrohm Autolab PDSTAT204 potentiostat to apply the film potential and the Metrohm NOVA software (Version 2.1.4) to control and communicate with external devices simultaneously. Note that the recorded potential in the three-electrode electrochemical configuration was defined by the applied potential vs. Ag/AgCl as a reference, while the gate voltage was applied to Ag/AgCl vs. the polymer film in the OECT setup. Here, we converted the electrochemical cell potential as the equivalent OECT gate potential.

For electrochemical impedance spectroscopy (EIS) and cyclic voltammetry (CV), we prepared BBL films on lithography patterned gold pads on glass substrates with defined areas (ranging from

0.01 cm^2 to 1 cm^2). CV measurements were carried out in 100 mmol/L KCl. The scan rate was 10 mV s^{-1}. In EIS measurements, the films were first electrochemically doped at a specific direct current (DC) potential (ranging from −0.2 V to −0.7 V *vs.* Ag/AgCl reference electrode) with the same three-electrode configuration. Then a small AC perturbation (a 10 mV sine wave) with a frequency from 10^5 Hz to 10^{-1} Hz was applied to the films. Once the spectra were recorded, we fit the EIS data to a modified Randles circuit model (see **Figure A.7**) using the Metrohm NOVA software or the Python *impedance.py*[106] package. The capacitance was extracted from a modified Randles circuit model,[27, 107] (R_s(R_p||CPE)), where R_s is the electrolyte resistance, CPE is a constant phase element for modeling polymer films, R_p is the charge transfer resistance of the polymer film. The capacitance values then were normalized by the film volumes to determine the volumetric capacitance (C^*). The thicknesses of the films were measured in their dry state by AFM.

2.5.6 *Spectroelectrochemistry*

For spectroelectrochemistry, we prepared BBL films on FTO substrates as described above. The films were cycled with three CV cycles prior to the measurement with the three-electrode configuration. The films were biased in 100 mmol/L KCl solution under different potentials for 60 s, and the currents were recorded simultaneously, which were later integrated to calculate the total injected charge. The UV–Vis spectra were collected with an integration time of 0.1 s per spectrum with an Agilent 8453 spectrometer.

2.5.7 *Quartz Crystal Microbalance (QCM)*

Measurements were performed using 1 in. diameter gold-coated AT quartz crystal (Stanford Research Systems, QCM-200 Crystals for Liquid Monitoring, 5 MHz) substrates on an SRS QCM200 instrument. The polymer films were patterned as the active gold area (≈0.40 cm^2). The

media difference between atmosphere and aqueous conditions needs to be taken into consideration. The baseline and film QCM signals were measured in both dry and wet environments to estimate the passive swelling. All films were soaked in their corresponding electrolytes overnight before QCM measurements on wet films, avoiding the baseline shifting during the measurements. After that, a typical CV measurement (scan rate: 50 mV/s) was carried out on the QCM crystal, and the current signals were also recorded simultaneously. Previous studies have shown that ≈100 nm thick polymer films could be considered as "rigid" films.[108, 109] So the mass change was calculated using the Sauerbrey equation in our study:

$$\Delta f = -C_f \Delta m \quad \textbf{(2-4)}$$

where Δf is the observed frequency change in Hz, Δm is the change in mass per unit area in g cm^{-2} and the C_f = 51.34 Hz μg^{-1} cm^2 (calibrated by galvanostatic silver deposition, see **Figure A.13**).

2.5.8 *Atomic Force Microscopy (AFM) based techniques*

In-situ atomic force microscopy (AFM) measurements and electrochemical strain microscopy (ESM) measurements were performed on an Asylum Research Cypher-ES instrument using gold-coated contact mode tips (Budget Sensors ContGB-G, ≈ 30 kHz, ≈ 2 N/m) under a nitrogen environment. The BBL films were spin-coated on a gold substrate. For the *in-situ* AFM measurement, the images were taken in a tapping mode immersed in 100 mmol/L KCl electrolyte. The external DC potential was applied between the sample substrate and the AFM tip. For the ESM measurement, we applied electrolyte between the tip and sample, and electrically grounded, while the tip was applied a drive bias, a combination of DC and AC voltage. The ESM amplitude at the contact resonance was monitored in dual-amplitude resonant frequency tracking (DART) mode with a 5 kHz width. The DC bias was varied from −300 mV to 500 mV and the AC bias

amplitude was fixed at 500 mV in the experiments. The applied DC was modulated to maintain the same efficient doping potential, ($V_{\text{applied}} - V_T$).

2.5.9 *Grazing incidence wide-angle scattering (GIWAXS)*

Ex situ GIWAXS measurements were performed on Beamline 7.3.3 at the Advanced Light Source (ALS) at Lawrence Berkeley National Laboratory using a Pilatus 2M area detector.[110] The images were taken with a beam energy of 10 keV and an incidence angle of 0.14° with 10 s exposure times. *Ex-situ* doped samples were reduced in 100 mmol/L KCl under –0.7 V for 60 s with an Ag/AgCl counter electrode, while *ex-situ* dedoped were doped first in 100 mmol/L KCl solution under –0.7 V and then dedoped at +0.5 V. All films were dried for 30 min in a helium atmosphere. *In situ* GIWAXS measurements were performed at the 11-BM CMS beamline at NSLS-II with a Pilatus 300K detector. A beam energy of 13.5 keV was used for all measurements. Rolling drop GIWAXS was performed as described in previous studies.[102] Traces are the average of the last 30 0.1 s exposures (for a total exposure of 3 s) after the blade and electrolyte meniscus has passed the sample. This allows for clean GIWAXS spectra without water scattering but maintains water contact and potential control through a lateral (≈3 mm) gate.

Data were processed using Nika and WAXStools in Igor Pro.[111] Peak positions and peak full width at half maximum (FWHM) were determined by fitting to Lorentzian peaks.

2.5.10 *Raman Spectroscopy*

Raman measurements of **BBL$_H$** film were carried out on a Thermo Scientific DXR2 Raman microscope. A 532-nm laser with a power of 1 mW was focused onto a sample surface through a 10x objective lens. The in-situ Raman spectra were taken during first doping/dedoping cycle and a Keithley 2400 was used to control the potential (V_G: +0.7 V to −0.3 V, 0.1 V per step). After the

first doping/dedoping cycle, the film was dried by blowing with a N_2 gun and Raman spectra were taken on the same spot to compare with the pristine dry film before depoing/dedoping cycle.

2.5.11 *Organic field-effect transistors (OFETs) fabrication and characterization*

OFET devices were fabricated in a typical top-contact and bottom-gate structure with a polystyrene (PS, $M_w \sim 280$ kg/mol) buffer layer as described in previous studies.[77, 112] The channel length (L) and width (W) were 100 and 1000 μm, respectively. The transistor characteristics were measured using two Keithley 2400 source-measure units (Keithley Instruments Inc., Cleveland, OH) controlled by custom Python code in a N_2-filled glovebox at room temperature. The saturation region field-effect electron mobility, μ_{OFET}, was calculated from the standard FET relationship:

$$I_{\mathrm{DS}} = \left(\frac{WC_{\mathrm{i}}}{2L}\right)\mu_{OFET}(V_{\mathrm{GS}} - V_{\mathrm{T}})^2 \qquad \textbf{(2-5)}$$

where I_{DS} is the drain current, C_{i} is the capacitance of gate insulator (10.6 nF/cm^2), V_{GS} is the gate voltage, and V_{T} is the threshold voltage. After the pre-cycle OFET measurement, the devices were then doped/dedoped in 100 mmol KCl with an external Ag/AgCl electrode as the gate. The post-cycle OFETs were then characterized after drying via a N_2 flow.

2.6 ACKNOWLEDGEMENTS

This project is based on research supported primarily by the National Science Foundation, DMR–2003456. In-house synthesis of BBL was supported by the NSF (DMR-2003518). L.Q.F. acknowledges the support of a NIST-National Research Council fellowship. Part of this work was conducted at the Washington Nanofabrication Facility/Molecular Analysis Facility, a National Nanotechnology Coordinated Infrastructure (NNCI) site at the University of Washington with partial support from the National Science Foundation via awards NNCI-1542101 and NNCI-2025489. The *ex-situ* GIWAXS in this research used beamline 7.3.3 of the Advanced Light Source

(ALS), which is a DOE Office of Science User Facility under contract no. DEAC02-05CH11231. The authors thank Chenhui Zhu and Eric Schaible at the ALS for assistance with GIWAXS data acquisition and analysis. The *operando* GIWAXS used beamline 11-BM (CMS) of the National Synchrotron Light Source, a U.S. Department of Energy (DOE) Office of Science User Facility operated for the DOE Office of Science by Brookhaven National Laboratory under contract no. DE-SC0012704. Certain commercial equipment, instruments, or materials are identified in this paper in order to specify the experimental procedure adequately. Such identification is not intended to imply recommendation or endorsement by the National Institute of Standards and Technology, nor is it intended to imply that the materials or equipment identified are necessarily the best available for the purpose.

Chapter 3. WHY ACCUMULATION MODE ORGANIC ELECTROCHEMICAL TRANSISTORS TURN OFF MUCH FASTER THAN THEY TURN ON

This chapter is from the submitted manuscript: Jiajie Guo, Shinya E. Chen, Rajiv Giridharagopal, Connor G. Bischak, Jonathan W. Onorato, Kangrong Yan, Ziqiu Shen, Chang-Zhi Li, Christine K. Luscombe, David S. Ginger. "Why accumulation mode organic electrochemical transistors turn off much faster than they turn on"

3.1 OVERVIEW

Understanding the factors underpinning device switching times is crucial for the implementation of organic electrochemical transistors (OECTs) in neuromorphic computing and real-time sensing applications. Existing models of device operation cannot explain the experimental observations that turn-off times are generally much faster than turn-on times in accumulation mode OECTs. Through operando optical microscopy, we image the local doping level of the transistor channel and show that device turn-on occurs in two stages, while turn-off occurs in one stage. We attribute the faster turn-off to a combination of engineering as well as physical and chemical factors including channel geometry, differences in doping and dedoping kinetics, and the physical phenomena of carrier density-dependent mobility. We show that ion transport is limiting the device operation speed in our model devices. Our study provides insights into the kinetics of OECTs and guidelines for engineering faster OECTs.

3.2 INTRODUCTION

Organic electrochemical transistors (OECTs) are currently being explored for applications including bioelectronics,[113-116] logic circuit elements,[117, 118] and neuromorphic devices.[59, 119-121] As

a class of transistors, OECTs feature high transconductance (≈ mS),[122] low operation voltage (typically < |1 V|),[122] and direct response to biologically relevant ions[123, 124] and neurotransmitters.[125, 126] The typically soft and flexible nature of organic semiconductors used in OECTs enables the detection of action potentials[114, 127] and opens the window for applications in brain-machine interfaces and in vivo sensing.[128-130] To unleash the full potential of OECTs, a deeper understanding of the fundamental transistor operation mechanism is necessary, especially transistor switching behaviors, which are critical to the training phase of neuromorphic computing and simulating behaviors of arrays of transistors and their scaling properties.[131, 132]

In OECTs, organic semiconductors — also referred to as organic mixed ionic-electronic conductors (OMIECs) in this context — are used as channel active layers, with the most common materials being conjugated polymers.[6, 8, 133-135] The conductivity of an OECT is modulated by the electrochemical gate potential, which controls the doping level (redox state) of the conjugated polymer channel. Importantly, in contrast to conventional field-effect transistors (FETs), OECTs exhibit volumetric doping: the gate voltage changes the conductivity of the entire volume of the transistor channel, rather than just the surface layer, and counterions injected from the electrolyte provide charge compensation for injected electronic carriers.[136] At steady-state, the channel current (I_D) is governed by both carrier mobility and carrier density. The steady-state behavior of OECTs has been relatively well studied.[6, 135, 137, 138] To benchmark the device performance, the product of electronic mobility and volumetric capacitance, μC^*, has been recognized as the material figure of merit of OECT in steady-state operation.[139]

Compared to the steady-state performance, our current knowledge of OECT kinetics is limited.[138] For example, the switching speed for materials with identical μC^* can vary by many orders of magnitude.[140] Understanding the switching behaviors of OECTs is crucial for designing

logic units as well as emulating and sensing neural activity, which typically operates at the frequency of ≈ 100 Hz.[127] The widely-used Bernards model describes the transient behavior with an equivalent RC circuit as the ionic path and makes the quasistatic approximation for the channel charge distribution.[137] Several improved models based on the original Bernards model have been proposed with more complex equivalent circuits describing the ionic circuit.[141, 142] Recently, Paudel *et al.*[143] demonstrated a 2D-finite element model based on drift-diffusion process and shows the existence of the lateral ion current during switching, which is neglected in the traditional model. However, it should be noted that all these kinetics studies are based on poly(3,4-ethylenedioxythiophene):poly(styrene sulfonate) (PEDOT:PSS), which operates as a depletion mode OECT, with the transistor in the on-state when no gate potential is applied. The transient response of PEDOT:PSS-based OECTs may not be directly comparable to accumulation mode OECTs. Accumulation-mode OECTs are generally more favorable for practical applications because of their comparatively lower energy-consumption, particularly for in vivo bioelectronics and neuromorphic computing. Nevertheless, to our best of knowledge, no studies have yet to systematically discuss the transient response and device turn-on/turn-off kinetics of accumulation mode OECTs.

In this project, we study the asymmetric transient behavior of accumulation mode OECTs. Through operando optical microscopy coupled with OECT characterization, we find that OECT turn-on occurs in two distinguishable stages: (1) doping front propagation and (2) vertical doping. In contrast, device turn-off occurs in one continuous stage. We further identify the factors that contribute to the rapid OECT turn-off behavior including typical faster dedoping kinetics of conjugated polymers compared to their doping kinetics, the channel geometry, and the carrier density-dependent mobility. Combining these observations, we propose an empirical model

describing the switching behavior of accumulation mode OECTs and provide physical interpretations to the response time constants. Lastly, we show that ion transport is the limiting factor to device kinetics, and we offer guidance for engineering faster accumulation mode OECTs from both materials and device perspective.

3.3 RESULTS AND DISCUSSION

3.3.1 *Asymmetric OECT response times*

Figure 3.1 a shows a typical transient response of an accumulation mode OECT: the transistor is turned on (higher $|I_D|$) upon gate potential applied and is turned off upon potential removal. We first tried the Bernards model[137] to describe the transistor switching behavior (See Appendix **B.1**). The Bernards model expresses the variation of I_D over time as a single exponential function upon a square V_G pulse, with one RC time constant related to ion transport into the channel polymer.[137] We found that Bernards model fails to predict the transient response of accumulation mode OECTs from three aspects: (1) the initial transistor turn-on, which manifests as a short delay (**Figure 3.1 a**, bottom left) rather than instant turn-on, cannot be well-captured; (2) the transistor turn-on cannot be described with a single exponential function; (3) the difference in transistor switching-on and switching-off times cannot be described (**Figure 3.1 a**). These issues, especially the difference in transistor switching times, cannot be resolved even if the improved models are applied, which focus more on interpreting the pre-exponential factor.[141, 142]

Figure 3.1 b and **Table 3.1** display the turn-on and turn-off times of accumulation mode OECTs from both this paper and our literature survey. We considered published results with typical planar structure and aqueous electrolyte, which is the most common OECT structure to date. **Figure 3.1 b** shows that faster device turn-off compared to turn-on is indeed ubiquitous, though rarely discussed aside from limited reports on PEDOT:PSS.[144]

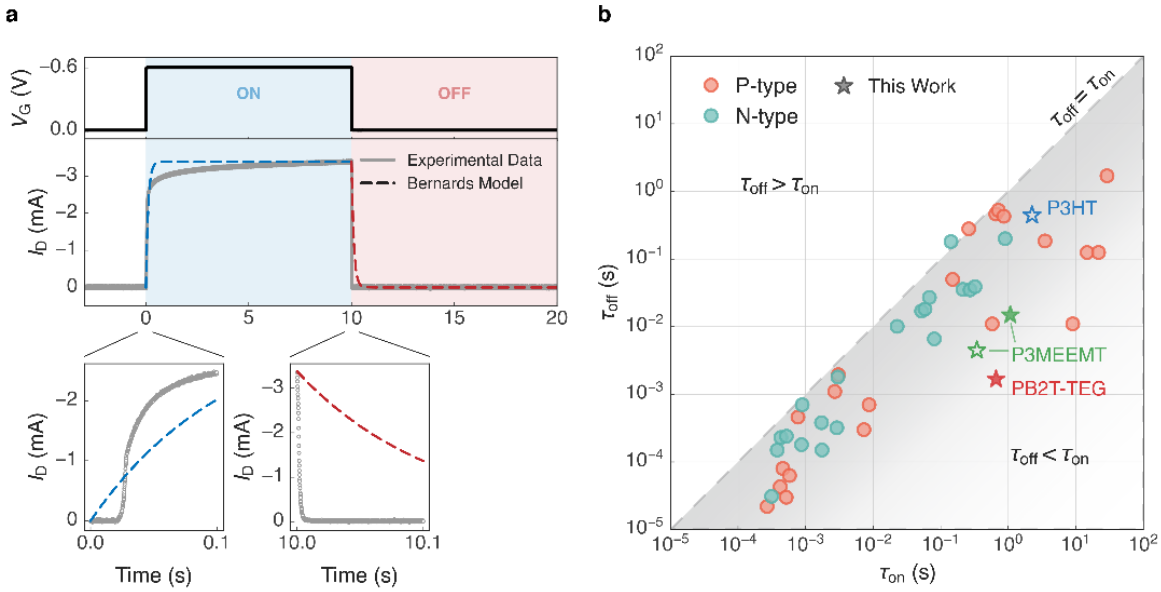

Figure 3.1 OECT response times. a, Transient response of a typical accumulation mode OECT (solid) and the fit with Bernards model (dashed). The initial stage of transistor turn-on and turn-off are magnified for clarification. **b**, Accumulation mode OECT response times in literatures. Each point represents one polymer-electrolyte pair. Detailed response times and references are listed in Table 1. The device response times measured in this work with carefully chosen gate voltage considering threshold voltage are represented as star symbols, which are PB2T-TEG (0.1 M KCl), P3MEEMT (0.1 M KCl), P3MEEMT (0.1 M KTFSI) and P3HT (0.1 M KTFSI). Solid and unfilled stars represent devices operated in 0.1 M KCl electrolyte and 0.1M KTFSI electrolyte, respectively.

Table 3.1 Accumulation mode OECT response times in literatures

Polymer	Type	Ion Concentration (mM)	Ion Type	τ_{on} (ms)	τ_{off} (ms)	Reference	Note
gDPP-g2T	p	PBS buffer	PBS buffer	0.269	0.022	[117]	cOECT
p(g2T-TT)	p	100	NaCl	0.42	0.043	[11]	
P(gTDPPT)	p	100	NaCl	0.46	0.08	[15]	
P(bgDPP-MeOT2)	p	100	NaCl	0.516	0.03	[145]	
P(lgDPP-MeOT2)	p	100	NaCl	0.578	0.063	[145]	
p(gPyDPP-MeOT2)	p	100	NaCl	0.77	0.46	[146]	
PBBTL	p	100	NaCl	2.7	1.1	[147]	
PBBTL/BBL blend	p	100	NaCl	3.05	1.95	[147]	
TDPP-gTVT	p	100	NaCl	7.3	0.3	[148]	
TDPP-gTBTT	p	100	NaCl	8.7	0.7	[148]	
PProDOT-DPP	p	100	LiCl	150	50	[149]	
PProDOT-DPP	p	100	$LiPF_6$	260	280	[149]	
P3APPT	p	100	KPF_6	580	11	[13]	estimation
PIBET-AO	p	50	KCl + $CaCl_2$	654	463	[150]	
PIBET-O	p	50	KCl + $CaCl_2$	714	526	[150]	
PIBET-BO	p	50	KCl + $CaCl_2$	862	429	[150]	
PIBT-BO	p	50	KCl + $CaCl_2$	3500	185	[150]	
P3APPT	p	100	KCl	9000	11	[13]	estimation
DPP-DTT (8:2)	p	100	KPF_6	14705	125	[151]	400 μm, estimation
DPP-DTT (1:0)	p	100	KPF_6	21739	125	[151]	400 μm, estimation
PIBET-A	p	50	KCl + $CaCl_2$	29000	1700	[150]	
Polymer	Type	Ion Concentration (mM)	Ion Type	τ_{on} (ms)	τ_{off} (ms)	Reference	Note
Homo-gDPP	n	PBS buffer	PBS buffer	0.313	0.031	[117]	cOECT
BBL_{152}	n	100	NaCl	0.38	0.15	[152]	
BBL_{98}	n	100	NaCl	0.43	0.23	[152]	
BBL_{60}	n	100	NaCl	0.52	0.24	[152]	
gNDI-T	n	100	KCl	0.87	0.18	[153]	normalized to area
BBL_{15}	n	100	NaCl	0.89	0.7	[152]	
PBBTL/BBL blend	n	100	NaCl	1.72	0.38	[147]	
P(gTDPP2FT)	n	100	NaCl	1.75	0.15	[15]	
gNDI-V	n	100	KCl	2.9	0.32	[153]	normalized to area
P(gPzDPP-CT2)	n	100	NaCl	3	1.8	[154]	
P(gPzDPP-2T)	n	100	NaCl	22.7	10.1	[154]	
f-BTI2g-TVTCN	n	100	NaCl	52	17	[155]	
gAIID-2FT	n	100	NaCl	58.5	18.2	[156]	
f-BTI2g-TVT	n	100	NaCl	68	27	[155]	
BBL_H	n	100	KCl	80.3	6.6	[26]	
BBL_L	n	100	KCl	142	181	[26]	
gAIID-T	n	100	NaCl	213.3	35.6	[156]	
f-BTI2TEG-FT	n	100	NaCl	272	35	[157]	
f-BTI2TEG-T	n	100	NaCl	322	39	[157]	
BBL	n	100	NaCl	900	200	[158]	estimation

One hypothesis is that this asymmetry could arise from the switching potentials chosen. Based on the Butler–Volmer model, the electrochemical reaction rate is influenced by the activation potential.[159-161] Since the threshold voltage (V_T) varies with different polymer-electrolyte systems, it is possible that the faster turn-off is the result of smaller voltage difference between V_{on} and V_T compared to V_{off} and V_T, namely, $|V_{on} - V_T| < |V_{off} - V_T|$. To rule out the influence of the mismatch between switching on and off gate potentials, we selected three p-type polymers as examples and carefully tested their OECT kinetics with fixed voltage difference between V_T and switching potentials. The three conjugated polymers studied here are: poly[2,5-bis-(thiophenyl)-1,4-bis(2-(2-(2-methoxyethoxy)ethoxy)ethoxy)-benzene] (PB2T-TEG), poly(3-{[2-(2-methoxyethoxy) ethoxy]methyl}-thiophene-2,5-diyl) (P3MEEMT), and poly(3-hexylthiophene-2,5-diyl) (P3HT); and the two aqueous electrolytes are: potassium chloride (KCl) and potassium trifluoromethanesulfonimide (KTFSI). The chemical structure of the polymers and the device performance are shown in **Figure B.1**. After considering threshold voltage, we still observed faster turn-off behavior (**Figure 3.1 b**, stars). Clearly, the faster turn-off is not caused by the mismatch between switching potentials, and the asymmetry in OECT switching times may be related to other factors such as polymer doping and dedoping kinetics or device geometry.

3.3.2 *Comparison between OECT and spectroelectrochemistry*

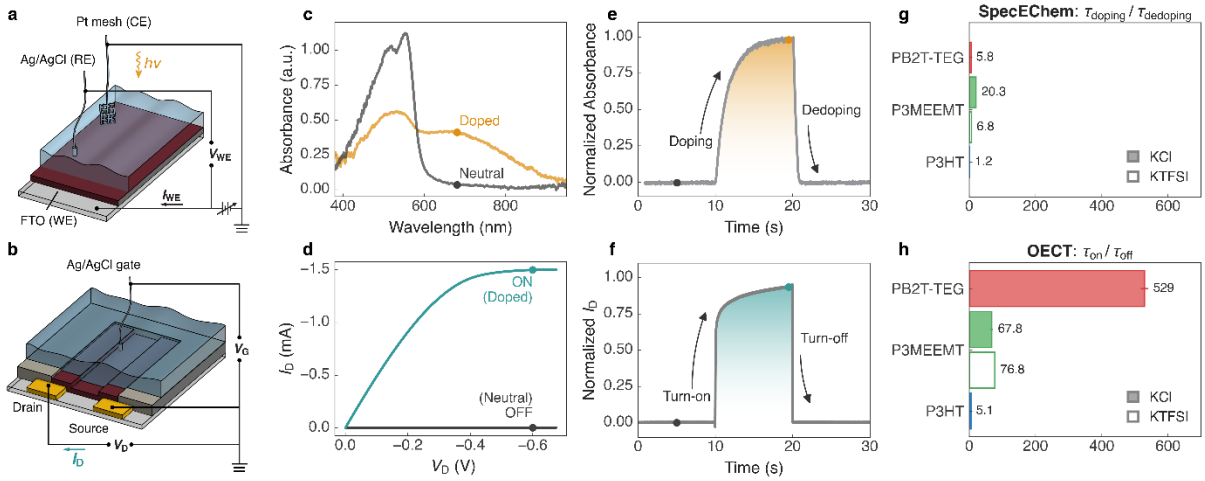

Figure 3.2 Comparison between OECT and UV-Vis spectroelectrochemistry a,**b**, Schematic diagram of spectroelectrochemistry (SpecEChem) (a) and OECT (b) experimental setups. **c**,**d**, Typical UV-Vis spectra (c) and OECT output curves (d) of two steady-states (neutral/doped). **e**,**f**, An example transient response of spectroelectrochemistry (**e**) at polaron peak absorption wavelength (680 nm) and OECT (**f**) at saturation region (V_D = −0.6 V). **g**,**h**, The $\tau_{doping}/\tau_{dedoping}$ measured in spectroelectrochemistry (**g**) and the τ_{on}/τ_{off} measured in OECT (**h**) for: PB2T-TEG and P3MEEMT with 0.1 M KCl (solid); P3MEEMT and P3HT with 0.1 M KTFSI (unfilled) The doping-voltage for spectroelectrochemistry, V_{doping} = OCP + 0.2 V, and the dedoping-voltage, $V_{dedoping}$ = OCP − 0.2 V. The on-voltage for OECT, $V_{on} = V_T$ − 0.2 V, and the off-voltage, $V_{off} = V_T$ + 0.2 V. Time resolution of spectroelectrochemistry is ≈ 10 ms and OECT is ≈ 10 μs. Error bars represent standard error of the mean from multiple cycles.

Because the magnitude of I_D is closely related to the electrochemical doping level of the channel conjugated polymer, it is possible that faster OECT turn-off is the consequence of rapid electrochemical dedoping nature of the polymer. To verify this hypothesis, we compared the doping and dedoping kinetics of spectroelectrochemistry (two-terminal diodes) to the turn-on and turn-off speed of OECTs (three-terminal transistors). **Figure 3.2 a,b** display the geometries of the spectroelectrochemistry and OECT measurements. **Figure 3.2 c** shows the steady-state UV-Vis spectra, which provides information on the electronic states of the conjugated polymers. When electrochemically doped, the polymer is oxidized along with the formation of a polaron, resulting

in the bleaching of the π-π* transition peak (≈ 525 nm) and the increase of the polaron peak (≈ 680 nm). **Figure 3.2 d** shows the transistor output curves associated with the on-state (doped) and the off-state (neutral). In addition to the steady-state study, the time-resolved UV-Vis spectra provide the rate of polaron formation and removal, which we expressed as the time constants: τ_{doping} and $\tau_{dedoping}$. We obtained the time constants from exponential fittings of polaron absorption peak over time (**Figure 3.2 e, Figure B.2 and Figure B.3**). Below, we referred to similar time constants from the transient response of OECT switching as τ_{on} and τ_{off} in order to distinguish them from the spectroelectrochemistry time constants (**Figure 3.2 f**, **Figure B.2 and Figure B.3**). Given the effect of the activation potential discussed in the previous section, we carefully measured the operando UV-Vis spectra under the same potential difference with respect to the equilibrium potential, or open circuit potential (OCP). The V_T and OCP values are listed in **Table B.1**.

Figure 3.2 g,h summarize the ratios of $\tau_{doping}/\tau_{dedoping}$ (spectroelectrochemistry) and τ_{on}/τ_{off} (OECT) of four polymer-electrolyte pairs, respectively. We showed that, in both spectroelectrochemistry and OECT, the processes involving polymer doping are slower than the ones associated with polymer dedoping. However, across all polymers and electrolytes, the switching difference between these two processes is much larger in OECTs compared to spectroelectrochemistry. **Table B.2** reports the collected response times. Interestingly, we found that the timescale of OECT turn-on is comparable to the timescale for spectroelectrochemical doping, while OECT turn-off is much faster than spectroelectrochemical dedoping (approximately 10-100x faster). These results suggest that faster OECT turn-off is not simply due to faster polymer dedoping. We next turn to explore the possible causes.

3.3.3 *Operando microscopy characterization*

To further understand the origin of faster device turn-off in accumulation mode OECTs, we probed the electrochemical doping level of channel conjugated polymer via operando optical microscopy coupled with a 650 nm long pass filter to selectively monitor polaron formation (**Figure 3.3 a**). **Figure 3.3 b** shows the transient response of I_D and I_G during transistor turn-on. We observed an immediate I_G response to the V_{on}, which shows a typical spiking and decay behavior, suggesting ion injection from the electrolyte into the channel polymer. In contrast, I_D remains relatively low initially after V_{on} applied, which to our knowledge, has not been discussed previously. **Figure 3.3 c** shows the microscope movie screenshots during turn-on. Darker pixels represent more polaron absorption and thus a higher electrochemical doping level. We found that OECT device turn-on occurs in two stages: (1) a *doping front propagation* stage and (2) a *vertical doping* stage. We provide detailed discussions of each stage in the following paragraphs.

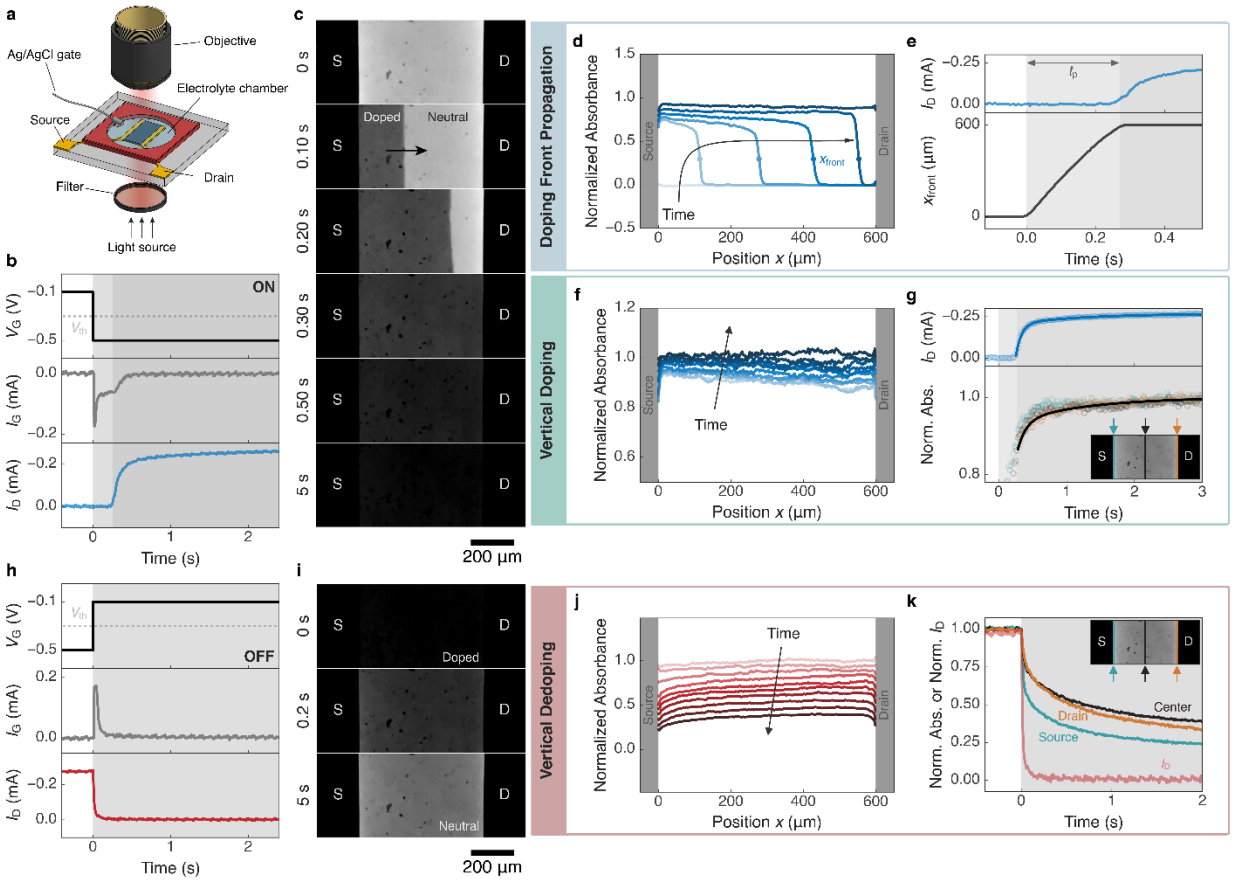

Figure 3.3 Operando optical microscope coupled with OECT switching. **a**, Operando optical microscope setup schematics. **b**, Potential and current response during turn-on. **c**, Microscope movie screenshots during turn-on with timestamp labels. Darker pixel represents higher polaron concentration. **d**, Normalized polaron absorption along channel over time during *doping front propagation* stage (stage 1 in turn-on). **e**, Comparison of I_D and moving front position over time during *doping front propagation* stage. **f**, Normalized polaron absorption along channel over time during *vertical doping* stage (stage 2 in turn-on). **g**, Comparison of I_D and normalized polaron absorption over time at selected positions during *vertical doping* stage. The solid lines indicate the fits. The insert image shows the selected positions over the channel. **h**, Potential and current response during turn-off. **i**, Microscope movie screenshots during turn-off with timestamp labels. **j**, Normalized polaron absorption along channel over time during turn-off, or *vertical dedoping*. **k**, Comparison of normalized I_D and normalized polaron absorption at three selected positions over time. The insert image shows the selected positions over the channel (labeled as source, center and drain). A 650 nm long pass filter was used, and the red channel intensity is used to calculate the polaron absorbance. The polymer used here is PB2T-TEG, and the electrolyte is 0.1 M KCl. The transistor channel length is 600 μm, and the film thickness is ≈ 120 nm. The drain potential is fixed at -0.6 V.

During the *doping front propagation* stage, we found that even though substantial doping of the channel polymer is already occurring, the growth of the I_D starts only after the doping front position (x_{front}) reaches the drain electrode (**Figure 3.3 d,e**). We thus introduce the doping front propagation time, t_p, as the time required for the doping front to propagate across the entire channel from the source to the drain electrode, with the value of ≈ 270 ms for this particular device (L = 600 μm). We defined x_{front} as the position of the peak of the first derivative of the absorbance. **Figure 3.3 e** shows the relatively linear relation between x_{front} and time, suggesting the front is moving at a constant speed, which is ≈ 2.2 μm/ms in this case. The fact that we observed the doping front propagating from the source to drain electrode suggests that the injection of electronic carriers is occurring primarily from the source electrode during device turn-on. This result makes sense considering p-type OECTs are typically operated at negative V_G and V_D, and electron removal (or hole injection) from channel conjugated polymer (polymer oxidation) will naturally favor the grounded source electrode instead of negatively biased drain electrode. In addition, we note that this doping front propagation stage (I_D remains relatively low after V_{on} applied) may be overlooked if transient response is characterized without enough sampling rate.

In the *vertical doping* stage, we observed a similar speed of doping of the polymer in the center of the channel and near both electrodes (**Figure 3.3 f,g**). We found the speed of I_D increase (τ_{OECT} ≈ 290 ms) and polymer doping (τ_{SpecE} ≈ 200 ms) is at the same order of magnitude, suggesting the I_D increment is largely dominated by the increase of doping level (or carrier density) along the channel with the underlying polymer acting as an increasingly conductive, planar electrode. **Figure 3.3** shows data from PB2T-TEG, a polymer that undergoes a distinct structural phase transition upon doping.[162] While the ion-induced phase transition in PB2T-TEG provides an easily resolvable doping front for kinetic analysis, we found the two-stage behavior of a doping front

propagation followed by a vertical doping, is a general across accumulation mode OECT behavior regardless of cycle numbers, active layer material, or channel length (**Figure B.4**).

For the OECT device turn-off, or the *vertical dedoping* stage, we observed an immediate response of both I_D and I_G to the V_{off} (**Figure 3.3 h**). We did not observe any front propagation event compared to turn-on. **Figure 3.3 i,j** display the polymer dedoping process along the channel. While we did not see a clear dedoping front, quantitative analysis of the microscope images shows that polymer does dedope faster near the source electrode than other positions in the channel (**Figure 3.3 k**). This finding partly explains the faster OECT turn-off. The conductive channel is broken by the dedoping of a thin slice near the electrode: if we consider the transistor channel as a series of resistors, as long as the resistance of one of the resistors increases (the polymer near source electrode), the total resistance will increase and thus result in the decrease in I_D. Nevertheless, this explanation must be incomplete, as the turn-off speed of I_D is *still* much faster than the dedoping speed of polymer near source electrode. As a corollary of this behavior, we found that even though the transistor is in the off-state already, dedoping of the channel polymer is not fully completed as noted by the absorbance in the polaron band (**Figure 3.3 k**). This phenomenon suggests that, through shortening the off-interval (or increased duty), faster OECT turn-on in the subsequent cycle can be readily achievable, as the channel polymer is already in slightly doped state (**Appendix B.2**). We speculate that this behavior may be useful in particular for designing OECT-based spiking neural networks[119, 120] and emulating neuron dynamic filtering function.[163, 164] We next considered whether carrier-density dependent mobility can account for the remaining acceleration of the turn-off time.

3.3.4 *Carrier density-dependent mobility*

Figure 3.4 a shows the transient response of the I_D, carrier density and average carrier mobility during the transistor turn-off. We calculated the carrier density using both the integral of gate current over time and average polaron absorbance along the channel during the vertical dedoping stage and both results are in good agreement (**Figure B.5**). We then estimated the average hole mobility in the channel during turn-off via:

$$\mu = \left(\frac{L}{W \cdot d \cdot e \cdot V_D}\right) \cdot \frac{I_D}{p} \quad \textbf{(3-1)}$$

assuming a linear electric field along the channel, where μ is the average carrier mobility, p is the hole density, e is the electron charge and V_D is the drain voltage. L, W, and d represent channel length, width, and thickness, respectively. We found the turn-off rate of I_D is comparable to the rate of the carrier mobility decay, which, due to the non-linear relationship between density and mobility in conjugated polymers, is about one order of magnitude faster than the carrier removal rate. This result agrees with what we have observed previously that the OECT turn-off speed is about an order of magnitude faster than polymer dedoping speed measured by spectroelectrochemistry (**Table B.2**).

Figure 3.4 b shows the calculated carrier mobility and extracted carrier density relation required to explain our data. We found that carrier mobility is indeed carrier density-dependent, especially in the high carrier density region. Previously, Friedlein et al. had demonstrated that the steady-state OECT performance could be well characterized if carrier density-dependent mobility is considered, with the relation between mobility and density being:

$$\mu = \mu_0 \cdot \left(\frac{p}{p_0}\right)^{\frac{E_0}{k_B T}-1} \quad \textbf{(3-2)}$$

where μ_0 is mobility prefactor and p_0 is zero-filed hole concentration. E_0 describes the energetic width of the tail of the density of states, k_B is Boltzmann's constant and T is temperature.[165] This equation captures the filling of the density of states (DOS) due to energetic disorder in conjugated polymer materials.[166] We found this relation also fits our carrier mobility and density data well. **Appendix B.3** describes detailed fittings and discussions of **Equation (3-2)**. We concluded that the carrier density-dependent mobility explains why the OECT turn-off is even faster than the dedoping of polymer near source electrode: not only carrier density, but also the carrier mobility decreases significantly at the initial stage of device turn-off, and both carrier mobility and carrier density contribute to I_D.

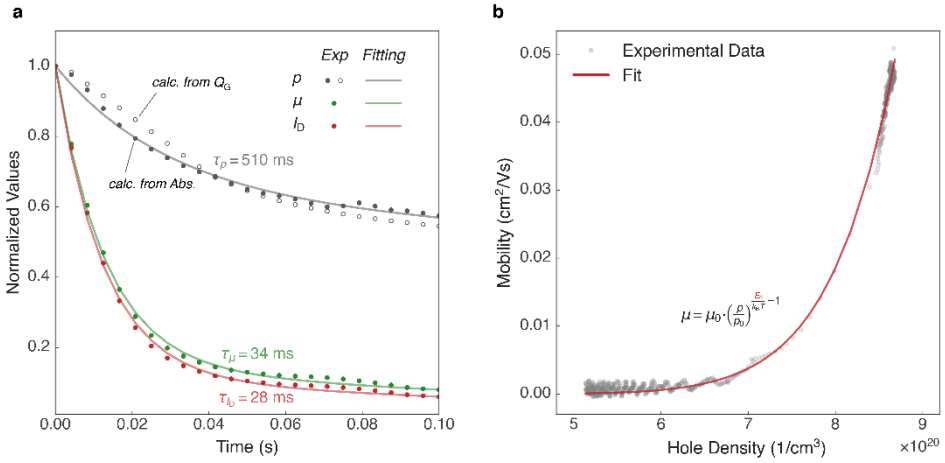

Figure 3.4 OECT mobility and carrier density a, Transient response of I_D, carrier density and average carrier mobility during the PB2T-TEG transistor turn-off. Solid line indicates the fit with biexponential equation. **b**, Calculated carrier mobility as a function of carrier density using eqn (1). Solid line indicates the fit with the eqn (2). The good fit of the classic density-dependent mobility formula to the experimental data based on the measured current and carrier density suggests the importance of carrier density-dependent mobility in explaining the rapid turn-off of OECTs.

3.3.5 *Engineering faster OECTs*

With the transient behavior knowledge from operando microscopy, we expressed the two-stage turn-on with an empirical biexponential equation including the initial front propagation time (t_p):

$$\left|I_{\mathrm{D,\,Norm}}(t)\right| = A_1 \cdot \left(1 - e^{-\frac{t-t_p}{\tau_{1,on}}}\right) + A_2 \cdot \left(1 - e^{-\frac{t-t_p}{\tau_{2,on}}}\right);\ A_1 + A_2 = 1 \qquad \textbf{(3-3)}$$

where $\tau_{1,\,on}$ and $\tau_{2,\,on}$ are time constants associated with the vertical doping stage. A_1 and A_2 are two constants with the value of A_1 typically ≈ 0.7 (**Figure 3.5 a**). For one-stage transistor turn-off, we described I_D as:

$$\left|I_{\mathrm{D,\,Norm}}(t)\right| = e^{-\frac{t}{\tau_{\mathrm{off}}}} \qquad \textbf{(3-4)}$$

where τ_{off} is the time constant expressing vertical dedoping (**Figure 3.5 a**).

To understand how the factors in Eqn. 3 depend on experimental conditions, we next studied how operation variables including potential and device geometry affect OECT switching behavior (**Figure 3.5 b**–**e** and **Figure B.6** – **Figure B.12**). During the *doping front propagation* stage, we found smaller t_p with shorter channel length as expected because the doping front is propagating at a relative constant speed. Surprisingly, we found t_p is relatively independent of the drain potential. This result suggests that ion transport from electrolyte into the polymer channel, instead of electronic transport from the source electrode, is limiting the front propagation speed. Indeed, we found faster front propagation (smaller t_p values) with higher gate potentials, as the increased gate potential speeds up ion movement. We further demonstrated smaller t_p with increased ion concentration, thinner channel active layer and bulky anion,[13, 167] all associated with shorter ion transport time from electrolyte into polymer channel.

In the *vertical doping* and *vertical dedoping* stages, we found a similar trend of $\tau_{1,\,on}$ and τ_{off} compared to t_p, namely, smaller $\tau_{1,\,on}$ and τ_{off} if the ion transport time from electrolyte into polymer layer is reduced (higher gate potential, increased ion concentration, thinner polymer layer and bulky anion[13, 167]). We hypothesize that smaller $\tau_{1,\,on}$ and τ_{off} with shorter channel length is akin to charging and discharging a capacitor, where smaller capacitance (shorter channel length) results

in faster charging and discharging. In contrast, the slower $\tau_{2,\,on}$, with the magnitude of ≈ 2-3 s, is less dependent on all operation variables. We propose that $\tau_{2,\,on}$ is associated with polymer structural relaxation or ionic/electronic charge reorganization, as recently suggested by Wu et al.[24] In addition, we noticed that when $|V_G - V_T| > |V_D|$, or when the device is operated in the linear region (shadowed area in **Figure 3.5** and **Figure B.13**), the difference between turn-on and turn-off response time becomes smaller. This result is reasonable as the transistor behaves like a diode-like spectroelectrochemistry device when drain potential is decreased.

Finally, we demonstrated a SPICE circuit model that accurately reflects transient asymmetry of accumulation mode OECTs by incorporating a time-dependent channel resistor into the existing model.[142, 168] The detailed SPICE simulation methods and results are in **Appendix** SPICE simulation**B.4**. To sum up, from the device perspective, shorter channel length, thinner polymer layer and higher gate potential (not drain potential) facilitate more rapid device switching. From the materials perspective, one could increase ion concentration, select a bulky counter anion, or design polymer with high ionic conducting ability or with rigid backbone.[26, 169]

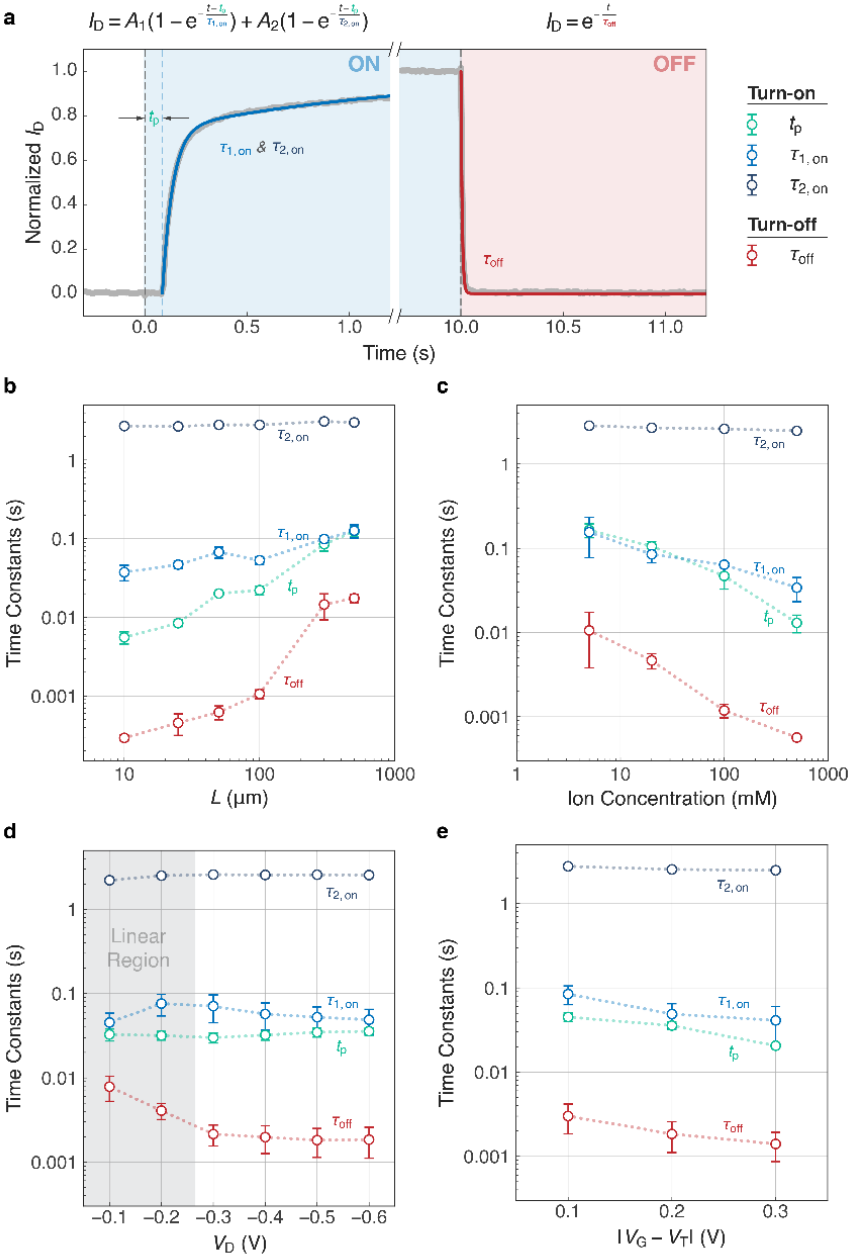

Figure 3.5 Dependency of OECT response times on the operation variablesa, Transient response of a typical accumulation mode PB2T-TEG OECT and the fitting equations. **b**, Relation between time constants and channel length. **c**, Relation between time constants and ion concentration. **d**, Relation between time constants and V_D. **e**, Relation between time constants and $|V_G - V_T|$. Transistor channel width is 2.5 or 5 mm, and the thickness is ≈50 nm for all cases. Electrolyte is 0.1 M KCl and transistor channel length is 100 μm unless otherwise specified. V_D is −0.6 V and $|V_G - V_T|$ is 0.2 V unless otherwise specified. Error bars are standard error of the mean from at least 3 different devices. Dashed lines are guide to the eye.

3.4 CONCLUSIONS

We show that three different conjugated polymers exhibit much faster turn-off compared to turn-on when used to make accumulation mode OECTs. This behavior, while ubiquitous in the literature, is rarely discussed, and is inconsistent with many common OECT models. Using operando optical microscopy, we demonstrate that device turn-on occurs in two temporally and spatially distinct stages: first, a doping front propagates from the source to the drain; second, the partially doped channel continues to dope more homogeneously. In contrast, turn-off occurs in a single step, with the kinetics varying weakly across the channel and the fastest dedoping occurring near the source. We identify several factors contributing to faster device turn-off including channel geometry, differences in doping and dedoping kinetics, and the physical phenomena of carrier density-dependent mobility. In this limit, reducing channel length can be very important to reducing turn-on time due to the initial doping front propagation step, however this might sacrifice the transconductance of OECTs. Second, doping processes are generally slower than dedoping, a factor we hypothesize is due to the rearrangement of the polymer that accompanies the doping process. Nevertheless, the doping front propagation and asymmetry of doping and dedoping rates are still insufficient to explain the large differences in turn-on vs. turn-off times for OECTs. The final key piece which we propose to explain the rapid turn-off is density-dependent mobility. Notably, the functional form of the mobility that we extract using this hypothesis is in excellent agreement with previous reports of the function dependence of carrier mobility on charge density in organic semiconductors. Finally, we show that ion transport is limiting the device speed in that it controls both doping and dedoping kinetics. These observations provide guidelines for engineering faster accumulation mode OECTs from both materials and device perspectives. We believe this unique transient asymmetry renders accumulation mode OECT as a tailorable “slow-

learning, fast-forgetting" unit which may found position in either the toolbox of traditional circuit design or neuromorphic computing applications. We anticipate these results will aid in the selection of counterion chemistries and transistor geometries for specific applications and set that stage for full drift-diffusion models that simulate device behavior of both accumulation and depletion mode OECTs and improve the accuracy of simplified equivalent circuit models.

3.5 MATERIAL AND METHODS

3.5.1 *Polymer film preparation and characterization*

The synthesis of PB2T-TEG[162, 170] (see detailed molecular weight information in the previous paper[50]) and P3MEEMT[167] (M_n = 24 kg/mol, $Đ$ = 1.67) polymers were described in our previous works. P3HT was obtained from Ossila (M109, M_w =36.6 kg/mol). PB2T-TEG polymer was dissolved in chloroform with the concentration of 2 to 4.5 mg/mL. P3MEEMT and P3HT polymers were dissolved in chlorobenzene with the concentration of 20 mg/mL. All polymer solutions were stirred overnight at 50 °C prior to spin coating. The substrates were cleaned sequentially by sonication in acetone and isopropanol for 15 min each. The surface of the substrate was then treated with oxygen plasma for 3 min before spin coating. The spin rate used is 600–2500 rpm to control film thickness between 20 nm to 120 nm. PB2T-TEG polymer films were annealed at 150 °C for 10 minutes under N_2 after spin-coating.

3.5.2 *OECT device fabrication and characterization*

OECT devices comprised lithographically patterned gold on glass substrates (see lithography process below) with transistor widths of 2.5 mm, 5 mm or 6 mm and lengths ranging from 10 μm to 600 μm. Polymers were spun casted onto OECT substrates and were carefully removed except at the electrode junction region via cotton tips (slightly dampened with acetone solution) under

microscope or magnifying lens to ensure minimum impact on the transient response. A secure seal hybridization chamber (GRACE BIO LABS) is attached onto the substrate to confine the electrolyte. A Ag/AgCl pellet is used as the gate. The distance between gate and channel is fixed at approximately 4 mm in this study. The transfer curves were measured using two Keithley 2400 source-measure units controlled by custom Python code. The transient measurements were conducted with NI PXIe-5451, NI PXIe-6366 and NI PXIe-8381 controlled by custom LabVIEW code with time resolution ≈ 10 μs.

The detailed lithography process: NR9-3000PY negative resist (Futurrex, Inc.) was deposited on cleaned glass wafers with diameter equals to 100 mm (University Wafer, Inc.) using Rite Track Automated Coater (SVG-90S), followed by UV light exposure (ABM-SemiAuto-Aligner) and resist development (SVG-90S). Metal deposition (10 nm chromium and 100 nm gold) was accomplished through evaporation (CHA Solution e-beam evaporator). The resist lift-off was achieved by soaking wafers in acetone solution overnight. The wafers were then diced using a Disco Wafer Dicer (Disco, America).

3.5.3 *Operando microscope coupled with OECT characterization*

An iPhone 11 Pro (1080 P, 240 fps) was attached to Leica CME microscope with a 15× eyepiece, a 10× objective (NA = 0.25) and a 650 nm long pass filter (FEL0650, THORLABS) for video recording. Videos were analyzed using custom Python code with OpenCV library. A dark and a reference image were taken for dark and flat field frame corrections, and absorbance calculation. To optimize the video contrast, a thicker PB2T-TEG film was prepared by drop casting from 1 mg/mL chlorobenzene solution to slow down the evaporation rate.

3.5.4 *Spectroelectrochemistry characterization*

The ultraviolet-visible (UV-Vis) absorption spectra were measured using an AVANTES spectrometer (AvaSpec-2048L) coupled with an AVANTES light source (Avalight-HAL-S). Doping and dedoping UV-Vis spectra were collected using continuous mode (with AvaSoft software) with time resolution ≈10 ms/spectrum. The potential bias is controlled using a Metrohm Autolab PGSTAT204 (with NOVA Software version 2.1). Polymers were cast onto fluoride-doped tin oxide-coated glass (FTO, Sigma-Aldrich, 7 Ω/sq) and used as a working electrode. A Ag/AgCl electrode and a Pt mesh were used as reference electrode and counter electrode, respectively. All three electrodes were submerged into a cuvette containing ≈ 2.5 mL of either 0.1 M $KCl_{(aq)}$ or 0.1 M $KTFSI_{(aq)}$.

3.6 ACKNOWLEDGEMENTS

This project is based on research supported primarily by the National Science Foundation, DMR-2003456. K.Y., Z.S., and C.-Z.L. thank the support from National Natural Science Foundation of China (22125901) for supporting synthesis of the PB2T-TEG polymer. J.W.O. and C.K.L.'s contributions to P3MEEMT polymer synthesis are based in part on work supported by the National Science Foundation DMREF-1922259. Part of this work (transistor fabrication) was conducted at the Washington Nanofabrication Facility/Molecular Analysis Facility, a National Nanotechnology Coordinated Infra- structure (NNCI) site at the University of Washington with partial support from the National Science Foundation via awards NNCI-1542101 and NNCI-2025489.

Chapter 4. UNDERSTANDING THE MECHANISM OF DEGRADATION IN ORGANIC ELECTROCHEMICAL TRANSISTORS

4.1 INTRODUCTION

Organic mixed ionic–electronic conductors (OMIECs) have emerged as promising devices with diverse applications in organic electronics,[171] bioelectronics,[172], energy storage,[56] and neuromorphic computing[128]. In OMIECs implemented as the channel of organic electrochemical transistors (OECTs), this ionic-electronic coupling enables the modulation of electrical conductivity as low-voltage, high-transconductance devices that can both sense and amplify biological signals. Compared to the traditional organic field effect transistors (OFETs), OECTs harness the unique property of volumetric capacitance, which contributes to their high transconductance, enabling efficient modulation of electronic conductivity. However, the presence of a bulky ion-electron coupling mechanism in OECTs can present challenges, particularly in terms of switching time and device stability. The sluggish kinetics associated with ion diffusion and the intricacies of ion-electron interactions can lead to prolonged switching times, limiting the device's response speed. Furthermore, the continuous exchange of ions during operation can induce structural changes and material degradation, ultimately affecting the device's long-term stability. Addressing these issues is crucial for advancing the performance and reliability of OECTs, opening new avenues for their application in cutting-edge electronic technologies.

Previous studies to improve the OMIEC stability have focused on the polymer side-chain design,[21, 29] cosolvents and additives influence,[173] substrate engineering,[174, 175] ion species,[176] and oxygen reduction reaction (ORR) in ambient environment.[177] In this chapter, we delve into the complexities of OECT stability with an example polymer, poly(3-

methoxyethoxyethoxybutylthiophene) P3MEEBT, investigating the underlying mechanisms that drive performance degradation during cycling operations and proposing strategies to mitigate these effects. To gain a more comprehensive understanding of OMIEC stability, we adopt the operando microscopy coupled with hyperspectral imaging. We aim to unveil the underlying factors that influence OECT stability, providing deeper insights into the intricate processes affecting the device's long-term performance and reliability. Through this comprehensive investigation, we aspire to shed light on the complex interplay between OMIEC electrochemical stability and OECT device behavior, ultimately leading to improved device design and performance optimization for practical applications.

4.2 RESULTS AND DISCUSSION

Previous efforts to investigate the electrochemical stability of OMIECs have mainly centered around studying the redox stability of OMIEC-coated electrodes and correlating these findings with the performance and degradation of OECTs.[29, 146, 178] However, as demonstrated in Chapter 3, it has become evident that the thin film behavior might not necessarily represent the true performance of OECT devices. **Figure 4.1 a.b** show the schematic setup of spectroelectrochemistry and OECT measurements. The polymer P3MEEBT stability has been evaluated through repetitive pulsing (0V/-0.4V vs. Ag/AgCl). To probe the doping level during spectroelectrochemistry cycling, we extracted the absorption at the π-π* transition peak (~ 550 nm) over time. When electrochemically doped, P3MEEBT exhibits a decreasing absorption at the π-π* transition peak and an increasing wide peak around 750 nm (polaron) and >1500 nm (bipolaron). After 20 cycles, the π-π* absorption bleaching degree maintained with no significant decay. (**Figure 4.1 c**) Similarly, we also track the drain current (I_D) over cycling. (**Figure 4.1 d**) In contrast to spectroelectrochemistry, the performance of OECTs shows a clear and noticeable

decay over repeated cycling. After just 20 cycles, the peak drain current of OECT devices decreases to approximately 25% of its initial value. Indeed, the observed difference in performance between spectroelectrochemistry and OECTs highlights the unique stability challenges associated with the transistor terminal geometry. The transistor terminal geometry of OECTs introduces complexities in charge transport and ion-electron coupling. Thus, we need to decouple the influence from ionic injection and electronic mobility. To compare the charging process, we extracted the maximum injected charge amounts by integrating the doping current for both spectroelectrochemistry and OECT over each cycle. (**Figure 4.1 e, f**) In spectroelectrochemistry setup, it is not surprising that the charges show no change, as they agree with the stable absorption bleaching. On the other hand, in the OECT setup, there is a slight decay in the amount of charges over repeated cycling. Despite this initial decay, after 20 cycles, the charges maintain approximately 75% of their initial amount. This finding suggests that while the OECT's peak drain current experienced a more significant decay, the overall amount of charges involved in the electrochemical processes remains relatively stable. This observation indicates that factors other than charge amount may contribute to the degradation in OECT performance. The discrepancy between the charge decay and the device degradation suggests the intricate interplay of various factors affecting OECT stability, such as charge mobility, electrode surface.

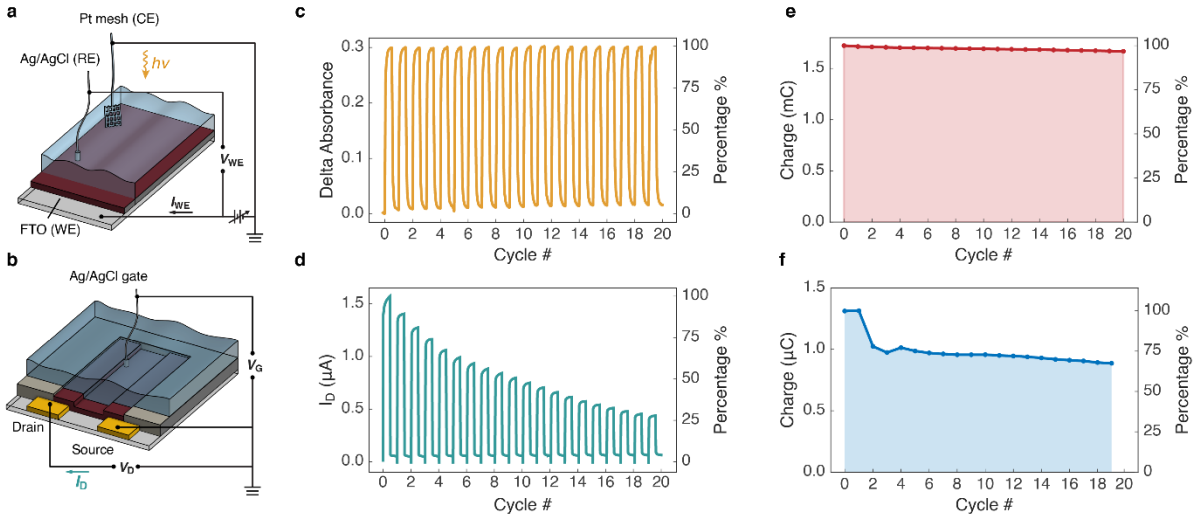

Figure 4.1 Stability comparison between OECT and UV-Vis spectroelectrochemistry. a,b, Schematic diagram of spectroelectrochemistry (SpecEChem) (a) and OECT (b) experimental setups. c,d, An example cycling stability test of spectroelectrochemistry (c) at polaron peak absorption wavelength (550 nm) and OECT (d) at saturation region (V_D = −0.4 V) in 100 mM KTFSI. e,f, The integral charge amount injected during electrochemical doping process with SpecEchem (e) and OECT (f) setup.

To discern whether degradation occurs at the electrode surface or across the channel polymer, a novel OECT channel design was implemented, featuring two internal probe electrodes. This innovative configuration allows for localized measurements at different points along the channel, providing valuable insights into the degradation mechanism. We first cycled the entire OECT channel (i.e., E_1 as drain, E_4 as source) over 100 cycles until the channel became completely died. (**Figure 4.2 a,b**) After the cycling, we then test the transfer performance of three internal channel: near drain end (E_1-E_2), middle channel (E_2-E_3), and near source end (E_3-E_4). If the degradation primarily occurs at the electrode surface, one would expect to observe a more significant decay in current at the electrode-probe junctions, but not the middle channel. However, **Figure 4.2 c-f** show gradient of degradation across the channel, with the worst degradation observed near the source end and a less pronounced degradation near the drain end. This result suggests that the polymer-

electrode interface may not be the primary contribution to the observed degradation. Interestingly, even the entire channel has been died, the near-drain-end channel (E_1-E_2) still performs like a normal OECT. Therefore, we believe the degradation of OECT starts from the source end, and when the degradation becomes severe and the bad region extends far away from the source, the entire channel disconnect and block the electronic transport, leading to a dead device. The observed degradation pattern points to the possibility that degradation mechanisms might be more complex and multifaceted.

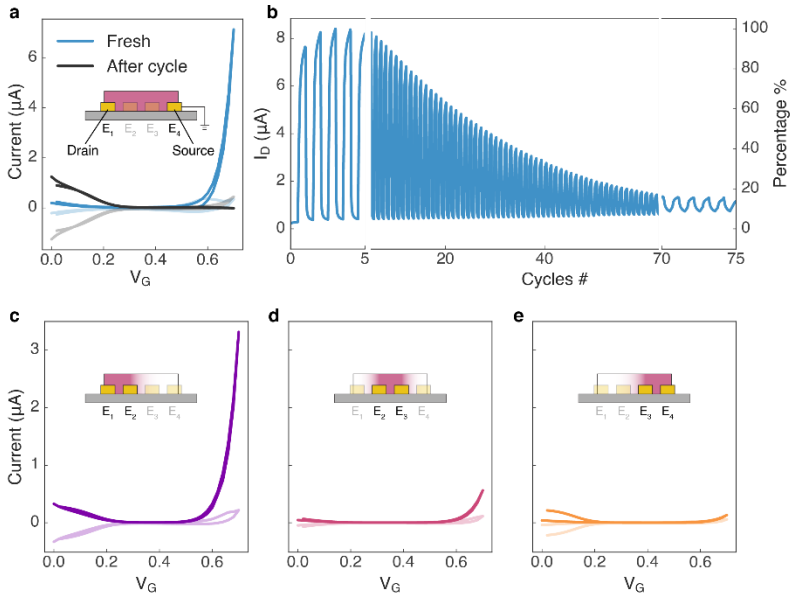

Figure 4.2 Internal degradation gradient across the channel. a, The transfer curve of the OECT channel before (blue) and after (black) 100 cycles. b, OECT cycling test. c,d,e, The transfer curves after cycling test with different channel region from near drain end (c), middle channel (d) and near source end (f). Insert: Schematic of device structure for selected probe electrodes ($E_{1\text{-}4}$).

Previous studies on OMIECs electrochemical process have shown structural change[25, 102] and mass uptake[26, 29]. To probe the structural change, we carried out grazing-incidence wide-angle X-ray scattering (GIWAXS) on pre-cycled OECT channel. Due to the spatial limit from the beam size, we design a "pseudo-OECT" structure with a mm-scale channel length. (**Figure 4.3 a**) **Figure 4.3 b** shows the out-of-plane (OOP) linecut at each position. It is clear that across the entire

channel, the face-on lamellar (d00) patterns have no significant changes even after 60 cycles. Thus, the gradient degradation does not come from the structural damage over the OECT channel.

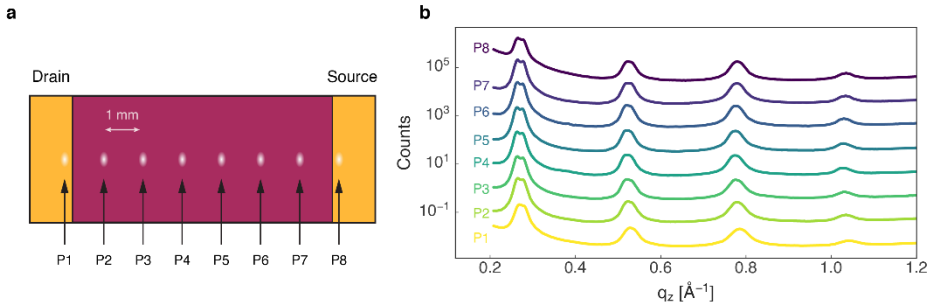

Figure 4.3 GIWAXS on a pseudo-OECT. a, Schematic diagram of pseudo-OECT GIWAXS setup. b, The out-of-plane (OOP) linecut at each position.

Furthermore, we carried out the operando microscopy setup mentioned in Chapter 3 coupled with the hyperspectral microscopy, which records the full spectrum over a wide range of wavelengths. (**Figure 4.4 a**) With the power of hyperspectral microscopy, we could capture the absorption at single wavelength, which gives us more accurate details and higher wavelength resolution. **Figure 4.4 b** shows the absorption profile at π-π* transition peak across the OECT channel. According to the ON states, the π-π* absorption bleaching shows minimal changes over 10 cycles. However, the device drain current decayed to 50% of the initial level. This result suggests that the degradation of the OECT drain current is not due to the difference in the charge density, but the charge mobility. Given that no damage was observed in the polymer lamellar structure, a plausible hypothesis is that the decrease in mobility is attributable to the intercrystallite features. Interactions and arrangements between polymer crystalline domains, particularly at the interfaces between them, can significantly impact charge transport properties within the channel. By investigating the inter-crystalline features and their influence on charge and ion transport, researchers can gain crucial insights into the underlying mechanisms driving the observed decrease in mobility and overall device degradation. Understanding these aspects will be essential for

devising targeted strategies to enhance the stability and performance of OECTs and other OMIEC-based devices in organic electronics applications. It will also inform the development of novel materials and processing techniques aimed at optimizing the inter-crystalline structure, ultimately contributing to the advancement of organic electronics technology.

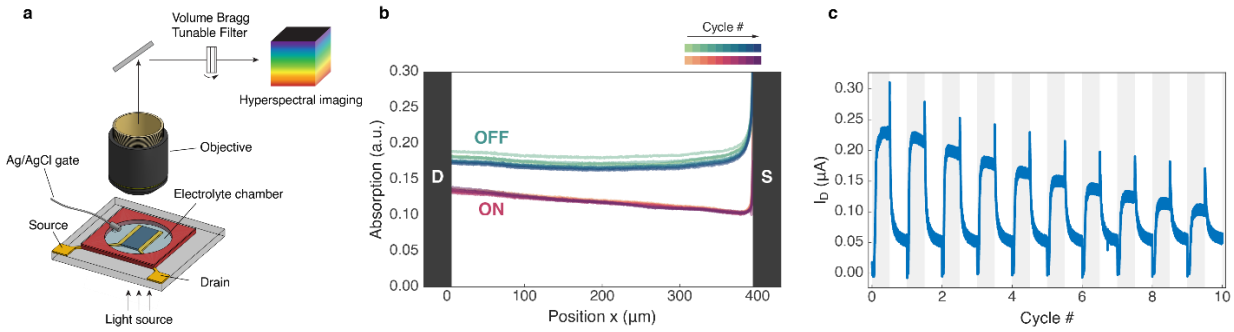

Figure 4.4 Operando hyperspectral microscopy over the OECT cycling. a, Schematic operando hyperspectral microscopy setup. b, The absorption at π-π* transition peak (525 nm) across the OECT channel and over 10 cycles at steady states. c, The OECT cycling stability performance.

4.3 CONCLUSIONS

We have provided comprehensive insights into the electrochemical stability of OMIECs and its impact on the performance of OECTs. Previous efforts to investigate OMIEC stability have primarily focused on studying redox stability and thin film behavior. However, it became evident that thin film behavior might not fully represent OECT performance, leading us to explore the degradation mechanism further. Through spectroelectrochemistry and OECT measurements, we observed a clear difference in performance, with OECTs showing significant decay in peak drain current over repeated cycling. However, the amount of charges involved in the electrochemical processes remained relatively stable. This discrepancy suggested that factors other than charge amount, such as charge mobility and electrode surface, contribute to OECT degradation.

To investigate the contribution of the polymer-electrode interface, a novel OECT channel design with internal probe electrodes was implemented. Surprisingly, the degradation showed a gradient across the channel, with the worst degradation near the source end and less pronounced degradation near the drain end. This observation suggested that the polymer-electrode interface might not be the primary contributor to degradation. Structural analysis using GIWAXS showed no significant changes in the face-on lamellar patterns across the OECT channel after repeated cycling, ruling out structural damage as a cause of degradation. The operando microscopy setup coupled with hyperspectral microscopy provided more accurate details and higher wavelength resolution, revealing that the degradation of OECT drain current is likely due to charge mobility changes. Despite no damage in the polymer lamellar structure, a plausible hypothesis is that the decrease in mobility is attributable to the influence of inter-crystalline features.

Overall, this chapter has shed light on the complex interplay of factors affecting OECT stability and performance. By understanding the underlying mechanisms, targeted strategies can be developed to enhance OECT stability and reliability. The findings presented in this work contribute to the advancement of organic electronics and the optimization of OECTs for practical applications in various emerging technologies. The novel approaches and insights gained from these studies open new avenues for future research in the field of OMIECs

4.4 MATERIALS AND METHODS

4.4.1 *Polymer Synthesis and characterizations*

All reactions were performed under air-free conditions using standard Schlenk techniques. All reaction glassware was dried overnight in an oven at 120 °C prior to use. Following monomer synthesis, P3MEEBT and P3MTEEBT were synthesized using Kumada Catalyst Transfer Polymerization (KCTP). The produced polymer was characterized via size-exclusion

chromatography (SEC), using a Malvern Viscotek TDA 305 GPC equipped with UV and refractive index detectors. THF was used as an eluent at a temperature of 40 °C and a flow rate of 1 mL/min. Molecular weight information was determined relative to polystyrene standards. 1H NMR was performed using either a 300 MHz Bruker AV-300 or a 500 MHz Bruker AV-500 instrument at 25°C.

4.4.2 *Spectroelectrochemistry characterization*

The ultraviolet-visible-near IR (UV-Vis-NIR) absorption spectra were measured using an AVANTES spectrometer (AvaSpec-2048L) coupled with an AVANTES light source (Avalight-HAL-S). The potential bias is controlled using a Metrohm Autolab PGSTAT204 (with NOVA Software version 2.1). Polymers were cast onto fluoride-doped tin oxide-coated glass (FTO, Sigma-Aldrich, 7 Ω/sq) and were used as a working electrode. A Ag/AgCl electrode and a Pt mesh was used as reference electrode and counter electrode, respectively. All three electrodes were submerged into a cuvette containing ≈2.5 mL of 0.1M KTFSI (aq). The cycling test was carried out over 30 cycles, including 10 s ON, 10 s OFF in each cycle.

4.4.3 *OECT device fabrication and characterization*

OECT devices comprised lithographically patterned gold on glass substrates (see lithography process below) with transistor lengths of 10 μm and widths ranging from 100 μm to 4000 μm. Transfer curves were measured by varying V_G from 0 V to -0.7 V and then back to 0 V (vs. Ag/AgCl). The V_D was fixed at -0.6 V. Cycling stability tests were taken under repetitive pulses (0 V 30 s, -0.4 V 30 s for each cycle) over 20 cycles.

4.4.4 *Grazing incidence wide-angle scattering (GIWAXS)*

GIWAXS measurements were performed on Beamline 7.3.3 at the Advanced Light Source (ALS) at Lawrence Berkeley National Laboratory using a Pilatus 2M area detector.[110] The images were taken with a beam energy of 10 keV and an incidence angle of 0.14° with 10 s exposure times. Pre-cycled samples were prepared in 100 mmol/L KTFSI after 60 cycles on/off switching (0 V/–0.6 V for 30 s each cycle) with an Ag/AgCl counter electrode. All films were dried for 30 min in a helium atmosphere.

Data were processed using Nika and WAXStools in Igor Pro.[111] Peak positions and peak full width at half maximum (FWHM) were determined by fitting to Lorentzian peaks.

4.4.5 *Hyperspectral microscope*

Hyperspectral measurements were performed using a Photon etc. IMA upright microscope fitted with a transmitted darkfield condenser and a 40X objective (Nikon Plan RT, NA 0.7, CC 0-1.2). The Hyperspectral Microscope uses a tunable Bragg filter to image a sample at specific wavelengths.

The sample is imaged throughout the spectral range and these images are combined into a single “Hyper Cube”, which carries spectral information at each pixel. This allows for diffraction limited imaging, rather than being constrained by the spot size of the fiber optic cable. Post-processing was done in the proprietary Photon etc. PHySpec Software and custom Python code.

Chapter 5. CONCLUSIONS AND FUTURE DIRECTION

In conclusion, this dissertation has delved into the realm of mixed ionic-electronic transport in conjugated polymers, shedding light on its intricate mechanisms and unveiling its significance for organic electronics. Through a series of operando measurements and comprehensive studies, we have explored the molecular-level structural changes, operational characteristics, and stability challenges associated with these materials.

The first study unveiled the diverse world of molecular design for OMIECs, emphasizing the critical roles of backbone engineering and sidechain modulation. This exploration illuminated strategies for achieving optimal electronic and ionic transport properties, paving the way for tailored material design in the pursuit of enhanced device performance.

In the second study, we ventured into the realm of organic electrochemical transistors (OECTs), dissecting their functionality, transconductance, and switching speed. Our findings not only elucidated the operational limits of OECTs but also pointed towards innovative engineering avenues for optimizing their response and performance.

The third study tackled the pressing issue of OECT stability, unraveling the intricate interplay of factors that contribute to device degradation. Through a meticulous exploration of degradation patterns and charge mobility, we discerned the primary source of instability, paving the way for targeted strategies to enhance the stability and lifespan of OECTs.

As we move forward, these insights beckon towards exciting future directions. The realm of OMIECs and OECTs holds immense potential for applications spanning neuromorphic computing, bioelectronics, and beyond. The understanding gained from this research lays the foundation for novel materials, advanced device architectures, and sophisticated engineering approaches that will propel organic electronics into new frontiers.

In the pursuit of these prospects, future research endeavors could encompass multi-scale simulations to elucidate intricate transport phenomena, innovative hybrid materials for improved performance and stability, and collaborations across disciplines to address complex challenges. Ultimately, the journey of unraveling mixed ionic-electronic transport is far from over, and this dissertation serves as a stepping stone towards a vibrant future where organic electronics reshape the technological landscape.

As we close this chapter, we stand at the crossroads of discovery, armed with the knowledge and insights gained from these studies. The road ahead beckons with promise and potential, and I am excited to witness the continued evolution of this captivating field.

Appendix A. SUPPLEMENTARY INFORMATION FOR CHAPTER 2

Appendix A accompanies Chapter 2: Hydration of a side-chain-free n-type semiconducting ladder polymer driven by electrochemical doping.

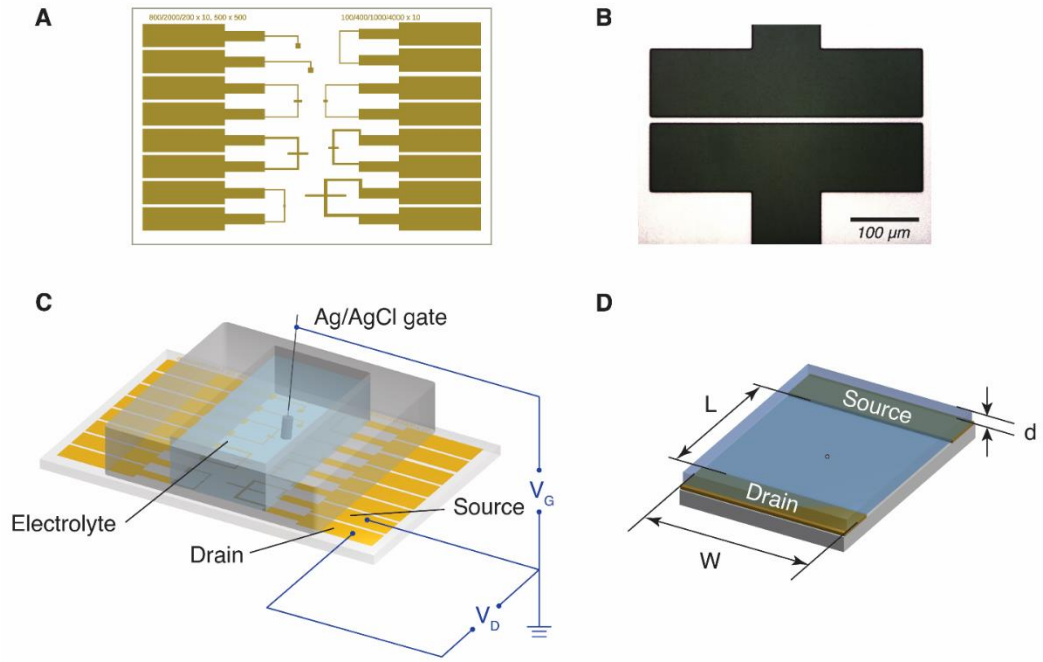

Figure A.1 OECT device measurement setup and dimensions. A) Configuration of the custom OECT substrate with 7 pixels (Length: 10 µm. Width: (100, 200, 400, 800, 1000, 2000, 4000) µm). B) Light microscope image of a W×L = 400 µm×10 µm channel. C) Schematic drawings of OECT device measurement setup. D) OECT configuration and channel dimensions (*W*, *L*, and *d*) of one channel.

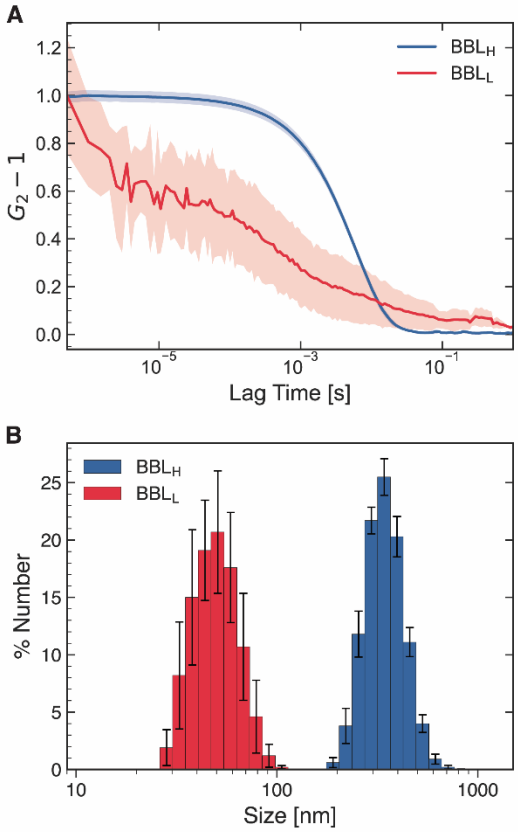

Figure A.2 Molecular weight estimation via DLS. A) Autocorrelation functions (ACFs) of **BBL$_L$** and **BBL$_H$** recorded during DLS measurements. B) Distribution of the hydrodynamic size of **BBL$_L$** (M_v = 6.15 kDa) and **BBL$_H$** (M_v = 60.5 kDa). The error bars represent one standard deviation over 10 readings.

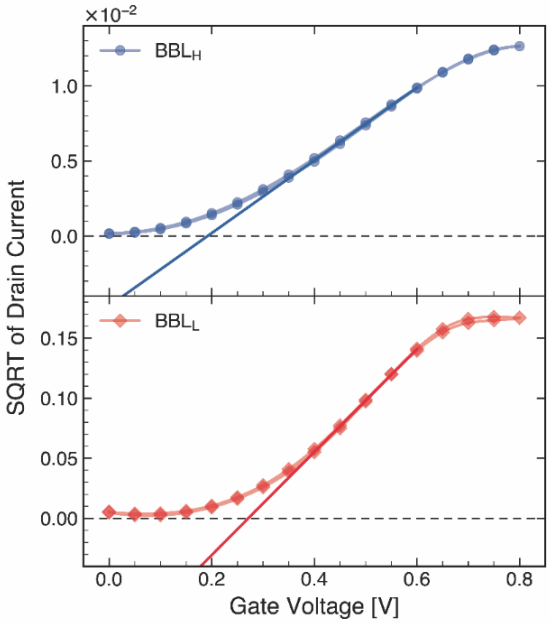

Figure A.3 Determining the threshold voltage of OECTs. The threshold voltage is determined x-axis intercept of the tangent drawn to the linear part of the square root of the I_D vs. V_G. The threshold of **BBL$_H$** (0.17 V) is much lower than the one of **BBL$_L$** (0.28 V), which suggests that the **BBL$_H$** OECT is easier to turn ON in 100 mmol/L KCl.

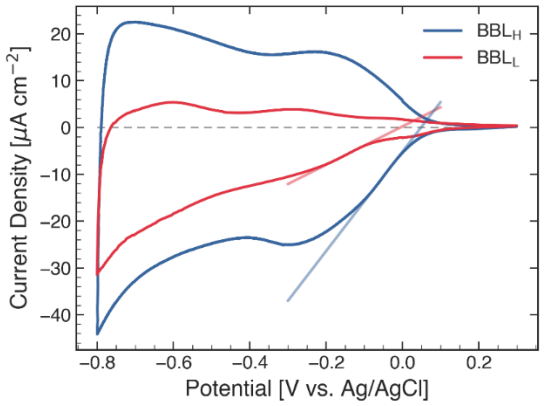

Figure A.4 Cyclic voltammetry curves of two BBLs in 100 mmol/L KCl. The onset voltage of the **BBL$_H$** (0.05 V) is less negative than the **BBL$_L$** (–0.01 V), which agrees with the threshold voltage shift in the OECTs.

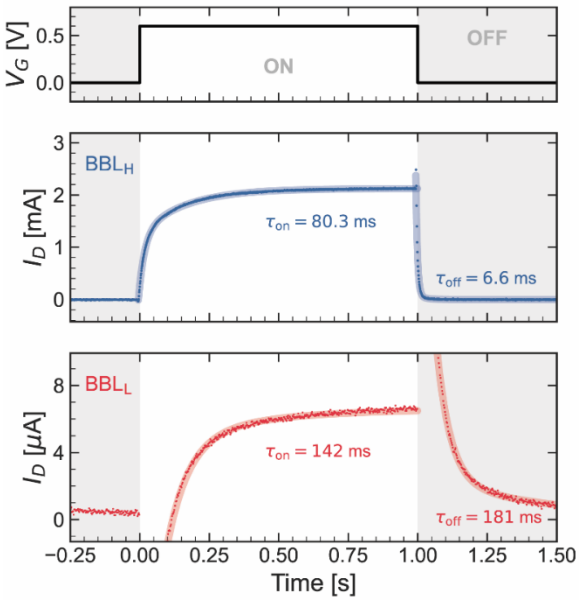

Figure A.5 Typical OECTs transient behavior in 100 mmol/L KCl. The normalized drain current is fit to biexponential equation $I_D = A_1\left(1 - e^{-t/\tau_1}\right) + A_2\left(1 - e^{-t/\tau_2}\right)$. Device dimension: W×L = 4000 μm×10 μm.

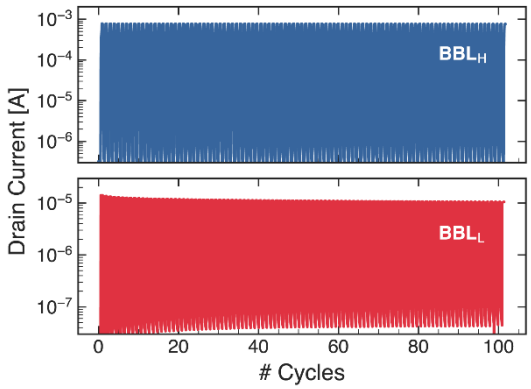

Figure A.6. OECT stability of BBL$_H$ (top, blue) and BBL$_L$ (bottom, red) OECT devices over 100 cycles in 100 mmol/L KCl. (V_G = 0 V/+0.6 V, V_D = +0.6 V, W×L = 800 μm×10 μm)

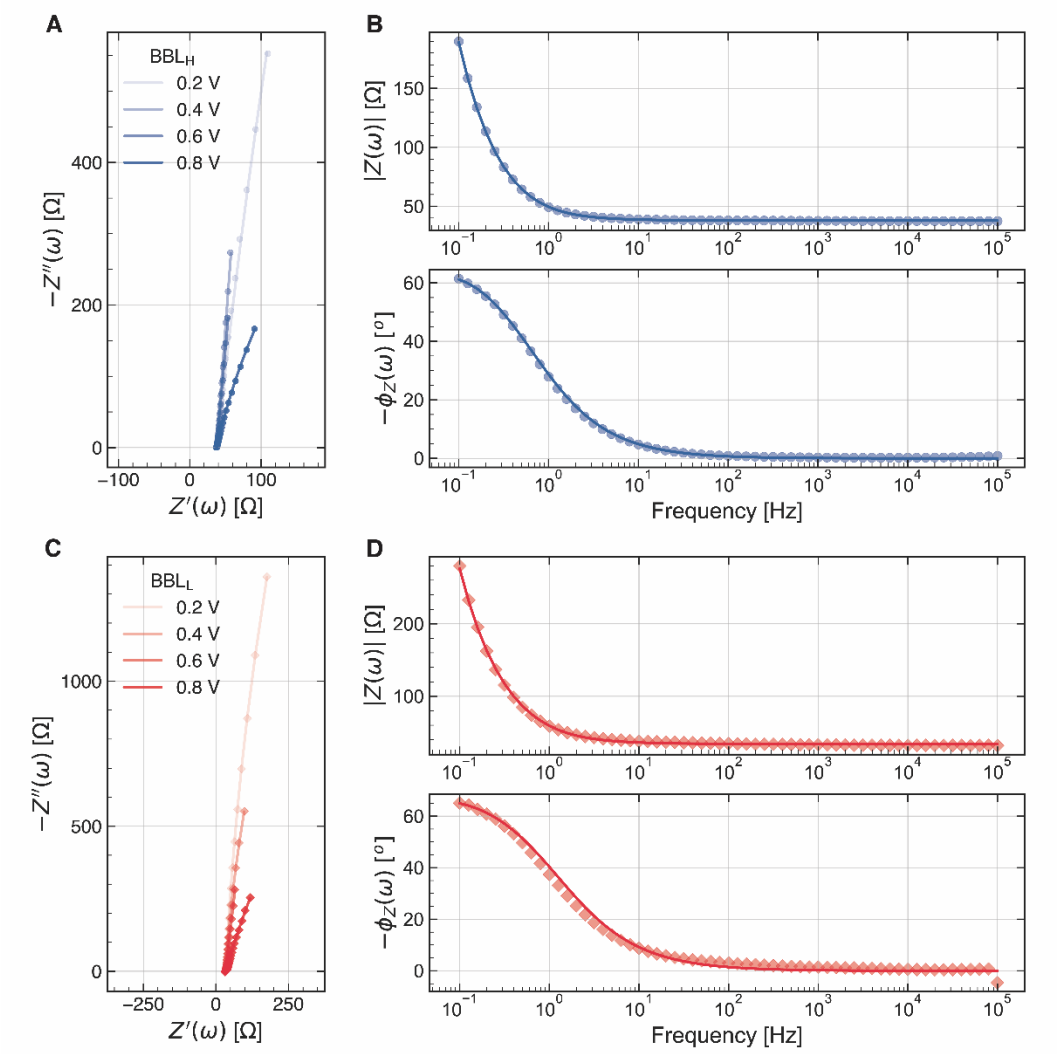

Figure A.7 Impedance spectra from EIS measurements. Example Nyquist (A, C) and Bode plots (B, D) of **BBL$_H$** (top) and **BBL$_L$** (bottom) in 100 mmol/L KCl. For the Nyquist plots, the gate voltages were converted from the electrochemical cell potentials. For the Bode plots, the films were doped at V_G = 0.8 V. The electrode area is 1×1 cm^2. Thickness is ≈ 120 nm.

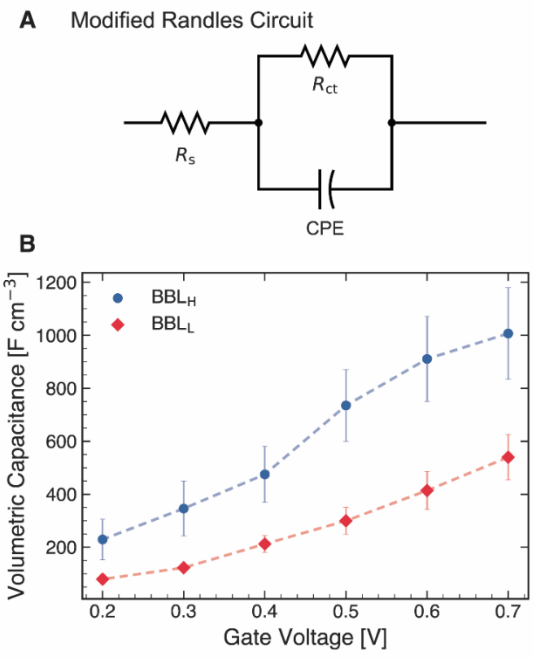

Figure A.8 Extracted volumetric capacitance over different potentials of two BBLs. A) The equivalent circuit for electrochemical impedance spectroscopy. B) Average volumetric capacitance as a function of gate voltages for two BBLs. The error bars represent the standard deviation of the mean.

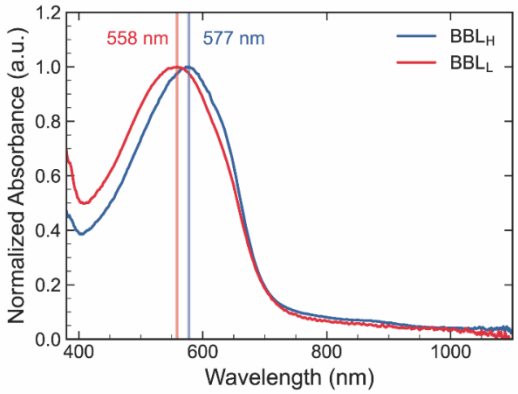

Figure A.9 Normalized UV–Vis absorption spectra of BBL_L and BBL_H films. The **BBL_H** shows a red shift in the peak absorption, which suggests that the **BBL_H** has a longer conjugated length.

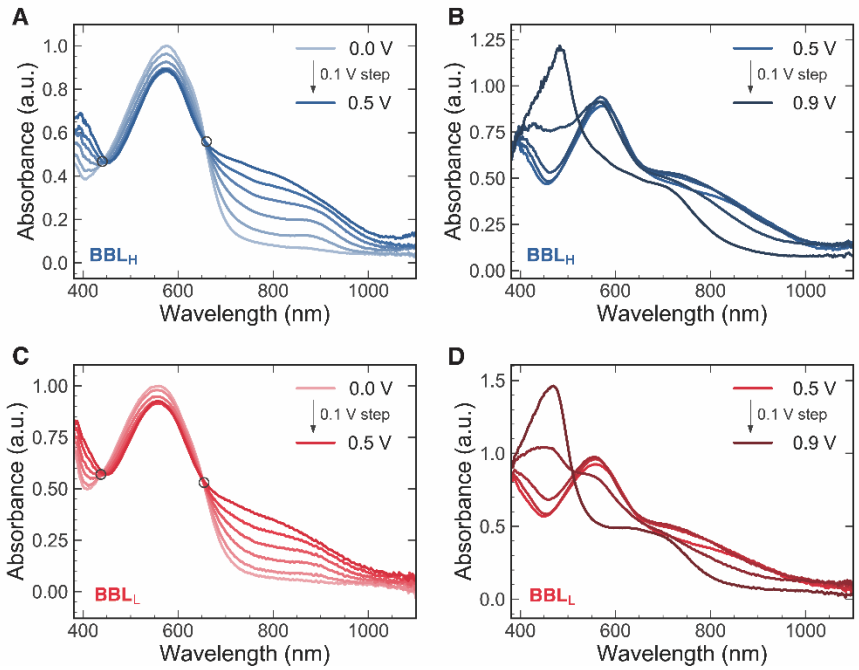

Figure A.10 Raw UV-Vis absorption spectra under different potentials of **BBL$_H$** (A, B) and **BBL$_L$** (C, D). The UV-Vis absorption spectra show two voltage ranges with different signature features. At low voltages (left, 0 V to 0.5 V), two isosbestic points are visible at about 450 nm and 650 nm, suggesting the reaction from neutral BBL to single charged BBL.[23, 50] At high voltage (right, above 0.5 V), the spectra changes become complex. The signature feature is the absorption increase around 450 nm, which corresponds to the conversion from single charged BBL to multiply charged form.[50]

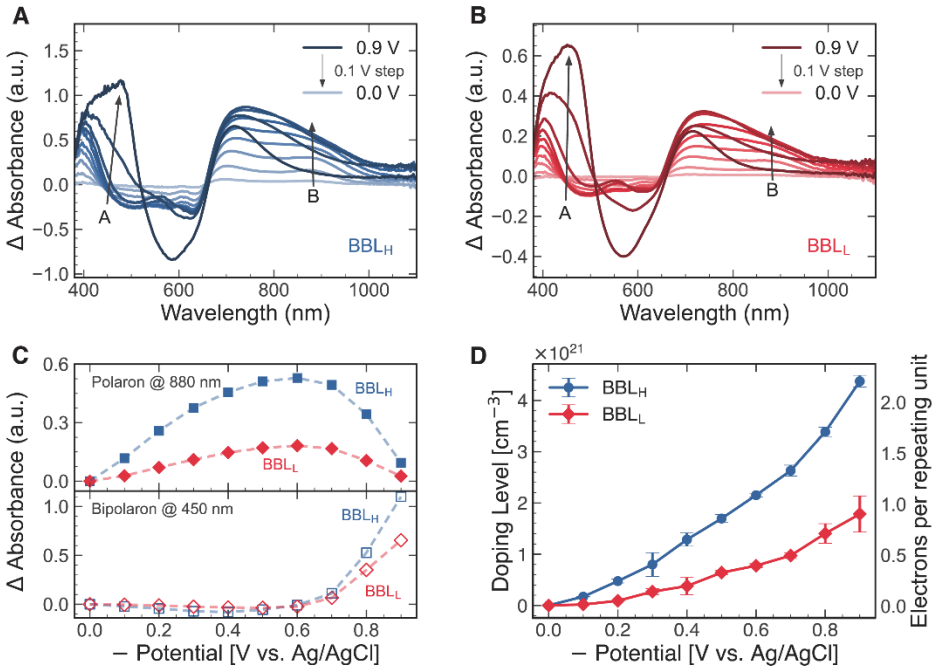

Figure A.11 The differential UV–Vis absorption spectra under different potentials of A) **BBL$_H$** and B) **BBL$_L$** at a steady state in 100 mmol/L KCl. (Polaron: peak B, Bipolaron: peak A.) C) The differential UV–Vis absorption spectra at select wavelengths under different potentials in 100 mmol/L KCl. D) The doping levels in two types of BBLs under different potentials were calculated by integrating the dedoping current at certain applied potential after taking the UV–Vis spectra. The charge integral from dedoping current, not doping current, was intentionally chosen to avoid the impact of ORR. (Detailed discussions in Appendix A.2) The electrons per repeat unit (ERU) were calculated by assuming the film density is 1.1 g/cm^{3,} and the monomer unit of BBL is 334 g/mol. The baseline was the spectrum taken at –0.3 V to dedope the film prior to the doping steps. The error bars represent the standard error of the mean over 3 measurements.

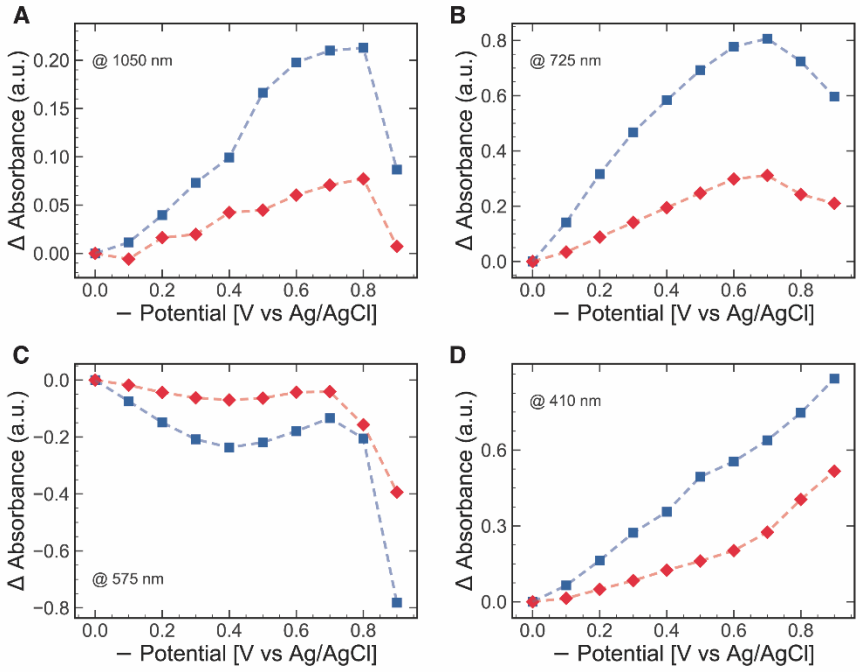

Figure A.12 Differential UV-Vis spectra intensity at selected wavelengths measured in 100 mmol/L KCl. The baseline spectrum was taken at –0.3 V to dedope the film.

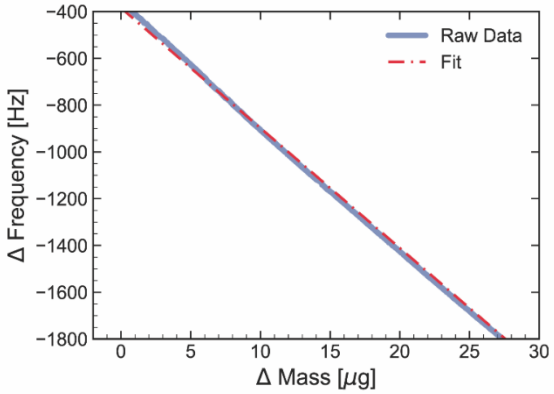

Figure A.13 Calibration of QCM sensitivity factor. Change in frequency (blue) in response to the change of mass due to electrochemical deposition of silver from $AgNO_3/HNO_3$ solution at 400 µA constant current and the fit (red) used to extract the sensitivity factor.

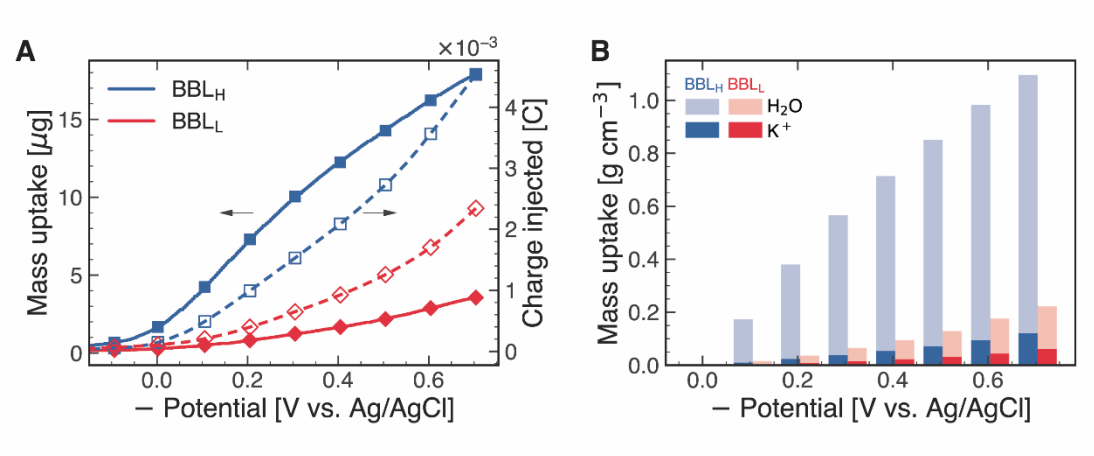

Figure A.14 The mass uptake and charge injection measured via eQCM. A) The mass uptake (left, solid) and charge injection (right, dashed) as a function of doping potentials in both BBLs. B) Calculated K^+ cations (dark color) and water molecules mass (light color) injected into the as a function of doping potentials. The charge integral from dedoping current, not doping current, was intentionally chosen to avoid the impact of ORR. (Detailed discussions in Appendix A.2)

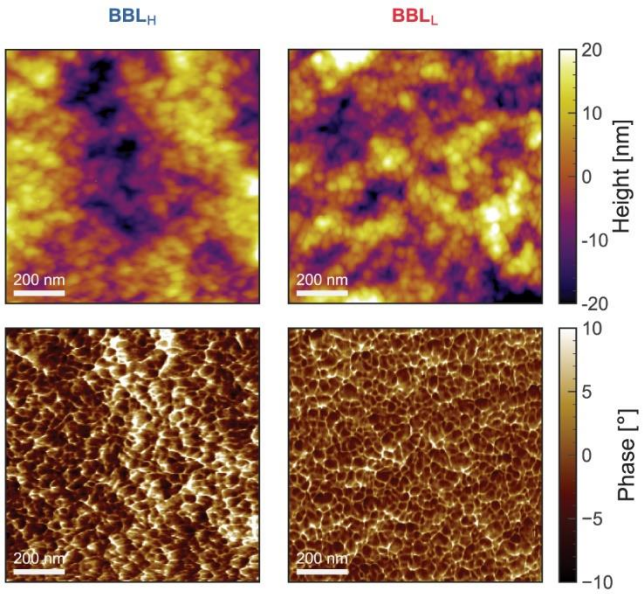

Figure A.15 Atomic force microscope (AFM) topography and phase images of the BBL_H (left) and BBL_L (right).

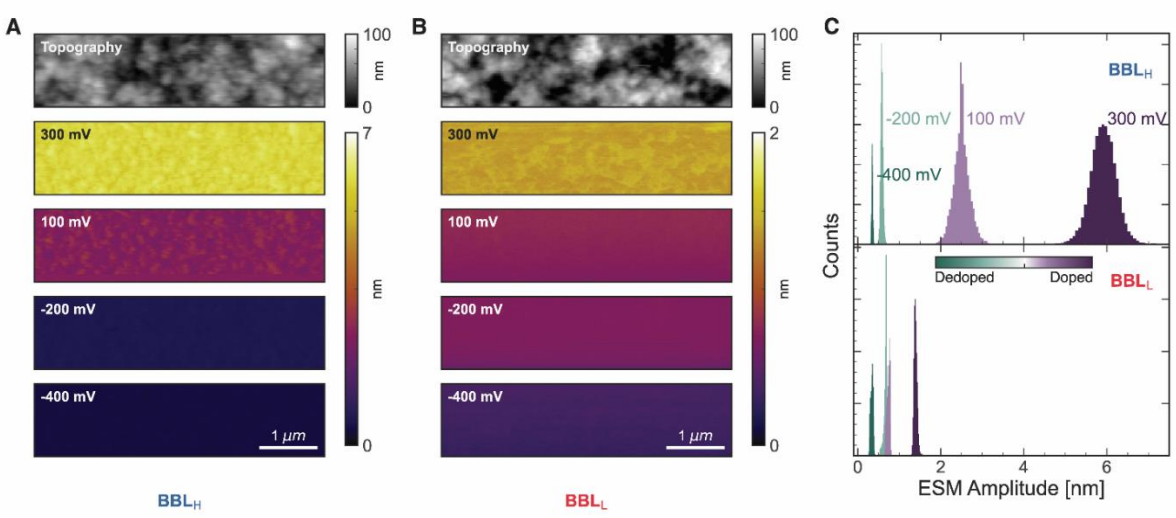

Figure A.16 Topography, ESM amplitude images and ESM amplitude histogram. Topography and ESM amplitude images of the **BBL$_H$** (A) and **BBL$_L$** (B) films in 100 mmol/L KCl at a 500 mV AC drive voltage. ESM images were taken with the tip at different DC potentials (as labeled). C) The histogram of ESM amplitude of two BBLs under different tip bias.

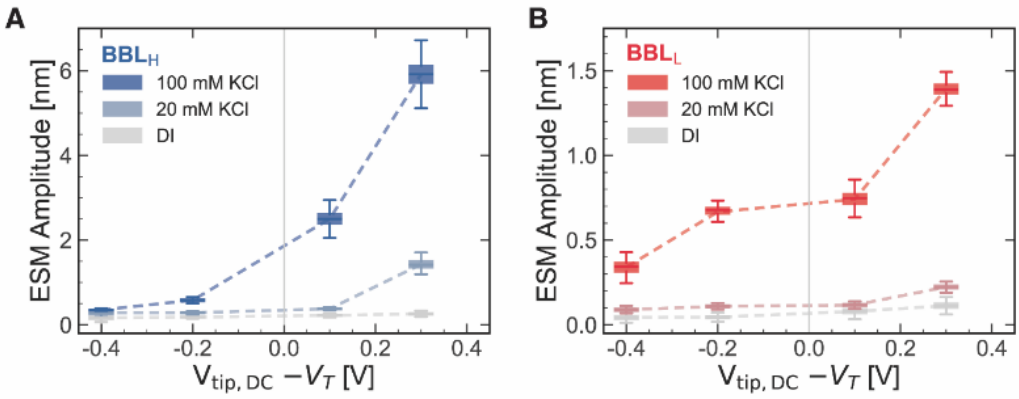

Figure A.17 ESM amplitude of two BBLs under different electrolyte concentrations. ESM amplitude of the **BBL$_H$** (A) and **BBL$_L$** (B) films in the KCl electrolyte with different concentrations. The error bars represent one standard deviation of the ESM amplitude.

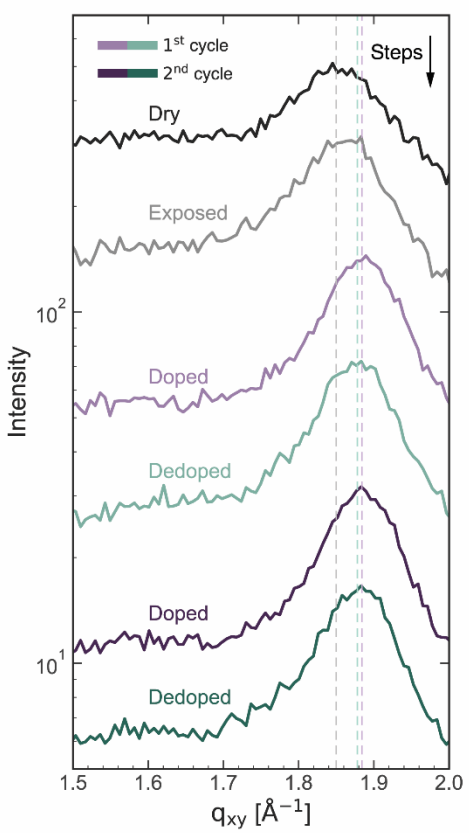

Figure A.18 In plane (IP) linecut profiles of *in operando* GIWAXS patterns of BBL_H thin films under different film conditions. The dashed lines are used to guide the eye.

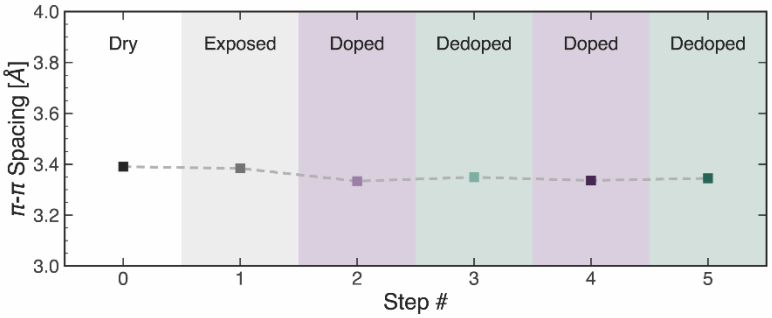

Figure A.19 The (010) π–π spacing changes along the *in operando* GIWAXS doping/dedoping cycle steps. Purple traces/markers: doped states; Green traces/markers: dedoped states.

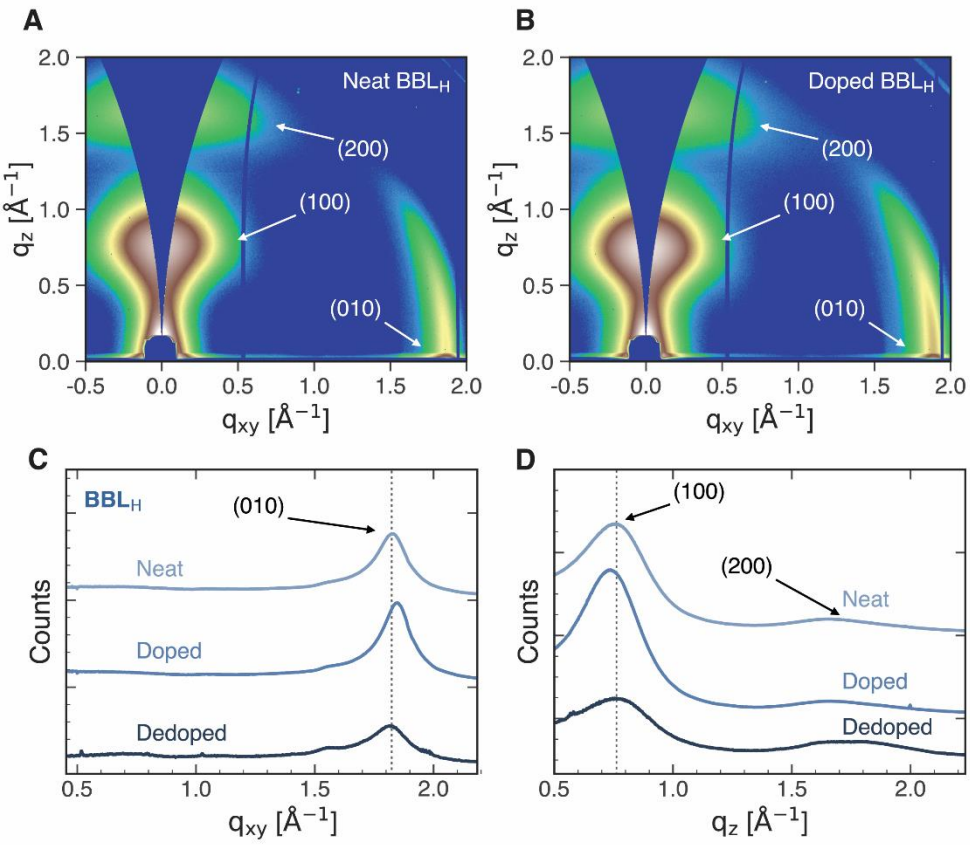

Figure A.20 2D GIWAXS images of BBL$_H$ neat (A) and doped (B) films. The in plane linecuts (C) and out of plane linecut (D) of different doping states.

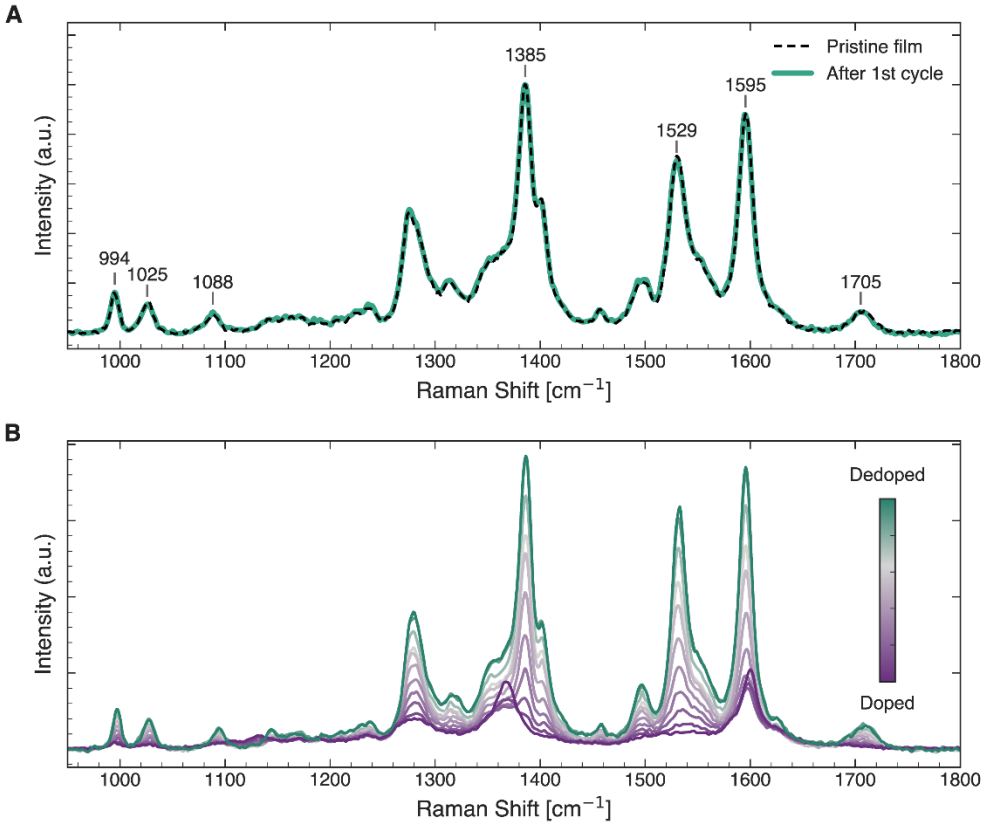

Figure A.21 Raman spectra on BBL_H samples. A) The Raman spectra with 532 nm excitation of dry BBL_H films before (dashed) and after (solid) the first doping/dedoping cycle. No significant change in peak intensity and no new peak formation was found, which indicates that there is no chemical reaction between the BBL_H backbone and the remaining waters. The peak positions assigned to various vibration modes are summarized in **Table A.1**. B) *Operando* Raman spectra of BBL_H during the first doping/dedoping cycle in 100 mmol KCl solution. Potential was swept from −0.7 V (doped, purple) to +0.3 V (dedoped, green), 0.1 V step.

Table A.1 Raman peak assignment of the Raman spectra of BBL[50, 179]

Raman peaks (cm^{-1})	Peak assignment
994, 1025	Naphthalene and imidazole ring breathing
1088	C-H bending
1385	C-N stretching
1529	Aromatic C-C and C-N skeletal vibrations
1595	C=N imine carbon-nitrogen stretching
1705	C=O stretching

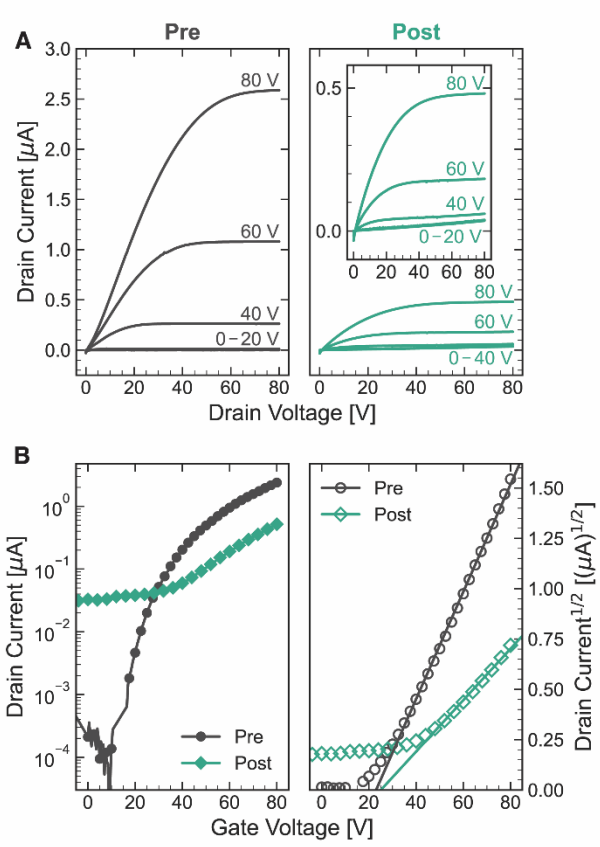

Figure A.22 BBL_H OFET performance before and after the first doping/dedoping cycle. Output curves (A) and transfer curves (B) of the same BBL_H OFET device before the 1st hydration cycle (black) and after the 1st hydration cycle (green). The post-cycle OFET shows a similar threshold voltage, but a lower drain current and ON/OFF ratio. The post-cycle OFET mobility ($(2.3 \pm 0.4) \times 10^{-3}$ cm^2 V^{-1} s^{-1}) is about an order of magnitude lower than the pre-cycle mobility ($(13.8 \pm 0.7) \times 10^{-3}$ cm^2 V^{-1} s^{-1}), which results from the remaining waters. Error bars present the standard error of mean over 4 device pixels.

A.1 Discussion on molecular weight effect on OECT performance

We observed that **BBL$_H$** shows a higher electronic mobility μ, as well as a higher volumetric capacitance C^* than **BBL$_L$**. (**Table 2.1**) To understand the origin of the enhancement, we further investigate the crystal structure differences between two BBLs with grazing-incidence wide-angle X-ray scattering (GIWAXS). (**Figure A.23**) Given that the similar thickness of samples, **BBL$_H$** obviously has a higher scattering intensity in both (d00) and (010) peaks. We next quantified the crystal orientation distribution with pole figures and calculated the relative degree of crystallinity (rDoC) by integrating the peak area through following equation:

$$\text{rDoC} \propto \int_{\chi_{\min}}^{\frac{\pi}{2}} I(\chi) \cdot sin\chi \, d\chi$$

where $\chi_{\min}$ is the minimum χ allowed by the GIWAXS geometry. **BBL$_H$** is more predominant edge-on orientation ($\chi < 45°$) than **BBL$_L$** (Figure SXC). The rDoC for BBL_L was calculated to be 0.81 ± 0.04 that of BBL_H. These data demonstrate that the BBL_H is more crystalline and highly ordered than BBL_L, which may explain its enhanced electronic mobility.

Surprisingly, the higher crystallinity does not harm the volumetric capacitance in **BBL$_H$**. Some previous studies on the molecular weight effect in OFETs suggest that short polymer backbones may be not sufficient to form tie-chains connection between crystalline domains.[78, 180-182] Thus, we speculated that the lower probability of tie-chains in **BBL$_L$** system is likely to generate some "dead zone" for electrons. Since C^* describes the ionic–electronic coupling in the polymer, which is related to electronic carrier density, the ion-accessible sites are limited by the electron "dead zone".

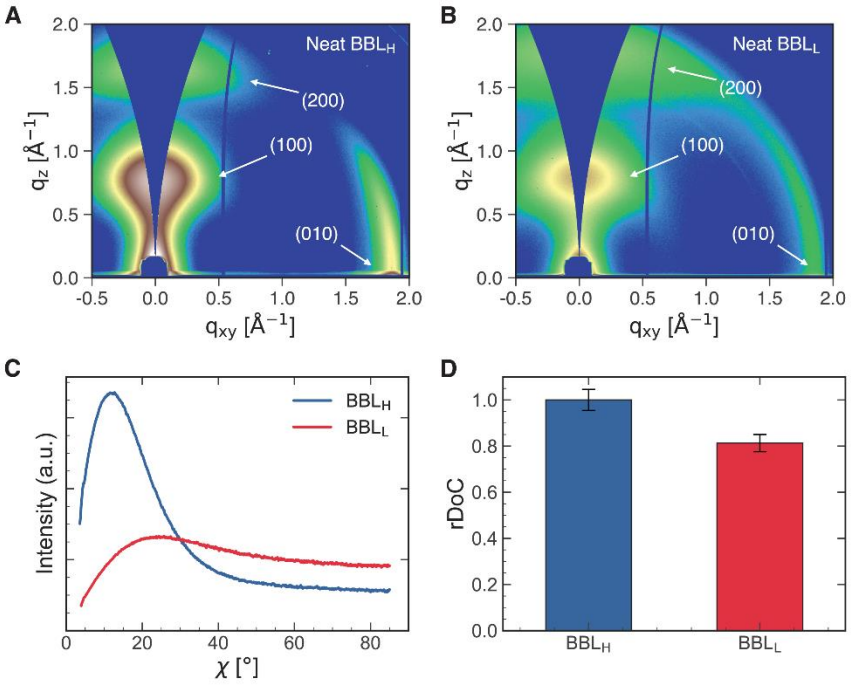

Figure A.23 Comparison between *ex-situ* GIWAXS of two BBLs. 2D GIWAXS images of **BBL$_H$** (A) and **BBL$_L$** (B). The Lorentz corrected partial pole figure (C) and calculated relative degree of crystallinity (rDoC) of two BBLs based on (100) peak. The corrected intensity $\sin(\chi)\cdot I(\chi)$ represents the relative population of the crystallites with a particular orientation χ. The relative degree of crystallinity (rDoC) is obtained by integrating the peak area and normalized to **BBL$_H$**. The rDoC for **BBL$_L$** was calculated to be 0.81 ± 0.04 that of **BBL$_H$**. The error bars were extracted from the normalized standard deviation over scattering vector *q*.

A.2 THE IMPACT OF ORR DURING BBL ELECTROCHEMICAL PROCESS

Previous studies reported that BBL provides electrocatalysis that fully reduces oxygen into water, via a (2+2)-electron transfer, and the electron transfer only happens from reduced BBL species.[86] In our work, we performed multiple characterizations on reduced BBL samples in an ambient environment. Thus, it is essential to take the ORR into account and understand how ORR affects the results, especially the currents and charges.

First of all, thanks to the unfavorable energetics, the reduced BBL does not undergo oxygen chemisorption, which results in a great stability of the BBL backbone.[86] However, due to the

significant ORR electrocatalytic activity of negatively doped BBL (BBL^-), the electrode current during the doping process includes both electron transports from BBL reduction and oxygen reduction. As a result, the integral charges calculated from doping process will overestimate the charged BBL amount. While during the dedoping process, the charge could be transferred from the reduced BBL either to the current collector, or to the oxygen in the electrolyte. Thus, the integral charges calculated from the dedoping process might underestimate the charged BBL amount. **Figure A.24A−B** show the recorded current and charge during the doping and dedoping process. In the doping process, after a quick spiking, the current maintains in a relatively high level with the increasing integral charges. While in the dedoping process, the current decays to a minimal level along with a charge saturation. Given that the concept of volumetric capacitance, charging behavior of the BBL polymer should be similar to that of a capacitor. Thus, we conclude that the charge transfer after tens of seconds during the doping step is dominantly attributed to ORR, not BBL reduction. In addition, since the dedoping steps were taken under −0.3 V, which is below the ORR-on-BBL onset potential (≈−0.1 V vs. Ag/AgCl),[86] we believe that the dedoping current is less affected by ORR, and more accurate for the BBL doping density calculation. (**Figure A.11**)

Furthermore, we calculated the charge amounts for both BBLs during both doping and dedoping process to estimate the fraction of ORR during the BBL electrochemical process. (**Figure A.24 C,D**) Over the entire potential window, **BBL_L** has a higher fraction of ORR charge transfer, which may result from a lower ion-charge coupling sites we observed in the volumetric capacitance.

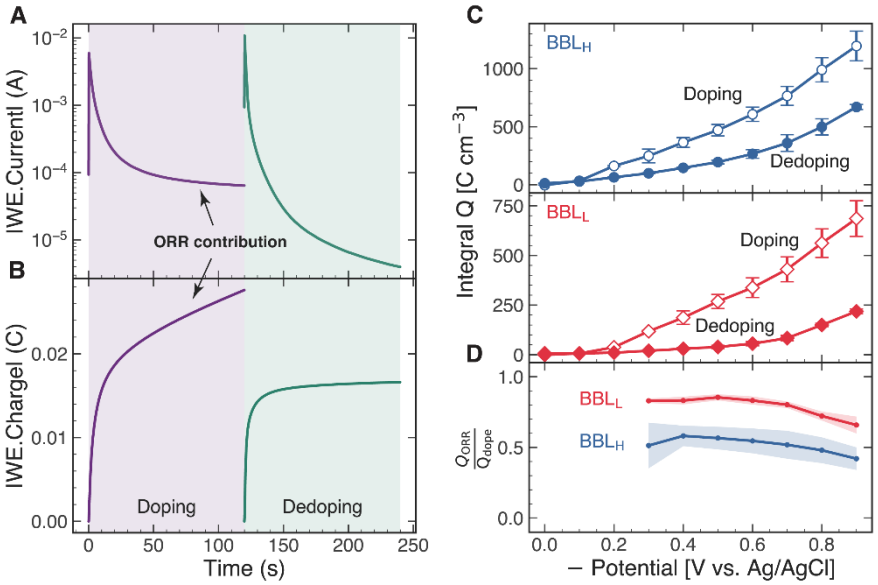

Figure A.24 . ORR impact on the UV−Vis measurements. Typical doping/dedoping working electrode current (A) and its integral charge (B) before a UV−Vis spectrum was taken. The data was taken with a BBL_H (WE) | Pt (CE) | Ag/AgCl (RE) 3-electrode electrochemical system in 100 mmol KCl solution. Doping potential: −0.8 V; Dedoping potential: +0.3 V (*vs.* Ag/AgCl) C) The integral charge amounts calculated with doping current (open symbol) and dedoping current (solid) for both **BBL_H** (top) and **BBL_L** (bottom). D) The fraction of the ORR charge amount in the doping charge amount. The error bars represent the standard error of the mean over 3 measurements.

Similar ORR impact was also observed in the QCM measurement. To minimize the ORR impact. The charge calculations in the QCM measurement are also based on the dedoping current. Given that the ORR fractions are at most ~ 10% for **BBL_H** or ~ 18% for **BBL_L**, we feel our reported charges are accurate to much better than 20%.

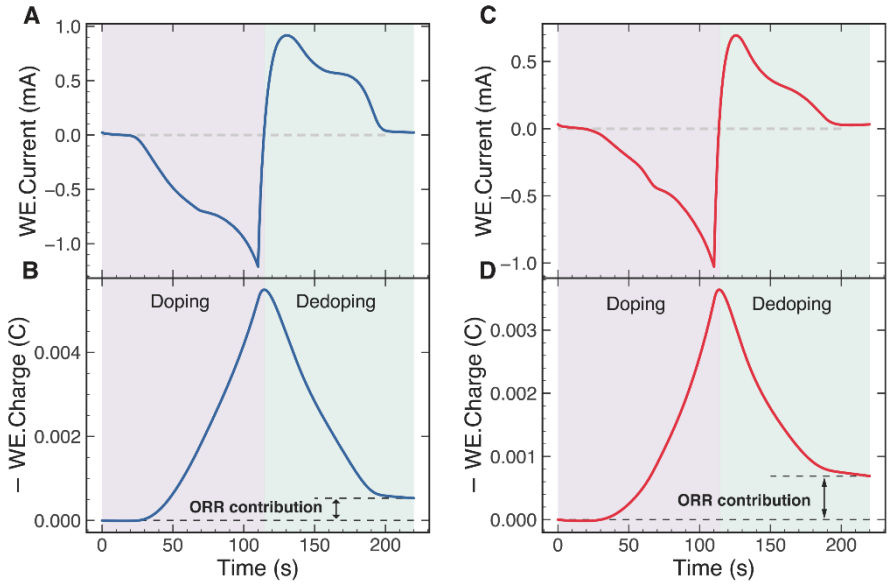

Figure A.25 ORR impact in the QCM measurements. The recorded electrode currents (A, C) and integral charges (B, D) for BBL_H (left) and BBL_L (right).

Appendix B. SUPPLEMENTARY INFORMATION FOR CHAPTER 3

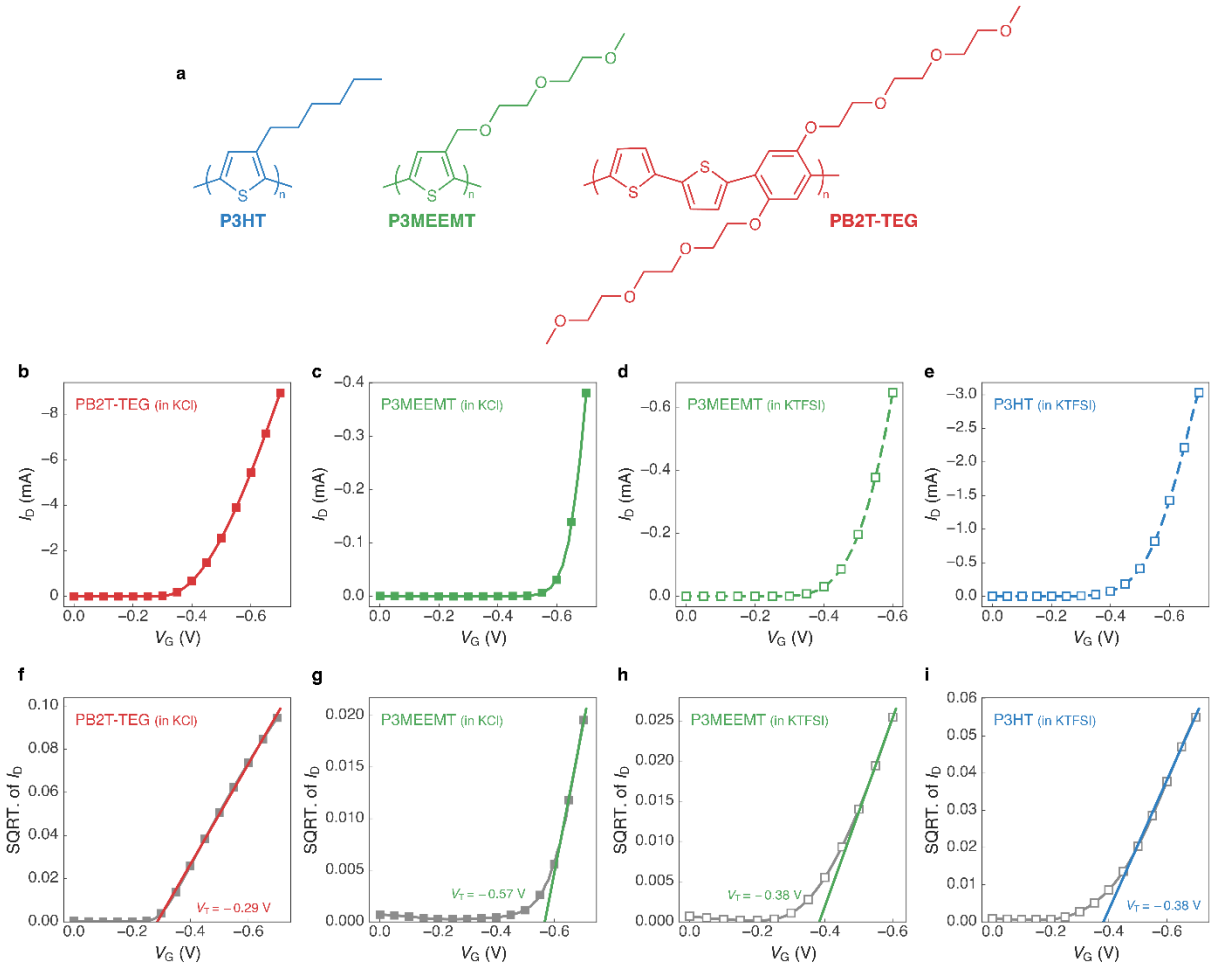

Figure B.1 Transfer curves and threshold voltage determination. (a) The polymer structure of P3HT, P3MEEMT, and PB2T-TEG (b-e) transfer curves and (e-i) threshold voltage fits of polymers in 0.1 M KCl and 0.1 M KTFSI.

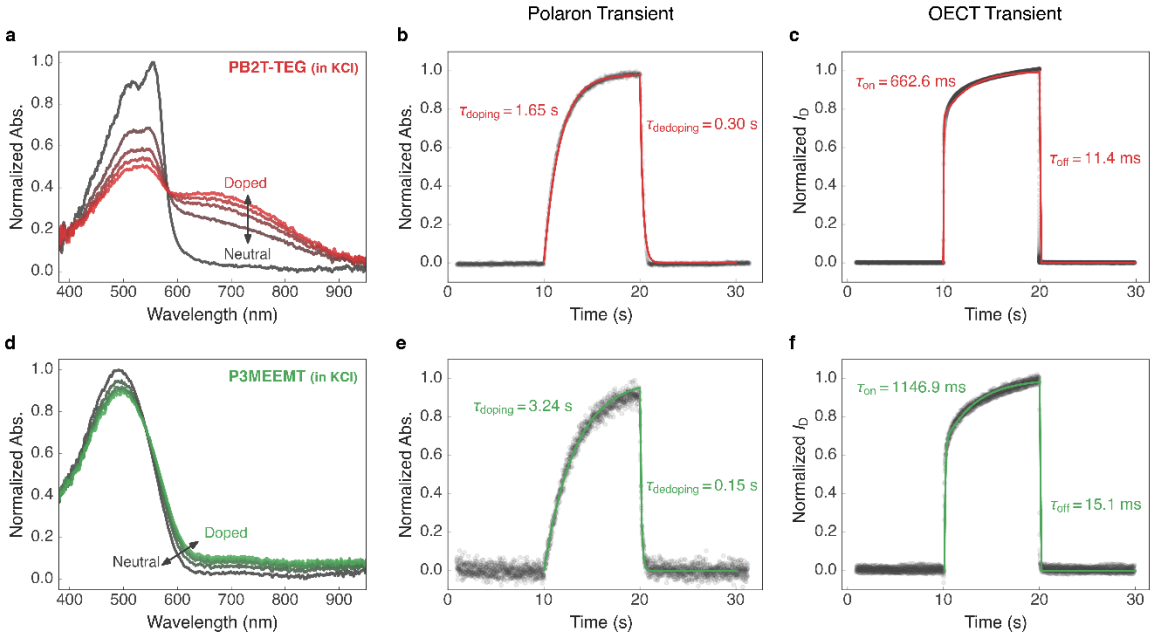

Figure B.2 The comparison between spectroelectrochemistry and OECT transient behaviors in 0.1 M KCl. The UV-Vis spectra of (a) PB2T-TEG and (d) P3MEEMT in 0.1 M KCl. The Polaron transient of (b) PB2T-TEG and (e) P3MEEMT in 0.1 M KCl. The OECT transient of (c) PB2T-TEG and (f) P3MEEMT in 0.1 M KCl. Dots represent the data and lines represent the fit in (b), (c), (e), and (f).

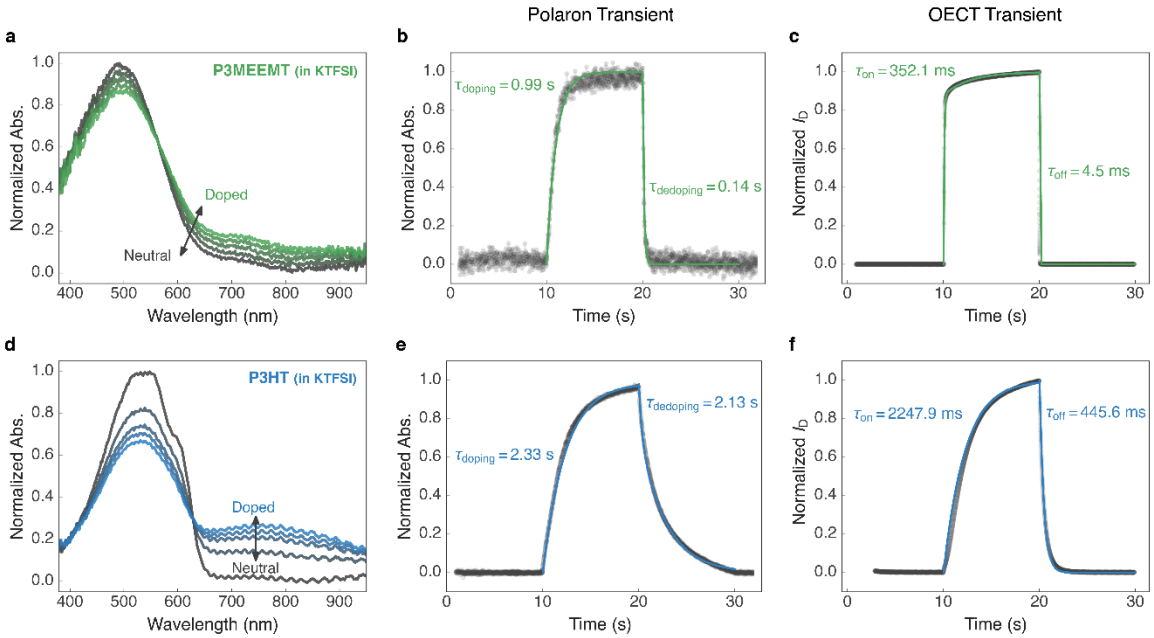

Figure B.3 The comparison between spectroelectrochemistry and OECT transient behaviors in 0.1 M KTFSI. The UV-Vis spectra of (a) PB2T-TEG and (d) P3MEEMT in 0.1 M KTFSI. The polaron transient of (b) PB2T-TEG and (e) P3MEEMT in 0.1 M KTFSI. The OECT transient of (c) PB2T-TEG and (f) P3MEEMT in 0.1 M KTFSI. Dots represent the data and lines represent the fit in (b), (c), (e), and (f).

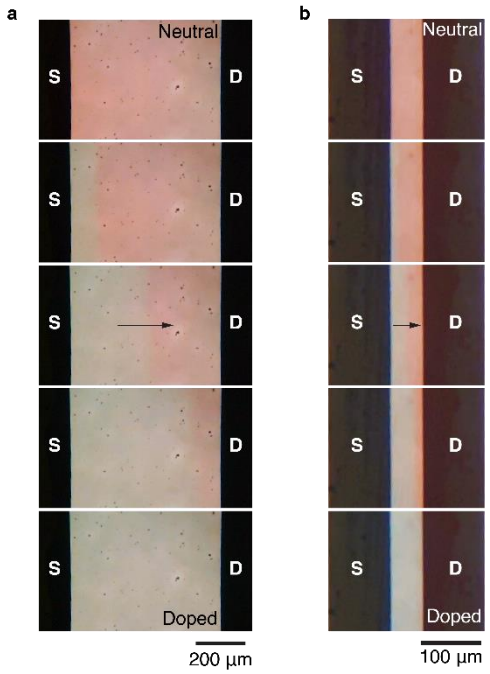

Figure B.4 Microscope screenshots of P3MEEMT OECT channels during operation. Turn-on process of P3MEEMT-based OECT with the channel length of (a) 600 µm (b) 50 µm. The electrolyte is 0.1 M KCl. Arrows indicate the doping front propagation direction. The color of the P3MEEMT polymer is red/orange in the neutral state and blue in the doped state.

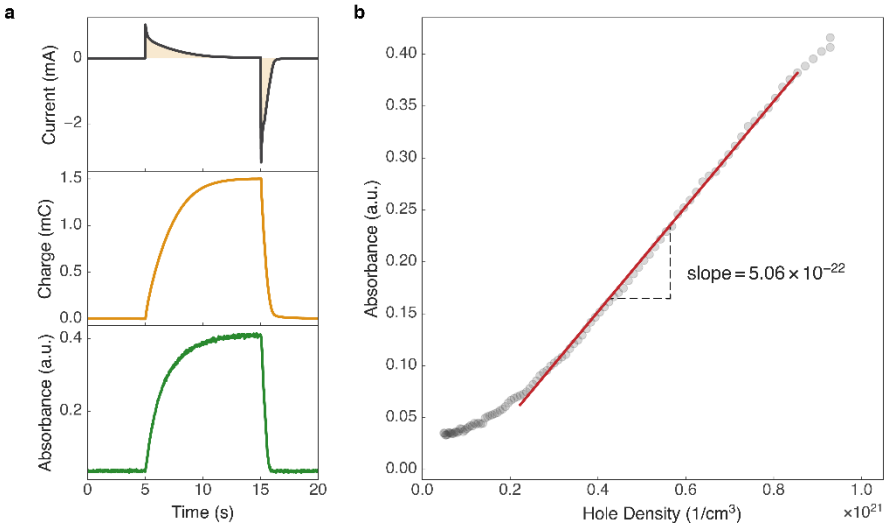

Figure B.5 The absorption-hole density calibration based on Beer's law. (a) The transient response of current, charge, and absorbance of PB2T-TEG in spectroelectrochemistry. The electrolyte is 0.1 M KCl. (b) The relation between absorbance and hole density.

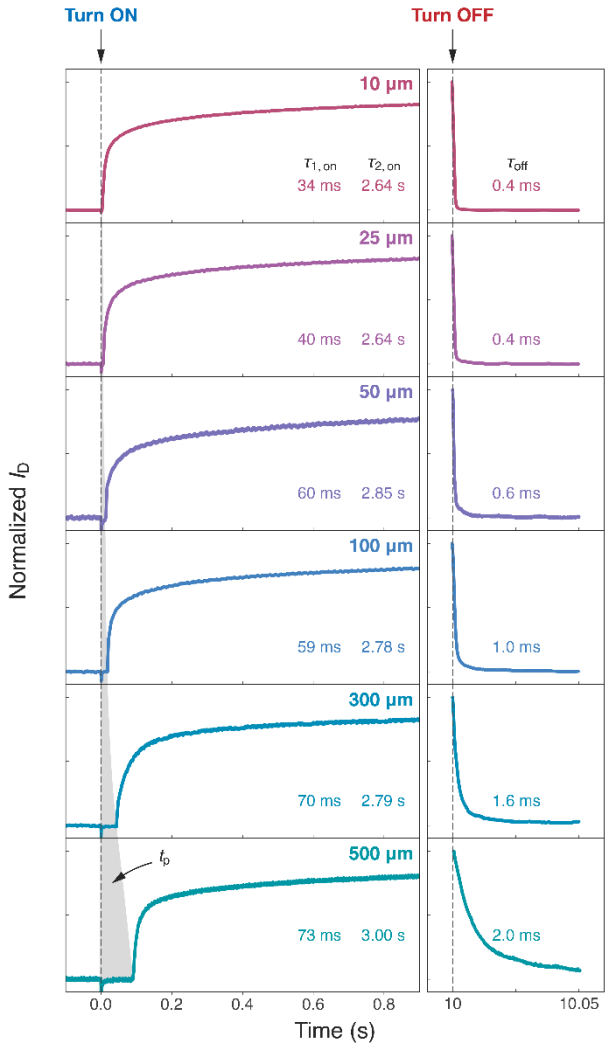

Figure B.6 The transient response with various channel lengths. The polymer is PB2T-TEG, and the electrolyte is 0.1 M KCl. The transistor channel width is 5 mm and the film thickness is ≈ 50 nm. The gate potential is fixed at $|V_G - V_T| = 0.2$ V, and the drain potential is – 0.6 V.

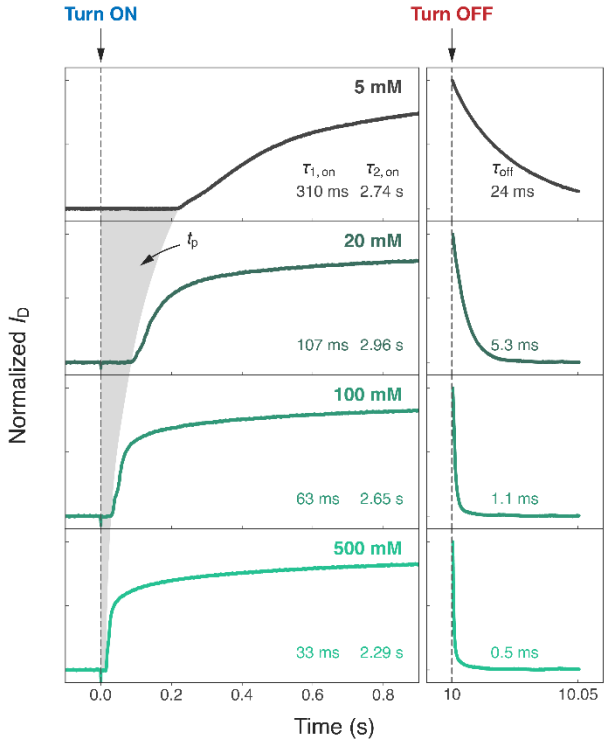

Figure B.7 The transient response with various ion concentrations. The polymer is PB2T-TEG. The transistor channel width is 2.5 mm, the channel length is 100 μm and the film thickness is ≈ 50 nm. The gate potential is fixed at $|V_G - V_T| = 0.2$ V, and the drain potential is – 0.6 V.

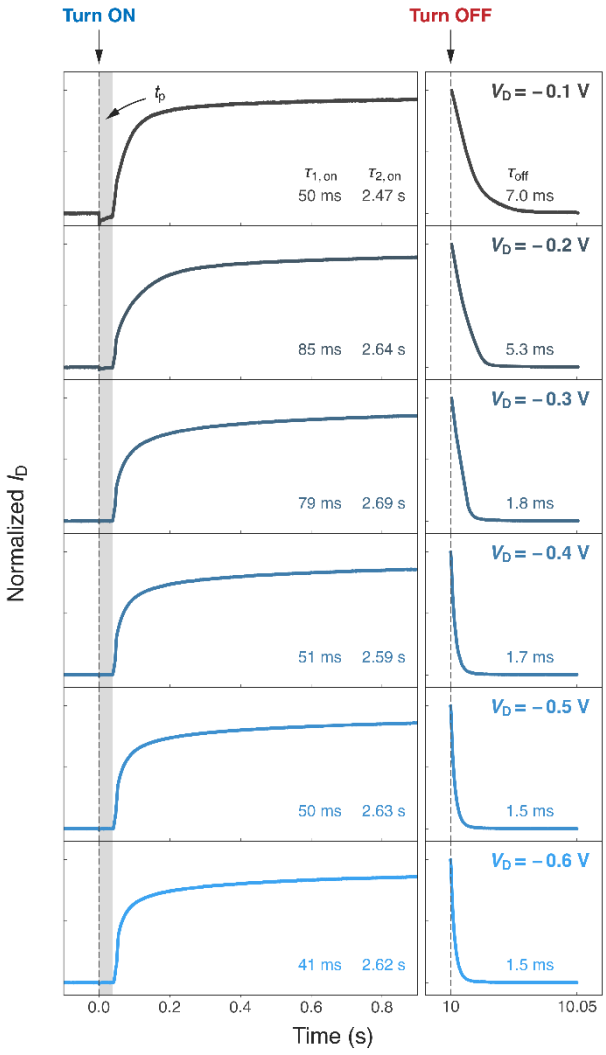

Figure B.8 The transient response with various drain potentials. The polymer is PB2T-TEG, and the electrolyte is 0.1 M KCl. The transistor channel width is 5 mm, the channel length is 100 μm, and the film thickness is ≈ 50 nm. The gate potential is fixed at $|V_G - V_T| = 0.2$ V.

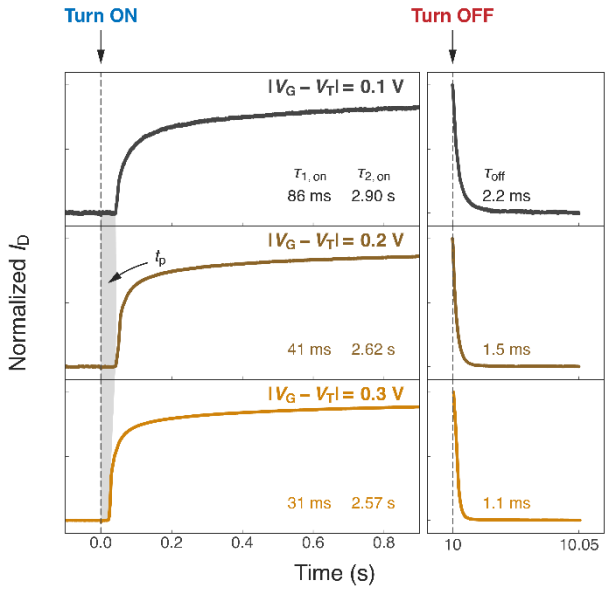

Figure B.9 The transient response with various gate potentials. The polymer is PB2T-TEG, and the electrolyte is 0.1 M KCl. The transistor channel width is 5 mm, the channel length is 100 μm, and the film thickness is ≈ 50 nm. The drain potential is – 0.6 V.

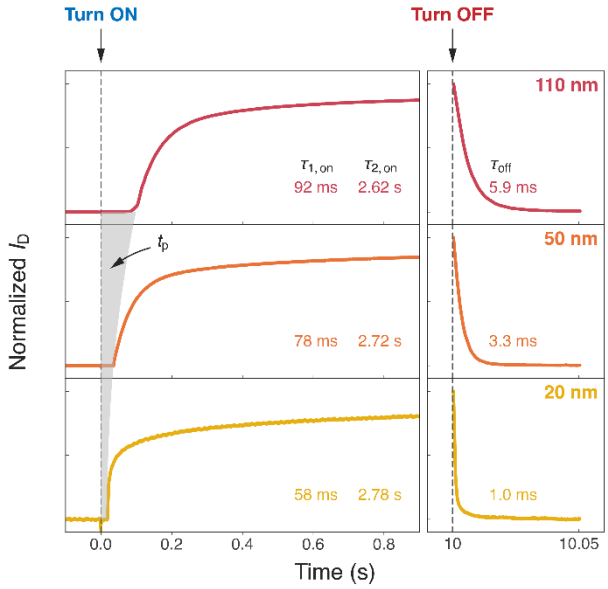

Figure B.10 The transient response with various film thickness. The polymer is PB2T-TEG, and the electrolyte is 0.1 M KCl. The transistor channel width is 5 mm, and the channel length is 100 μm. The gate potential is fixed at $|V_G - V_T| = 0.2$ V, and the drain potential is – 0.6 V.

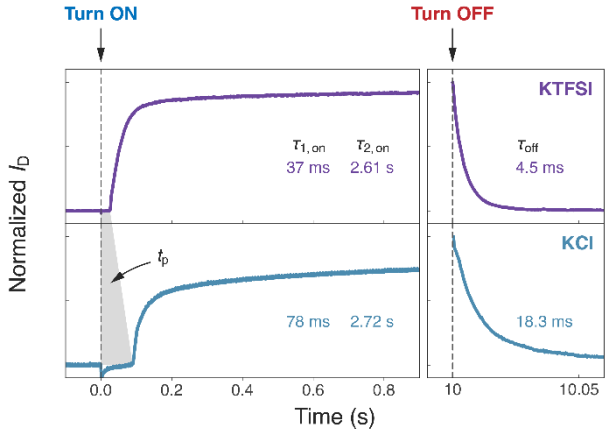

Figure B.11 The transient response with various counter anion species. The polymer is P3MEEMT. The transistor channel width is 5 mm, the channel length is 100 μm, and the film thickness is ≈ 120 nm. The gate potential is fixed at $|V_G - V_T| = 0.2$ V, and the drain potential is – 0.6 V.

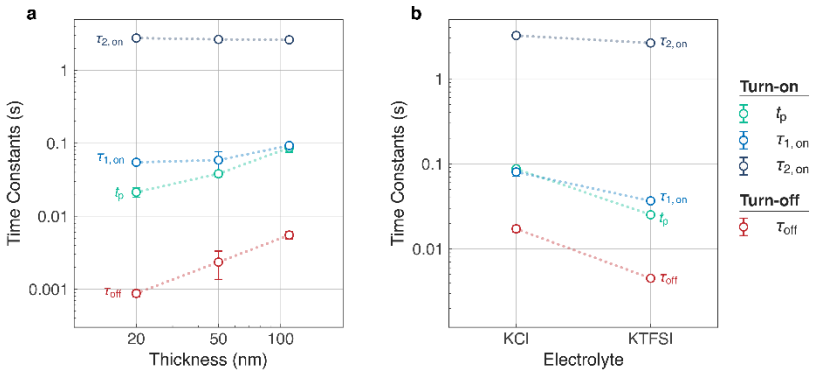

Figure B.12 The relation between response time constants and thickness or electrolyte.(Results from **Figure B.10** and **Figure B.11**). Error bars represent the standard deviation from multiple cycles.

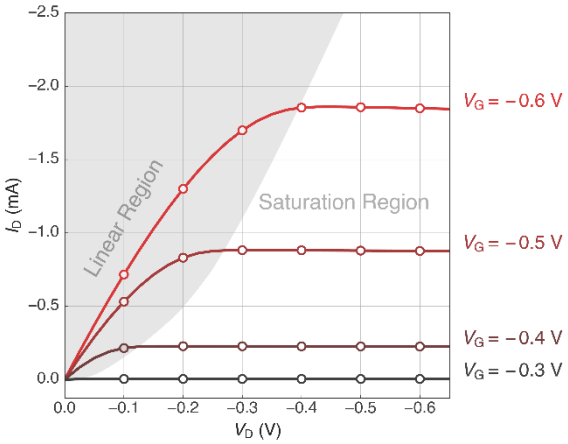

Figure B.13 The output curve of PB2T-TEG in 0.1 M KCl.

Table B.1 OCP and V_T values of different polymer/electrolyte pairs

Polymer	Electrolyte	OCP (V)[a]	V_T (V)[b]
PB2T-TEG	0.1 M KCl	0.11	-0.29
P3MEEMT	0.1 M KCl	0.13	-0.57
P3MEEMT	0.1 M KTFSI	-0.03	-0.38
P3HT	0.1 M KTFSI	-0.12	-0.38

[a] Open circuit potential of the system.

[b] OECT threshold voltage. See Figure B.1.

Table B.2 Response time constants of spectroelectrochemistry and OECT

Polymer	Electrolyte	SpecEChem τ_{doping} (s) [a]	OECT τ_{on} (s) [b]	SpecEChem $\tau_{dedoping}$ (s) [c]	OECT τ_{off} (s) [d]
PB2T-TEG	0.1 M KCl	1.69 ± 0.01	0.65828 ± 0.00701	0.29 ± 0.01	0.00124 ± 0.00002
P3MEEMT	0.1 M KCl	3.17 ± 0.07	1.14873 ± 0.03257	0.16 ± 0.01	0.01693 ±0.00075
P3MEEMT	0.1 M KTFSI	1.05 ± 0.03	0.34316 ± 0.00515	0.15 ± 0.01	0.00447 ± 0.00004
P3HT	0.1 M KTFSI	2.67 ± 0.35	2.25052 ± 0.01539	2.18 ± 0.05	0.44508 ± 0.00134

[a] Average tau from biexponential fit or single exponential fit. Error bars represent standard error of the mean from multiple cycles. Time resolution of spectroelectrochemistry is ≈ 10 ms.

[b] Average tau from biexponential fit. We did not consider propagation time (t_p) here. Error bars represent standard error of the mean from multiple cycles. Time resolution of OECT is ≈ 10 μs.

[c] Average tau from biexponential fit or single exponential fit. Error bars represent standard error of the mean from multiple cycles.

[d] Tau from single exponential fit. Error bars represent standard error of the mean from multiple cycles.

B.1 TRANSIENT FITS WITH BERNARDS MODEL

The Bernards model considers the transient behavior of an OECT as the characteristic of charging or discharging a capacitor.[137] Assuming charging or discharging occurs uniformly along the channel polymer, they proposed that I_D to have a single exponential response when switching between two steady-states:

$$I_D(t, V_G) = I_{ss}(V_G) + \Delta I_{ss}\left(1 - f\frac{\tau_e}{\tau_i}\right) \cdot e^{-t/\tau_i} \quad \textbf{(B-1)}$$

where I_{SS} is the steady-state channel current, and ΔI_{SS} is the current difference between two different steady-states. f determines the ratio of I_{GS} and I_{GD}. τ_e is the electronic charge transit time and τ_i is the product of $R_S \cdot C_{Ch}$. The R_S is the electrolyte resistance and the C_{Ch} is the channel capacitance.[137] They demonstrated the I_D response to be either a monotonic decay or a spike-and-recovery depending on the ratio between $f\tau_e$ and τ_i, with device switching speed determined by τ_i.[137]

As shown in **Figure 3.1 a**, we found that Bernards model cannot accurately describe the transient response of accumulation mode OECTs. Most importantly, the Bernards model cannot explain the much faster device turn-off speed compared to turn-on phenomenon, which, based on the model, should be both equal to τ_i, as R_S and C_{Ch} are the same. We believe the reasons why Bernards model failed to predict the switching behavior of accumulation mode OECTs are as follows: first, the uniform charging or discharging assumption is inaccurate. Second, the carrier density dependent mobility needs to be considered, especially during device turn-off. Last, Bernards and Malliaras developed the model based on poly(3,4-ethylenedioxythiophene) doped with poly(styrene sulfonate) (PEDOT:PSS), which is a depletion mode OECT material.

B.2 OFF-INTERVAL DEPENDENT OECT TURN-ON KINETICS

Figure B.14 shows faster OECT turn-on kinetics through shortening the off-interval. To ensure the same electrochemical doping level is achieved, we fixed the on-interval to be 30 s for each cycle while varying the off-interval from 30 s to 1 s. Since the τ_{off} is much smaller than τ_{on} (see main text), the device could be turned off even with 1s off-interval in this case. It is clear that transistor turns on faster (smaller τ_{on}) with shorter off-interval. This phenomenon occurs because even though the transistor is at off-state already, dedoping of the channel polymer is not fully completed (see **Chapter 3**).

This behavior also implies that accumulation mode OECT turn-on kinetics is duty cycle dependent if the total period is carefully selected. Duty cycle is defined as the ratio between on-interval over the total period, and the total period is the sum of the on-interval and the off-interval. The duty-dependent kinetics may be beneficial for emulating neuron dynamic filtering function, in which the post synaptic response (i.e. I_D) depends on the duty of the presynaptic stimuli (i.e. V_G). Previously, Gkoupidenis et al.[164] and Yamamoto et al.[163] had demonstrated the dynamic filtering function with depletion mode, PEDOT:PSS-based OECTs.

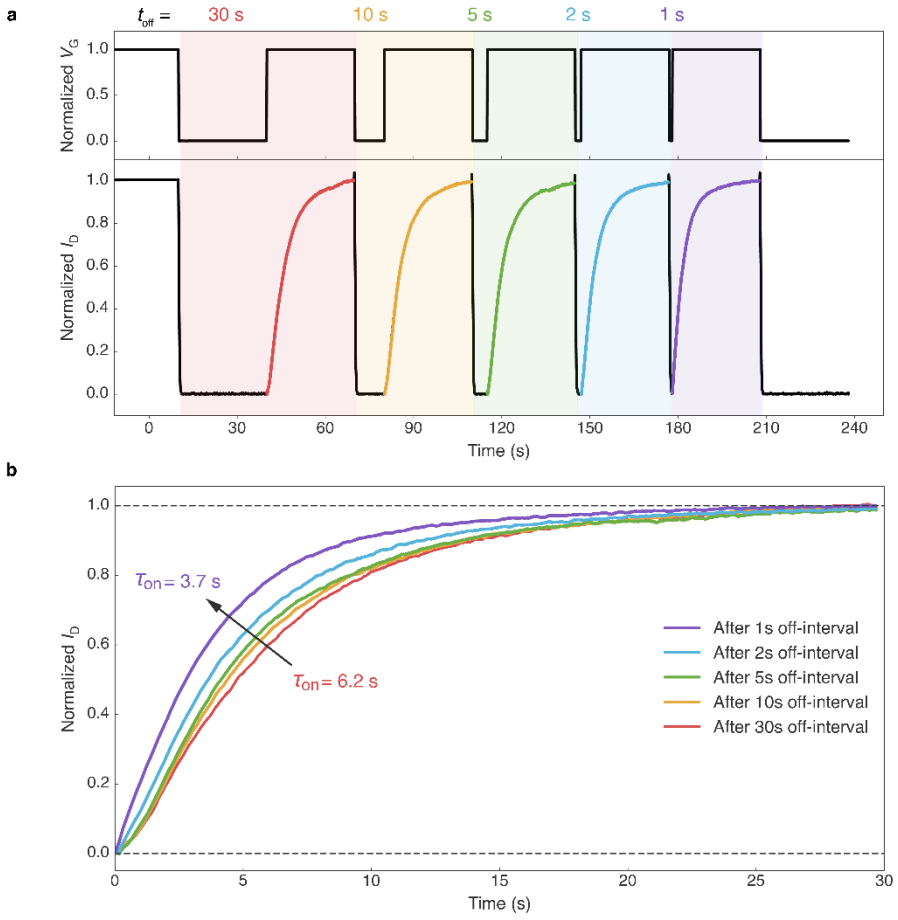

Figure B.14 The transient response after different off-interval. (a) The transient response of a P3HT-based OECT with a fixed on-interval (30 s) and various off-intervals. Pre indicates previous runs for device stabilization. Numbers represent the cycle number. Transistor channel width, length and thickness is 4000 μm, 10 μm and ≈ 100 nm, respectively. (b) Comparison between turn-on kinetics with various off-intervals.

B.3 CARRIER DENSITY-DEPENDENT MOBILITY

Previously, with the exponentially distributed density of states (DOS) assumption, Friedlein et al. proposed the relation between OECT mobility and carrier concentration to be:

$$\mu = \mu_0 \cdot \left(\frac{p}{p_0}\right)^{\frac{E_0}{k_B T}-1} \quad \textbf{(B-2)}$$

where μ_0 is mobility prefactor and p_0 is zero-filed hole concentration. E_0 describes the energetic width of the tail of the density of states, k_B is Boltzmann's constant and T is temperature.[165] We found that our mobility and carrier concentration relation could be well characterized with this equation (**Figure 3.4 b** and **Figure B.15 a**). The E_0 obtained from mobility and carrier concentration fit is ≈ 300 meV.

To justify our fitting result, we further estimated the E_0 value from the ultraviolet photoelectron spectroscopy (UPS) spectra data from our previous work.[170] **Figure B.15 b** shows the estimation of E_0 value of PB2T-TEG via the exponential fit of the edge of HOMO region. We found the E_0 value is ≈ 204 meV, which we believe is close to the value obtained from mobility and carrier concentration fit, considering the difficulty to accurately determine the width of DOS via different techniques,[183, 184] and the possible broadening of DOS after doping.[185] The similar E_0 values obtained by two different methods verify that our approach studying mobility and carrier density relation is feasible.

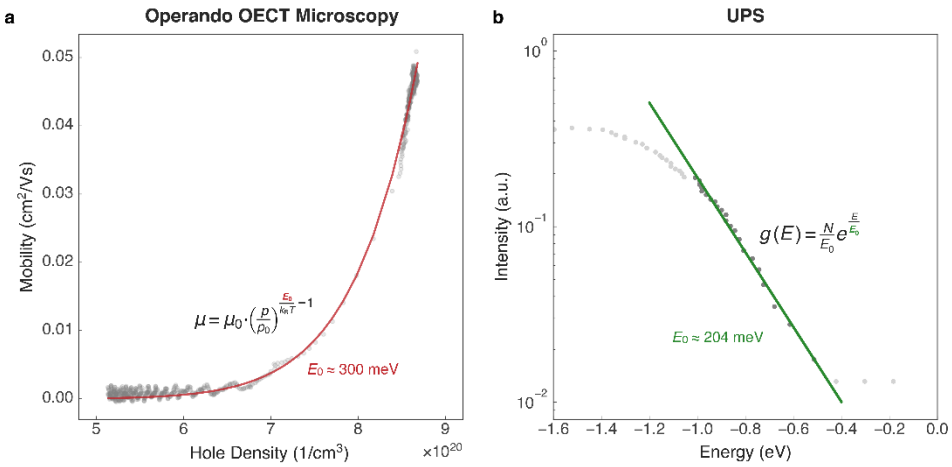

Figure B.15 The estimation of the energetic width of the tail of the density of states (E_0) with (a) OECT mobility and concentration fit and (b) via ultraviolet photoelectron spectroscopy (UPS). *N* represents number of states, *E* is the energy, and *g* is the DOS in the equation in (b).

B.4 SPICE SIMULATION

Here, we attempt to replicate the delayed turn-on (doping front propagation stage) and asymmetric kinetics via circuit modeling. To the best of our knowledge, Ersman et al. are the only ones to report an OECT circuit model including active elements and show asymmetric kinetics with depletion mode OECTs.[144] In their approach, a diode was used to represent the discharging path from the body of a SPICE MOSFET model. Though their model can indeed represent asymmetric kinetics, it does not intuitively capture the physics of an OECT, because unlike a MOSFET, there is no body terminal in an OECT. On the other hand, purely passive element circuit models are very popular, as in those developed by Bernards et al. and Faria et al. that have seen widespread adoption.[137, 142] However, such circuit models are linear and thus cannot exhibit different turn-on and turn-off kinetics. For details, the reader is referred to reviews on circuit model kinetics,[168, 186, 187] and a more systematic modeling is beyond the scope of this manuscript.

To reconcile these two approaches with our experimental data, based on the classical $R_s+(R_{ct}||C_p)$ model commonly used in literature,[142, 188] we include a time-dependent resistance to represent the channel polymer resistivity. The RC component could reflect the initial "spike" in both I_G and I_D, while the time-dependent resistance could replicate the timing. **Figure B.16 a** shows the proposed equivalent circuit model. Here, V_G is the gate potential and V_D is the drain potential. R_s is the solution resistance, $R_D(t)$ is the time-dependent resistance and R_{ss} is the source electrode contact used for measuring current in SPICE simulation. C_p and R_{ct} are the polymer volume capacitance and charge transfer resistance commonly applied in Randles circuit. R_s, C_p, R_{ct} have limited effects on the kinetics through the channel in this proposed model, where they represent the electrolyte-drain interface, rather than the entire active layer. We also included a constant current source to represent the gate leakage current, $f \times I_G$, which does not affect the

kinetics here. The detailed explanation of *f* factor could be found in Faria and Bernards models.[137, 142]

Figure B.16 b shows the transient response and SPICE simulation result of an example accumulation mode P3HT OECT operating 0.1 M KTFSI. (*W*/*L*/*d* = 5 mm/100 μm/100 nm) The drain potential is fixed at −0.6 V while the on-potential is −0.2 V and off-potential is −0.6 V. We modeled the time-dependent resistance $R_D(t)$ by an exponential decay from a high resistance (undoped) state to a low resistance state (doped) or vice versa:

$$R_D(t) = \begin{cases} V_D/I_{D,sat} + C\left(1 - e^{-\frac{t}{\tau_{off}}}\right) & \text{(turn-off)} \\ V_D/I_{D,sat} + Ae^{-\frac{t}{\tau_1}} + Be^{-\frac{t}{\tau_2}} & \text{(turn-on)} \end{cases} \quad \textbf{(B-3)}$$

where *A*, *B*, and *C* are constants. $I_{D,sat}$ is the expected saturation current, or the on-state current. τ_1, τ_2, and τ_{off} are the time constants associated with the transistor turn-on stage (which has two components as discussed in the main text), and the transistor turn-off stage. We demonstrated that the SPICE model could accurately reflect the transient asymmetry, with the time constants τ_1, τ_2, and τ_{off} being 0.7 s, 2 s, and 0.5 s, consistent with observations of faster device turn-off behavior. We also note that the parameters used for fitting here including solution resistance ($R_s \approx 1$ kΩ), polymer volume capacitance ($C_p \approx 2.4$ μF) and charge transfer resistance ($R_{ct} \approx 10$ kΩ) are all close to the actual physical values, verifying the proposed model captures the physics of OECT switching. Constants related to time-dependent resistance, namely, *A*, *B* and *C* all have values around 1000 in this specific example. We expect these values to vary with different polymers and channel geometry. All SPICE simulations were performed with LTSpice (freely available from Analog Devices).

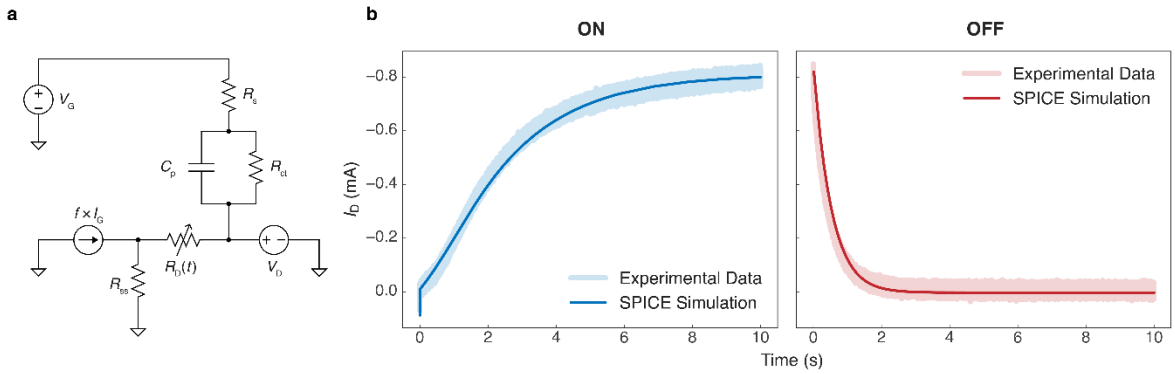

Figure B.16 SPICE simulation of an accumulation mode OECT. **a**, LTSpice circuit model. Here, we used f = 0.5, though in this work the nature of f parameter is not under investigation. R_{ss} is used only for simulation purposes to measure the total source current, and it is generally a trivially low resistance (0.01 Ω). The other values are defined in the discussion above. **b**, Experimental data of an example accumulation mode P3HT OECT operates in 0.1 M KTFSI and the SPICE simulation results. ($W/L/d$ = 5 mm/100 µm/100 nm) The drain potential is fixed at −0.6 V while the on-potential is −0.6 V and off-potential is −0.2 V. We showed that the turn-on and turn-off kinetics are well represented by the circuit.

BIBLIOGRAPHY

1. Chen, D.; Pei, Q., Electronic Muscles and Skins: A Review of Soft Sensors and Actuators. *Chemical Reviews* **2017,** *117* (17), 11239-11268.

2. Beaujuge, P. M.; Reynolds, J. R., Color Control in π-Conjugated Organic Polymers for Use in Electrochromic Devices. *Chemical Reviews* **2010,** *110* (1), 268-320.

3. Keene, S. T.; Fogarty, D.; Cooke, R.; Casadevall, C. D.; Salleo, A.; Parlak, O., Wearable Organic Electrochemical Transistor Patch for Multiplexed Sensing of Calcium and Ammonium Ions from Human Perspiration. *Advanced Healthcare Materials* **2019,** *8* (24), 1901321.

4. Filho, G.; Júnior, C.; Spinelli, B.; Damasceno, I.; Fiuza, F.; Morya, E., All-Polymeric Electrode Based on PEDOT:PSS for In Vivo Neural Recording. **2022,** *12* (10), 853.

5. Jakešová, M.; Sjöström, T. A.; Đerek, V.; Poxson, D.; Berggren, M.; Głowacki, E. D.; Simon, D. T., Wireless organic electronic ion pumps driven by photovoltaics. *npj Flexible Electronics* **2019,** *3* (1).

6. Rivnay, J.; Inal, S.; Salleo, A.; Owens, R. M.; Berggren, M.; Malliaras, G. G., Organic electrochemical transistors. *Nat Rev Mater* **2018,** *3* (2), 17086.

7. Ji, X.; Paulsen, B. D.; Chik, G. K. K.; Wu, R.; Yin, Y.; Chan, P. K. L.; Rivnay, J., Mimicking associative learning using an ion-trapping non-volatile synaptic organic electrochemical transistor. *Nature communications* **2021,** *12* (1).

8. Paterson, A. F.; Savva, A.; Wustoni, S.; Tsetseris, L.; Paulsen, B. D.; Faber, H.; Emwas, A. H.; Chen, X.; Nikiforidis, G.; Hidalgo, T. C.; Moser, M.; Maria, I. P.; Rivnay, J.; McCulloch, I.; Anthopoulos, T. D.; Inal, S., Water stable molecular n-doping produces organic electrochemical transistors with high transconductance and record stability. *Nature communications* **2020,** *11* (1), 3004.

9. Heeger, A. J., Semiconducting polymers: the Third Generation. *Chemical Society Reviews* **2010,** *39* (7), 2354.

10. Tropp, J.; Meli, D.; Rivnay, J., Organic mixed conductors for electrochemical transistors. *Matter* **2023**.

11. Giovannitti, A.; Sbircea, D. T.; Inal, S.; Nielsen, C. B.; Bandiello, E.; Hanifi, D. A.; Sessolo, M.; Malliaras, G. G.; McCulloch, I.; Rivnay, J., Controlling the mode of operation of organic transistors through side-chain engineering. *Proc. Natl. Acad. Sci. U. S. A.* **2016,** *113* (43), 12017-12022.

12. Moro, S.; Siemons, N.; Drury, O.; Warr, D. A.; Moriarty, T. A.; Perdigão, L. M. A.; Pearce, D.; Moser, M.; Hallani, R. K.; Parker, J.; Mcculloch, I.; Frost, J. M.; Nelson, J.; Costantini, G., The Effect of Glycol Side Chains on the Assembly and Microstructure of Conjugated Polymers. *ACS Nano* **2022,** *16* (12), 21303-21314.

13. Chen, S. E.; Flagg, L. Q.; Onorato, J. W.; Richter, L. J.; Guo, J. J.; Luscombe, C. K.; Ginger, D. S., Impact of varying side chain structure on organic electrochemical transistor performance: a series of oligoethylene glycol-substituted polythiophenes. *J Mater Chem A* **2022,** *10* (19), 10738-10749.

14. Flagg, L. Q.; Bischak, C. G.; Onorato, J. W.; Rashid, R. B.; Luscombe, C. K.; Ginger, D. S., Polymer Crystallinity Controls Water Uptake in Glycol Side-Chain Polymer Organic Electrochemical Transistors. *J. Am. Chem. Soc.* **2019,** *141* (10), 4345-4354.

15. Li, P.; Shi, J.; Lei, Y.; Huang, Z.; Lei, T., Switching p-type to high-performance n-type organic electrochemical transistors via doped state engineering. *Nature communications* **2022,** *13* (1), 5970.

16. Griggs, S.; Marks, A.; Bristow, H.; McCulloch, I., n-Type organic semiconducting polymers: stability limitations, design considerations and applications. *J. Mater. Chem. C Mater.* **2021,** *9* (26), 8099-8128.

17. Kim, B.-G.; Ma, X.; Chen, C.; Ie, Y.; Coir, E. W.; Hashemi, H.; Aso, Y.; Green, P. F.; Kieffer, J.; Kim, J., Energy Level Modulation of HOMO, LUMO, and Band-Gap in Conjugated Polymers for Organic Photovoltaic Applications. *Adv Funct Mater* **2013,** *23* (4), 439-445.

18. Nielsen, C. B.; Giovannitti, A.; Sbircea, D.-T.; Bandiello, E.; Niazi, M. R.; Hanifi, D. A.; Sessolo, M.; Amassian, A.; Malliaras, G. G.; Rivnay, J.; Mcculloch, I., Molecular Design of

Semiconducting Polymers for High-Performance Organic Electrochemical Transistors. *Journal of the American Chemical Society* **2016,** *138* (32), 10252-10259.

19. Zhang, X.; Bronstein, H.; Kronemeijer, A. J.; Smith, J.; Kim, Y.; Kline, R. J.; Richter, L. J.; Anthopoulos, T. D.; Sirringhaus, H.; Song, K.; Heeney, M.; Zhang, W.; Mcculloch, I.; Delongchamp, D. M., Molecular origin of high field-effect mobility in an indacenodithiophene–benzothiadiazole copolymer. *Nature communications* **2013,** *4* (1).

20. Sun, H.; Vagin, M.; Wang, S.; Crispin, X.; Forchheimer, R.; Berggren, M.; Fabiano, S., Complementary Logic Circuits Based on High-Performance n-Type Organic Electrochemical Transistors. *Adv. Mater.* **2018,** *30* (9), 1704916.

21. Moser, M.; Hidalgo, T. C.; Surgailis, J.; Gladisch, J.; Ghosh, S.; Sheelamanthula, R.; Thiburce, Q.; Giovannitti, A.; Salleo, A.; Gasparini, N.; Wadsworth, A.; Zozoulenko, I.; Berggren, M.; Stavrinidou, E.; Inal, S.; McCulloch, I., Side Chain Redistribution as a Strategy to Boost Organic Electrochemical Transistor Performance and Stability. *Adv. Mater.* **2020,** *32* (37), e2002748.

22. Keene, S. T.; Gueskine, V.; Berggren, M.; Malliaras, G. G.; Tybrandt, K.; Zozoulenko, I., Exploiting mixed conducting polymers in organic and bioelectronic devices. *Physical Chemistry Chemical Physics* **2022,** *24* (32), 19144-19163.

23. Surgailis, J.; Savva, A.; Druet, V.; Paulsen, B. D.; Wu, R.; Hamidi‐Sakr, A.; Ohayon, D.; Nikiforidis, G.; Chen, X.; McCulloch, I.; Rivnay, J.; Inal, S., Mixed Conduction in an N‐Type Organic Semiconductor in the Absence of Hydrophilic Side‐Chains. *Adv. Funct. Mater.* **2021,** *31* (21), 2010165.

24. Wu, R.; Paulsen, B. D.; Ma, Q.; Rivnay, J., Mass and Charge Transport Kinetics in an Organic Mixed Ionic−Electronic Conductor. *Chem Mater* **2022,** *34* (21), 9699--9710.

25. Bischak, C. G.; Flagg, L. Q.; Yan, K.; Rehman, T.; Davies, D. W.; Quezada, R. J.; Onorato, J. W.; Luscombe, C. K.; Diao, Y.; Li, C. Z.; Ginger, D. S., A Reversible Structural Phase Transition by Electrochemically-Driven Ion Injection into a Conjugated Polymer. *J. Am. Chem. Soc.* **2020,** *142* (16), 7434-7442.

26. Guo, J.; Flagg, L. Q.; Tran, D. K.; Chen, S. E.; Li, R.; Kolhe, N. B.; Giridharagopal, R.; Jenekhe, S. A.; Richter, L. J.; Ginger, D. S., Hydration of a Side-Chain-Free n-Type Semiconducting Ladder Polymer Driven by Electrochemical Doping. *J Am Chem Soc* **2023,** *145* (3), 1866-1876.

27. Inal, S.; Malliaras, G. G.; Rivnay, J., Benchmarking organic mixed conductors for transistors. *Nat. Commun.* **2017,** *8* (1), 1767.

28. Kaphle, V.; Paudel, P. R.; Dahal, D.; Radha Krishnan, R. K.; Lussem, B., Finding the equilibrium of organic electrochemical transistors. *Nature communications* **2020,** *11* (1), 2515.

29. Szumska, A. A.; Maria, I. P.; Flagg, L. Q.; Savva, A.; Surgailis, J.; Paulsen, B. D.; Moia, D.; Chen, X.; Griggs, S.; Mefford, J. T.; Rashid, R. B.; Marks, A.; Inal, S.; Ginger, D. S.; Giovannitti, A.; Nelson, J., Reversible Electrochemical Charging of n-Type Conjugated Polymer Electrodes in Aqueous Electrolytes. *J. Am. Chem. Soc.* **2021,** *143* (36), 14795-14805.

30. Wałęsa-Chorab, M.; Skene, W. G., Extending the Color Retention of an Electrochromic Device by Immobilizing Color Switching and Ion-Storage Complementary Layers. *Electronic Materials* **2020,** *1* (1), 40-53.

31. Flagg, L. Q.; Giridharagopal, R.; Guo, J.; Ginger, D. S., Anion-Dependent Doping and Charge Transport in Organic Electrochemical Transistors. *Chem. Mater.* **2018,** *30* (15), 5380-5389.

32. Chen, S. E.; Flagg, L. Q.; Onorato, J. W.; Richter, L. J.; Guo, J.; Luscombe, C. K.; Ginger, D. S., Impact of varying side chain structure on organic electrochemical transistor performance: a series of oligoethylene glycol-substituted polythiophenes. *J. Mater. Chem. A* **2022,** *10* (19), 10738-10749.

33. Savva, A.; Cendra, C.; Giugni, A.; Torre, B.; Surgailis, J.; Ohayon, D.; Giovannitti, A.; McCulloch, I.; Di Fabrizio, E.; Salleo, A.; Rivnay, J.; Inal, S., Influence of Water on the Performance of Organic Electrochemical Transistors. *Chem. Mater.* **2019,** *31* (3), 927-937.

34. Friedlein, J. T.; Donahue, M. J.; Shaheen, S. E.; Malliaras, G. G.; McLeod, R. R., Microsecond Response in Organic Electrochemical Transistors: Exceeding the Ionic Speed Limit. *Adv Mater* **2016,** *28* (38), 8398-8404.

35. Coppede, N.; Villani, M.; Gentile, F., Diffusion driven selectivity in organic electrochemical transistors. *Sci Rep* **2014,** *4*, 4297.

36. Friedlein, J. T.; Rivnay, J.; Dunlap, D. H.; McCulloch, I.; Shaheen, S. E.; McLeod, R. R.; Malliaras, G. G., Influence of disorder on transfer characteristics of organic electrochemical transistors. *Appl Phys Lett* **2017,** *111* (2).

37. Parr, Z. S.; Rashid, R. B.; Paulsen, B. D.; Poggi, B.; Tan, E.; Freeley, M.; Palma, M.; Abrahams, I.; Rivnay, J.; Nielsen, C. B., Semiconducting Small Molecules as Active Materials for p‐Type Accumulation Mode Organic Electrochemical Transistors. *Advanced Electronic Materials* **2020,** *6* (6), 2000215.

38. Spano, F. C., The Spectral Signatures of Frenkel Polarons in H- and J-Aggregates. *Accounts of Chemical Research* **2010,** *43* (3), 429-439.

39. Massonnet, N.; Carella, A.; Jaudouin, O.; Rannou, P.; Laval, G.; Celle, C.; Simonato, J. P., Improvement of the Seebeck coefficient of PEDOT:PSS by chemical reduction combined with a novel method for its transfer using free-standing thin films. *J Mater Chem C* **2014,** *2* (7), 1278-1283.

40. Jackson, S. R.; Kingsford, R. L.; Collins, G. W.; Bischak, C. G., Crystallinity Determines Ion Injection Kinetics and Local Ion Density in Organic Mixed Conductors. *Chem Mater* **2023**.

41. Wada, Y.; Enokida, I.; Yamamoto, J.; Furukawa, Y., Raman imaging of carrier distribution in the channel of an ionic liquid-gated transistor fabricated with regioregular poly(3-hexylthiophene). *Spectrochim Acta A Mol Biomol Spectrosc* **2018,** *197*, 166-169.

42. Thelen, J. L.; Wu, S.-L.; Javier, A. E.; Srinivasan, V.; Balsara, N. P.; Patel, S. N., Relationship between Mobility and Lattice Strain in Electrochemically Doped Poly(3-hexylthiophene). *ACS Macro Letters* **2015,** *4* (12), 1386-1391.

43. Thomas, E. M.; Brady, M. A.; Nakayama, H.; Popere, B. C.; Segalman, R. A.; Chabinyc, M. L., X‐Ray Scattering Reveals Ion‐Induced Microstructural Changes During Electrochemical Gating of Poly(3‐Hexylthiophene). *Adv Funct Mater* **2018,** *28* (44), 1803687.

44. Paulsen, B. D.; Giovannitti, A.; Wu, R.; Strzalka, J.; Zhang, Q.; Rivnay, J.; Takacs, C. J., Electrochemistry of Thin Films with In Situ/Operando Grazing Incidence X-Ray Scattering: Bypassing Electrolyte Scattering for High Fidelity Time Resolved Studies. *Small* **2021,** *17* (42), e2103213.

45. Wu, R.; Matta, M.; Paulsen, B. D.; Rivnay, J., Operando Characterization of Organic Mixed Ionic/Electronic Conducting Materials. *Chemical Reviews* **2022,** *122* (4), 4493-4551.

46. Mahmood, A.; Wang, J. L., A Review of Grazing Incidence Small‐ and Wide‐Angle X‐Ray Scattering Techniques for Exploring the Film Morphology of Organic Solar Cells. *Solar RRL* **2020,** *4* (10), 2000337.

47. Giridharagopal, R.; Flagg, L. Q.; Harrison, J. S.; Ziffer, M. E.; Onorato, J.; Luscombe, C. K.; Ginger, D. S., Electrochemical strain microscopy probes morphology-induced variations in ion uptake and performance in organic electrochemical transistors. *Nat. Mater.* **2017,** *16* (7), 737-742.

48. Lee, H. J.; Lee, J.; Park, S.-M., Electrochemistry of Conductive Polymers. 45. Nanoscale Conductivity of PEDOT and PEDOT:PSS Composite Films Studied by Current-Sensing AFM. *The Journal of Physical Chemistry B* **2010,** *114* (8), 2660-2666.

49. Giridharagopal, R.; Guo, J.; Kong, J.; Ginger, D. S., Nanowire Architectures Improve Ion Uptake Kinetics in Conjugated Polymer Electrochemical Transistors. *ACS Appl. Mater. Interfaces* **2021,** *13* (29), 34616-34624.

50. Xu, K.; Ruoko, T. P.; Shokrani, M.; Scheunemann, D.; Abdalla, H.; Sun, H. D.; Yang, C. Y.; Puttisong, Y.; Kolhe, N. B.; Figueroa, J. S. M.; Pedersen, J. O.; Ederth, T.; Chen, W. M.; Berggren, M.; Jenekhe, S. A.; Fazzi, D.; Kemerink, M.; Fabiano, S., On the Origin of Seebeck Coefficient Inversion in Highly Doped Conducting Polymers. *Adv. Funct. Mater.* **2022,** *32* (20), 2112276.

51. Liu, H.; Yang, A.; Song, J.; Wang, N.; Lam, P.; Li, Y.; Law, H. K.; Yan, F., Ultrafast, sensitive, and portable detection of COVID-19 IgG using flexible organic electrochemical transistors. *Sci. Adv.* **2021,** *7* (38), eabg8387.

52. Inal, S.; Rivnay, J.; Suiu, A. O.; Malliaras, G. G.; McCulloch, I., Conjugated Polymers in Bioelectronics. *Acc. Chem. Res.* **2018,** *51* (6), 1368-1376.

53. Picca, R. A.; Manoli, K.; Macchia, E.; Sarcina, L.; Di Franco, C.; Cioffi, N.; Blasi, D.; Österbacka, R.; Torricelli, F.; Scamarcio, G.; Torsi, L., Ultimately Sensitive Organic Bioelectronic Transistor Sensors by Materials and Device Structure Design. *Adv. Funct. Mater.* **2019,** *30* (20), 1904513.

54. Bischak, C. G.; Flagg, L. Q.; Ginger, D. S., Ion Exchange Gels Allow Organic Electrochemical Transistor Operation with Hydrophobic Polymers in Aqueous Solution. *Adv. Mater.* **2020,** *32* (32), e2002610.

55. Mike, J. F.; Lutkenhaus, J. L., Recent advances in conjugated polymer energy storage. *Journal of Polymer Science Part B: Polymer Physics* **2013,** *51* (7), 468-480.

56. Volkov, A. V.; Sun, H. D.; Kroon, R.; Ruoko, T. P.; Che, C. Y.; Edberg, J.; Muller, C.; Fabiano, S.; Crispin, X., Asymmetric Aqueous Supercapacitor Based on p- and n-Type Conducting Polymers. *ACS Appl. Energy Mater.* **2019,** *2* (8), 5350-5355.

57. Andersson Ersman, P.; Lassnig, R.; Strandberg, J.; Tu, D.; Keshmiri, V.; Forchheimer, R.; Fabiano, S.; Gustafsson, G.; Berggren, M., All-printed large-scale integrated circuits based on organic electrochemical transistors. *Nat. Commun.* **2019,** *10* (1), 5053.

58. Keene, S. T.; Lubrano, C.; Kazemzadeh, S.; Melianas, A.; Tuchman, Y.; Polino, G.; Scognamiglio, P.; Cina, L.; Salleo, A.; van de Burgt, Y.; Santoro, F., A biohybrid synapse with neurotransmitter-mediated plasticity. *Nat. Mater.* **2020,** *19* (9), 969-973.

59. Fuller, E. J.; Keene, S. T.; Melianas, A.; Wang, Z.; Agarwal, S.; Li, Y.; Tuchman, Y.; James, C. D.; Marinella, M. J.; Yang, J. J.; Salleo, A.; Talin, A. A., Parallel programming of an ionic floating-gate memory array for scalable neuromorphic computing. *Science* **2019,** *364* (6440), 570-574.

60. Felder, D.; Femmer, R.; Bell, D.; Rall, D.; Pietzonka, D.; Henzler, S.; Linkhorst, J.; Wessling, M., Coupled Ionic–Electronic Charge Transport in Organic Neuromorphic Devices. *Adv. Theory Simul.* **2022,** *5* (6), 2100492.

61. Flagg, L. Q.; Bischak, C. G.; Quezada, R. J.; Onorato, J. W.; Luscombe, C. K.; Ginger, D. S., P-Type Electrochemical Doping Can Occur by Cation Expulsion in a High-Performing Polymer for Organic Electrochemical Transistors. *ACS Materials Lett.* **2020,** *2* (3), 254-260.

62. Kukhta, N. A.; Marks, A.; Luscombe, C. K., Molecular Design Strategies toward Improvement of Charge Injection and Ionic Conduction in Organic Mixed Ionic-Electronic Conductors for Organic Electrochemical Transistors. *Chem. Rev.* **2022,** *122* (4), 4325-4355.

63. Li, P.; Lei, T., Molecular design strategies for high‐performance organic electrochemical transistors. *J. Polym Sci.* **2021,** *60* (3), 377-392.

64. Bischak, C. G.; Flagg, L. Q.; Yan, K.; Li, C. Z.; Ginger, D. S., Fullerene Active Layers for n-Type Organic Electrochemical Transistors. *ACS Appl. Mater. Interfaces* **2019,** *11* (31), 28138-28144.

65. Chen, X.; Marks, A.; Paulsen, B. D.; Wu, R.; Rashid, R. B.; Chen, H.; Alsufyani, M.; Rivnay, J.; McCulloch, I., n-Type Rigid Semiconducting Polymers Bearing Oligo(Ethylene Glycol) Side Chains for High-Performance Organic Electrochemical Transistors. *Angew. Chem. Int. Ed.* **2021,** *60* (17), 9368-9373.

66. Giovannitti, A.; Nielsen, C. B.; Sbircea, D. T.; Inal, S.; Donahue, M.; Niazi, M. R.; Hanifi, D. A.; Amassian, A.; Malliaras, G. G.; Rivnay, J.; McCulloch, I., N-type organic electrochemical transistors with stability in water. *Nat. Commun.* **2016,** *7*, 13066.

67. Sun, H. D.; Gerasimov, J.; Berggren, M.; Fabiano, S., n-Type organic electrochemical transistors: materials and challenges. *J. Mater. Chem. C* **2018,** *6* (44), 11778-11784.

68. Giovannitti, A.; Maria, I. P.; Hanifi, D.; Donahue, M. J.; Bryant, D.; Barth, K. J.; Makdah, B. E.; Savva, A.; Moia, D.; Zetek, M.; Barnes, P. R. F.; Reid, O. G.; Inal, S.; Rumbles, G.; Malliaras, G. G.; Nelson, J.; Rivnay, J.; McCulloch, I., The Role of the Side Chain on the Performance of N-type Conjugated Polymers in Aqueous Electrolytes. *Chem. Mater.* **2018,** *30* (9), 2945-2953.

69. Maria, I. P.; Paulsen, B. D.; Savva, A.; Ohayon, D.; Wu, R.; Hallani, R.; Basu, A.; Du, W.; Anthopoulos, T. D.; Inal, S.; Rivnay, J.; McCulloch, I.; Giovannitti, A., The Effect of Alkyl Spacers on

the Mixed Ionic ‐ Electronic Conduction Properties of N ‐ Type Polymers. *Adv. Funct. Mater.* **2021,** *31* (14), 2008718.

70. Jeong, D.; Jo, I. Y.; Lee, S.; Kim, J. H.; Kim, Y.; Kim, D.; Reynolds, J. R.; Yoon, M. H.; Kim, B. J., High ‐ Performance n ‐ Type Organic Electrochemical Transistors Enabled by Aqueous Solution Processing of Amphiphilicity ‐ Driven Polymer Assembly. *Adv. Funct. Mater.* **2022,** *32* (16), 2111950.

71. Ohayon, D.; Savva, A.; Du, W.; Paulsen, B. D.; Uguz, I.; Ashraf, R. S.; Rivnay, J.; McCulloch, I.; Inal, S., Influence of Side Chains on the n-Type Organic Electrochemical Transistor Performance. *ACS Appl. Mater. Interfaces* **2021,** *13* (3), 4253-4266.

72. Feng, K.; Shan, W.; Ma, S.; Wu, Z.; Chen, J.; Guo, H.; Liu, B.; Wang, J.; Li, B.; Woo, H. Y.; Fabiano, S.; Huang, W.; Guo, X., Fused Bithiophene Imide Dimer-Based n-Type Polymers for High-Performance Organic Electrochemical Transistors. *Angew.Chem.* **2021,** *133*, 24400– 24407.

73. Wu, H. Y.; Yang, C. Y.; Li, Q.; Kolhe, N. B.; Strakosas, X.; Stoeckel, M. A.; Wu, Z.; Jin, W.; Savvakis, M.; Kroon, R.; Tu, D.; Woo, H. Y.; Berggren, M.; Jenekhe, S. A.; Fabiano, S., Influence of Molecular Weight on the Organic Electrochemical Transistor Performance of Ladder-Type Conjugated Polymers. *Adv. Mater.* **2022,** *34* (4), e2106235.

74. Proctor, C. M.; Rivnay, J.; Malliaras, G. G., Understanding volumetric capacitance in conducting polymers. *Journal of Polymer Science Part B: Polymer Physics* **2016,** *54* (15), 1433-1436.

75. Sahalianov, I.; Singh, S. K.; Tybrandt, K.; Berggren, M.; Zozoulenko, I., The intrinsic volumetric capacitance of conducting polymers: pseudo-capacitors or double-layer supercapacitors? *RSC Adv.* **2019,** *9* (72), 42498-42508.

76. Wang, S.; Sun, H.; Ail, U.; Vagin, M.; Persson, P. O.; Andreasen, J. W.; Thiel, W.; Berggren, M.; Crispin, X.; Fazzi, D.; Fabiano, S., Thermoelectric Properties of Solution-Processed n-Doped Ladder-Type Conducting Polymers. *Adv. Mater.* **2016,** *28* (48), 10764-10771.

77. Kim, F. S.; Park, C. H.; Na, Y. N.; Jenekhe, S. A., Effects of ladder structure on the electronic properties and field-effect transistor performance of Poly(benzobisimidazobenzophenanthroline). *Org Electron* **2019,** *69*, 301-307.

78. Gu, K.; Snyder, C. R.; Onorato, J.; Luscombe, C. K.; Bosse, A. W.; Loo, Y. L., Assessing the Huang-Brown Description of Tie Chains for Charge Transport in Conjugated Polymers. *ACS Macro Lett.* **2018,** *7* (11), 1333-1338.

79. Wang, H.; Xu, Y.; Yu, X.; Xing, R.; Liu, J.; Han, Y., Structure and Morphology Control in Thin Films of Conjugated Polymers for an Improved Charge Transport. *Polymers* **2013,** *5* (4), 1272-1324.

80. Noriega, R.; Rivnay, J.; Vandewal, K.; Koch, F. P.; Stingelin, N.; Smith, P.; Toney, M. F.; Salleo, A., A general relationship between disorder, aggregation and charge transport in conjugated polymers. *Nat. Mater.* **2013,** *12* (11), 1038-1044.

81. Kline, R. J.; McGehee, M. D.; Kadnikova, E. N.; Liu, J.; Fréchet, J. M. J., Controlling the Field-Effect Mobility of Regioregular Polythiophene by Changing the Molecular Weight. *Adv. Mater.* **2003,** *15* (18), 1519-1522.

82. Li, J.; Zhao, Y.; Tan, H. S.; Guo, Y.; Di, C. A.; Yu, G.; Liu, Y.; Lin, M.; Lim, S. H.; Zhou, Y.; Su, H.; Ong, B. S., A stable solution-processed polymer semiconductor with record high-mobility for printed transistors. *Sci. Rep.* **2012,** *2* (1), 754.

83. Hayashi, S.; Yamamoto, S. I.; Koizumi, T., Effects of molecular weight on the optical and electrochemical properties of EDOT-based pi-conjugated polymers. *Sci. Rep.* **2017,** *7* (1), 1078.

84. Meier, H.; Stalmach, U.; Kolshorn, H., Effective conjugation length and UV/vis spectra of oligomers. *Acta Polymer.* **1997,** *48* (9), 379-384.

85. Gierschner, J.; Huang, Y. S.; Van Averbeke, B.; Cornil, J.; Friend, R. H.; Beljonne, D., Excitonic versus electronic couplings in molecular assemblies: The importance of non-nearest neighbor interactions. *J. Chem. Phys.* **2009,** *130* (4), 044105.

86. Vagin, M.; Gueskine, V.; Mitraka, E.; Wang, S.; Singh, A.; Zozoulenko, I.; Berggren, M.; Fabiano, S.; Crispin, X., Negatively‐Doped Conducting Polymers for Oxygen Reduction Reaction. *Adv. Energy Mater*. **2021,** *11* (3), 2002664.

87. Nicolini, T.; Surgailis, J.; Savva, A.; Scaccabarozzi, A. D.; Nakar, R.; Thuau, D.; Wantz, G.; Richter, L. J.; Dautel, O.; Hadziioannou, G.; Stingelin, N., A Low-Swelling Polymeric Mixed Conductor Operating in Aqueous Electrolytes. *Adv. Mater.* **2021,** *33* (2), e2005723.

88. Denison, D. R., Linearity of a Heavily Loaded Quartz Crystal Microbalance. *Journal of Vacuum Science and Technology* **1973,** *10* (1), 126-129.

89. Behrndt, K. H., Long-Term Operation of Crystal Oscillators in Thin-Film Deposition. *Journal of Vacuum Science and Technology* **1971,** *8* (5), 622-626.

90. Vogt, B. D.; Lin, E. K.; Wu, W.-L.; White, C. C., Effect of Film Thickness on the Validity of the Sauerbrey Equation for Hydrated Polyelectrolyte Films. *J. Phys. Chem. B* **2004,** *108* (34), 12685-12690.

91. Cendra, C.; Giovannitti, A.; Savva, A.; Venkatraman, V.; McCulloch, I.; Salleo, A.; Inal, S.; Rivnay, J., Role of the Anion on the Transport and Structure of Organic Mixed Conductors. *Adv. Funct. Mater*. **2019,** *29* (5), 1807034.

92. Mancinelli, R.; Botti, A.; Bruni, F.; Ricci, M. A.; Soper, A. K., Hydration of sodium, potassium, and chloride ions in solution and the concept of structure maker/breaker. *J. Phys. Chem. B* **2007,** *111* (48), 13570-13577.

93. Mahler, J.; Persson, I., A study of the hydration of the alkali metal ions in aqueous solution. *Inorg. Chem.* **2012,** *51* (1), 425-438.

94. Schmode, P.; Savva, A.; Kahl, R.; Ohayon, D.; Meichsner, F.; Dolynchuk, O.; Thurn-Albrecht, T.; Inal, S.; Thelakkat, M., The Key Role of Side Chain Linkage in Structure Formation and Mixed Conduction of Ethylene Glycol Substituted Polythiophenes. *ACS Appl. Mater. Interfaces* **2020,** *12* (11), 13029-13039.

95. Balke, N.; Kalnaus, S.; Dudney, N. J.; Daniel, C.; Jesse, S.; Kalinin, S. V., Local detection of activation energy for ionic transport in lithium cobalt oxide. *Nano Lett.* **2012,** *12* (7), 3399-3403.

96. Balke, N.; Jesse, S.; Kim, Y.; Adamczyk, L.; Tselev, A.; Ivanov, I. N.; Dudney, N. J.; Kalinin, S. V., Real space mapping of Li-ion transport in amorphous Si anodes with nanometer resolution. *Nano Lett.* **2010,** *10* (9), 3420-3425.

97. Balke, N.; Jesse, S.; Morozovska, A. N.; Eliseev, E.; Chung, D. W.; Kim, Y.; Adamczyk, L.; Garcia, R. E.; Dudney, N.; Kalinin, S. V., Nanoscale mapping of ion diffusion in a lithium-ion battery cathode. *Nat. Nanotech.* **2010,** *5* (10), 749-754.

98. Balke, N.; Jesse, S.; Kim, Y.; Adamczyk, L.; Ivanov, I. N.; Dudney, N. J.; Kalinin, S. V., Decoupling electrochemical reaction and diffusion processes in ionically-conductive solids on the nanometer scale. *ACS Nano.* **2010,** *4* (12), 7349-7357.

99. Alikin, D. O.; Romanyuk, K. N.; Slautin, B. N.; Rosato, D.; Shur, V. Y.; Kholkin, A. L., Quantitative characterization of the ionic mobility and concentration in Li-battery cathodes via low frequency electrochemical strain microscopy. *Nanoscale* **2018,** *10* (5), 2503-2511.

100. Morozovska, A. N.; Eliseev, E. A.; Balke, N.; Kalinin, S. V., Local probing of ionic diffusion by electrochemical strain microscopy: Spatial resolution and signal formation mechanisms. *J. Appl. Phys.* **2010,** *108* (5), 053712.

101. Paulsen, B. D.; Wu, R.; Takacs, C. J.; Steinruck, H. G.; Strzalka, J.; Zhang, Q.; Toney, M. F.; Rivnay, J., Time-Resolved Structural Kinetics of an Organic Mixed Ionic-Electronic Conductor. *Adv. Mater.* **2020,** *32* (40), e2003404.

102. Flagg, L. Q.; Asselta, L. E.; D'Antona, N.; Nicolini, T.; Stingelin, N.; Onorato, J. W.; Luscombe, C. K.; Li, R.; Richter, L. J., In Situ Studies of the Swelling by an Electrolyte in Electrochemical Doping of Ethylene Glycol-Substituted Polythiophene. *ACS Appl. Mater. Interfaces* **2022,** *14* (25), 29052-29060.

103. Handbook of Electrochemical Impedance Spectroscopy.

104. Arnold, F. E.; Van Deusen, R. L., Preparation and Properties of High Molecular Weight, Soluble Oxobenz[de]imidazobenzimidazoisoquinoline Ladder Polymer. *Macromolecules* **2002,** *2* (5), 497-502.

105. Berry, G. C., Properties of an optically anisotropic heterocyclic ladder polymer (BBL) in dilute solution. *Journal of Polymer Science: Polymer Symposia* **1978,** *65* (1), 143-172.

106. Murbach, M.; Gerwe, B.; Dawson-Elli, N.; Tsui, L.-K., impedance.py: A Python package for electrochemical impedance analysis. *Journal of Open Source Software* **2020,** *5* (52), 2349.

107. Randles, J. E. B., Kinetics of Rapid Electrode Reactions. *Discuss Faraday Soc* **1947,** *1*, 11-19.

108. Hillman, A. R.; Daisley, S. J.; Bruckenstein, S., Ion and solvent transfers and trapping phenomena during n-doping of PEDOT films. *Electrochim Acta* **2008,** *53* (11), 3763-3771.

109. Hillman, A. R.; Daisley, S. J.; Bruckenstein, S., Kinetics and mechanism of the electrochemical p-doping of PEDOT. *Electrochem Commun* **2007,** *9* (6), 1316-1322.

110. Hexemer, A.; Bras, W.; Glossinger, J.; Schaible, E.; Gann, E.; Kirian, R.; MacDowell, A.; Church, M.; Rude, B.; Padmore, H., A SAXS/WAXS/GISAXS Beamline with Multilayer Monochromator. *J. Phys.: Conf. Ser.* **2010,** *247*, 012007.

111. Oosterhout, S. D.; Savikhin, V.; Zhang, J. X.; Zhang, Y. D.; Burgers, M. A.; Marder, S. R.; Bazan, G. C.; Toney, M. F., Mixing Behavior in Small Molecule:Fullerene Organic Photovoltaics. *Chem. Mater.* **2017,** *29* (7), 3062-3069.

112. Tran, D. K.; Robitaille, A.; Hai, I. J.; Lin, C. C.; Kuzuhara, D.; Koganezawa, T.; Chiu, Y. C.; Leclerc, M.; Jenekhe, S. A., Unified Understanding of Molecular Weight Dependence of Electron Transport in Naphthalene Diimide-Based n-Type Semiconducting Polymers. *Chem. Mater.* **2022,** *34* (21), 9644-9655.

113. Guo, K.; Wustoni, S.; Koklu, A.; Diaz-Galicia, E.; Moser, M.; Hama, A.; Alqahtani, A. A.; Ahmad, A. N.; Alhamlan, F. S.; Shuaib, M.; Pain, A.; McCulloch, I.; Arold, S. T.; Grunberg, R.; Inal, S., Rapid single-molecule detection of COVID-19 and MERS antigens via nanobody-functionalized organic electrochemical transistors. *Nat Biomed Eng* **2021,** *5* (7), 666-677.

114. Bischak, C. G.; Flagg, L. Q.; Ginger, D. S., Ion Exchange Gels Allow Organic Electrochemical Transistor Operation with Hydrophobic Polymers in Aqueous Solution. *Adv Mater* **2020,** *32* (32), e2002610.

115. Pappa, A. M.; Curto, V. F.; Braendlein, M.; Strakosas, X.; Donahue, M. J.; Fiocchi, M.; Malliaras, G. G.; Owens, R. M., Organic Transistor Arrays Integrated with Finger-Powered Microfluidics for Multianalyte Saliva Testing. *Adv. Healthc. Mater.* **2016,** *5* (17), 2295-302.

116. Strakosas, X.; Bongo, M.; Owens, R. M., The organic electrochemical transistor for biological applications. *Journal of Applied Polymer Science* **2015,** *132* (15), 41735.

117. Huang, W.; Chen, J.; Yao, Y.; Zheng, D.; Ji, X.; Feng, L. W.; Moore, D.; Glavin, N. R.; Xie, M.; Chen, Y.; Pankow, R. M.; Surendran, A.; Wang, Z.; Xia, Y.; Bai, L.; Rivnay, J.; Ping, J.; Guo, X.; Cheng, Y.; Marks, T. J.; Facchetti, A., Vertical organic electrochemical transistors for complementary circuits. *Nature* **2023,** *613* (7944), 496-502.

118. Andersson Ersman, P.; Lassnig, R.; Strandberg, J.; Tu, D.; Keshmiri, V.; Forchheimer, R.; Fabiano, S.; Gustafsson, G.; Berggren, M., All-printed large-scale integrated circuits based on organic electrochemical transistors. *Nat Commun* **2019,** *10* (1), 5053.

119. Harikesh, P. C.; Yang, C. Y.; Wu, H. Y.; Zhang, S.; Donahue, M. J.; Caravaca, A. S.; Huang, J. D.; Olofsson, P. S.; Berggren, M.; Tu, D.; Fabiano, S., Ion-tunable antiambipolarity in mixed ion-electron conducting polymers enables biorealistic organic electrochemical neurons. *Nat Mater* **2023,** *22* (2), 242-248.

120. Sarkar, T.; Lieberth, K.; Pavlou, A.; Frank, T.; Mailaender, V.; McCulloch, I.; Blom, P. W. M.; Torricelli, F.; Gkoupidenis, P., An organic artificial spiking neuron for in situ neuromorphic sensing and biointerfacing. *Nature Electronics* **2022,** *5* (11), 774-783.

121. Chen, S. E.; Giridharagopal, R.; Ginger, D. S., Artificial neuron transmits chemical signals. *Nat Mater* **2023,** *22* (4), 416-418.

122. Khodagholy, D.; Rivnay, J.; Sessolo, M.; Gurfinkel, M.; Leleux, P.; Jimison, L. H.; Stavrinidou, E.; Herve, T.; Sanaur, S.; Owens, R. M.; Malliaras, G. G., High transconductance organic electrochemical transistors. *Nature communications* **2013,** *4*, 2133.

123. Du, D.; Zou, Z.; Shin, Y.; Wang, J.; Wu, H.; Engelhard, M. H.; Liu, J.; Aksay, I. A.; Lin, Y., Sensitive immunosensor for cancer biomarker based on dual signal amplification strategy of graphene sheets and multienzyme functionalized carbon nanospheres. *Anal. Chem.* **2010,** *82* (7), 2989-95.

124. Ghittorelli, M.; Lingstedt, L.; Romele, P.; Craciun, N. I.; Kovacs-Vajna, Z. M.; Blom, P. W. M.; Torricelli, F., High-sensitivity ion detection at low voltages with current-driven organic electrochemical transistors. *Nature communications* **2018,** *9* (1), 1441.

125. Gualandi, I.; Tonelli, D.; Mariani, F.; Scavetta, E.; Marzocchi, M.; Fraboni, B., Selective detection of dopamine with an all PEDOT:PSS Organic Electrochemical Transistor. *Sci Rep* **2016,** *6*, 35419.

126. Xie, K.; Wang, N.; Lin, X.; Wang, Z.; Zhao, X.; Fang, P.; Yue, H.; Kim, J.; Luo, J.; Cui, S.; Yan, F.; Shi, P., Organic electrochemical transistor arrays for real-time mapping of evoked neurotransmitter release in vivo. *Elife* **2020,** *9*, 1--19.

127. Khodagholy, D.; Doublet, T.; Quilichini, P.; Gurfinkel, M.; Leleux, P.; Ghestem, A.; Ismailova, E.; Herve, T.; Sanaur, S.; Bernard, C.; Malliaras, G. G., In vivo recordings of brain activity using organic transistors. *Nature communications* **2013,** *4*, 1575.

128. Go, G. T.; Lee, Y.; Seo, D. G.; Lee, T. W., Organic Neuroelectronics: From Neural Interfaces to Neuroprosthetics. *Adv Mater* **2022,** *34* (45), e2201864.

129. Tang, X.; Shen, H.; Zhao, S. Y.; Li, N.; Liu, J., Flexible brain-computer interfaces. *Nature Electronics* **2023,** *6* (2), 109-118.

130. Berggren, M.; Glowacki, E. D.; Simon, D. T.; Stavrinidou, E.; Tybrandt, K., In Vivo Organic Bioelectronics for Neuromodulation. *Chem Rev* **2022,** *122* (4), 4826-4846.

131. van de Burgt, Y.; Melianas, A.; Keene, S. T.; Malliaras, G.; Salleo, A., Organic electronics for neuromorphic computing. *Nature Electronics* **2018,** *1* (7), 386-397.

132. Gumyusenge, A.; Melianas, A.; Keene, S. T.; Salleo, A., Materials Strategies for Organic Neuromorphic Devices. *Annu Rev Mater Res* **2021,** *51* (1), 47-71.

133. He, Y.; Kukhta, N. A.; Marks, A.; Luscombe, C. K., The effect of side chain engineering on conjugated polymers in organic electrochemical transistors for bioelectronic applications. *J Mater Chem C Mater* **2022,** *10* (7), 2314-2332.

134. Kukhta, N. A.; Marks, A.; Luscombe, C. K., Molecular Design Strategies toward Improvement of Charge Injection and Ionic Conduction in Organic Mixed Ionic-Electronic Conductors for Organic Electrochemical Transistors. *Chem Rev* **2022,** *122* (4), 4325-4355.

135. Zeglio, E.; Inganas, O., Active Materials for Organic Electrochemical Transistors. *Adv Mater* **2018,** *30* (44), e1800941.

136. Flagg, L. Q.; Bischak, C. G.; Quezada, R. J.; Onorato, J. W.; Luscombe, C. K.; Ginger, D. S., P-Type Electrochemical Doping Can Occur by Cation Expulsion in a High-Performing Polymer for Organic Electrochemical Transistors. *Acs Materials Letters* **2020,** *2* (3), 254-260.

137. Bernards, D. A.; Malliaras, G. G., Steady-state and transient behavior of organic electrochemical transistors. *Advanced Functional Materials* **2007,** *17* (17), 3538-3544.

138. Ohayon, D.; Druet, V.; Inal, S., A guide for the characterization of organic electrochemical transistors and channel materials. *Chem Soc Rev* **2023,** *52* (3), 1001-1023.

139. Inal, S.; Malliaras, G. G.; Rivnay, J., Benchmarking organic mixed conductors for transistors. *Nat Commun* **2017,** *8* (1), 1767.

140. Li, P.; Lei, T., Molecular design strategies for

high‐performance

organic electrochemical transistors. *Journal of Polymer Science* **2021,** *60* (3), 377-392.

141. Gentile, F.; Delmonte, D.; Solzi, M.; Villani, M.; Iannotta, S.; Zappettini, A.; Coppede, N., A theoretical model for the time varying current in organic electrochemical transistors in a dynamic regime. *Org Electron* **2016,** *35*, 59-64.

142. Faria, G. C.; Duong, D. T.; Salleo, A., On the transient response of organic electrochemical transistors. *Org Electron* **2017,** *45*, 215-221.

143. Paudel, P. R.; Skowrons, M.; Dahal, O.; Krishnan, R. K. R.; Lussem, B., The Transient Response of Organic Electrochemical Transistors. *Adv Theor Simul* **2022,** *5* (5), 2100563.

144. Andersson Ersman, P.; Westerberg, D.; Tu, D.; Nilsson, M.; Åhlin, J.; Eveborn, A.; Lagerlöf, A.; Nilsson, D.; Sandberg, M.; Norberg, P.; Berggren, M.; Forchheimer, R.; Gustafsson, G., Screen printed digital circuits based on vertical organic electrochemical transistors. *Flexible and Printed Electronics* **2017,** *2* (4), 045008.

145. Jia, H. Y.; Huang, Z.; Li, P. Y.; Zhang, S.; Wang, Y. F.; Wang, J. Y.; Gu, X. D.; Lei, T., Engineering donor-acceptor conjugated polymers for high-performance and fast-response organic electrochemical transistors. *J Mater Chem C* **2021,** *9* (14), 4927-4934.

146. Giovannitti, A.; Rashid, R. B.; Thiburce, Q.; Paulsen, B. D.; Cendra, C.; Thorley, K.; Moia, D.; Mefford, J. T.; Hanifi, D.; Weiyuan, D.; Moser, M.; Salleo, A.; Nelson, J.; McCulloch, I.; Rivnay, J., Energetic Control of Redox-Active Polymers toward Safe Organic Bioelectronic Materials. *Adv Mater* **2020,** *32* (16), e1908047.

147. Wu, X.; Tam, T. L. D.; Chen, S.; Salim, T.; Zhao, X.; Zhou, Z.; Lin, M.; Xu, J.; Loo, Y. L.; Leong, W. L., All-Polymer Bulk-Heterojunction Organic Electrochemical Transistors with Balanced Ionic and Electronic Transport. *Adv Mater* **2022,** *34* (42), e2206118.

148. Wang, Y. Z.; Hamidi-Sakr, A.; Surgailis, J.; Zhou, Y. C.; Liao, H. L.; Chen, J. X.; Zhu, G. M.; Li, Z. K.; Inal, S.; Yue, W., The effect of the donor moiety of DPP based polymers on the performance of organic electrochemical transistors. *J Mater Chem C* **2021,** *9* (38), 13338-13346.

149. Luo, X.; Shen, H.; Perera, K.; Tran, D. T.; Boudouris, B. W.; Mei, J., Designing Donor-Acceptor Copolymers for Stable and High-Performance Organic Electrochemical Transistors. *ACS Macro Lett* **2021,** *10* (8), 1061-1067.

150. Wang, Y. Z.; Zeglio, E.; Liao, H. L.; Xu, J. Q.; Liu, F.; Li, Z. K.; Maria, I. P.; Mawad, D.; Herland, A.; McCulloch, I.; Yue, W., Hybrid Alkyl-Ethylene Glycol Side Chains Enhance Substrate Adhesion and Operational Stability in Accumulation Mode Organic Electrochemical Transistors. *Chem Mater* **2019,** *31* (23), 9797-9806.

151. Giridharagopal, R.; Guo, J.; Kong, J.; Ginger, D. S., Nanowire Architectures Improve Ion Uptake Kinetics in Conjugated Polymer Electrochemical Transistors. *ACS Appl Mater Interfaces* **2021,** *13* (29), 34616-34624.

152. Wu, H. Y.; Yang, C. Y.; Li, Q.; Kolhe, N. B.; Strakosas, X.; Stoeckel, M. A.; Wu, Z.; Jin, W.; Savvakis, M.; Kroon, R.; Tu, D.; Woo, H. Y.; Berggren, M.; Jenekhe, S. A.; Fabiano, S., Influence of Molecular Weight on the Organic Electrochemical Transistor Performance of Ladder-Type Conjugated Polymers. *Adv Mater* **2022,** *34* (4), e2106235.

153. Chen, J.; Cong, S.; Wang, L.; Wang, Y.; Lan, L.; Chen, C.; Zhou, Y.; Li, Z.; McCulloch, I.; Yue, W., Backbone coplanarity manipulation via hydrogen bonding to boost the n-type performance of polymeric mixed conductors operating in aqueous electrolyte. *Mater Horiz* **2023,** *10* (2), 607-618.

154. Shi, J. W.; Li, P. Y.; Deng, X. Y.; Xu, J. C.; Huang, Z.; Lei, Y. Q.; Wang, Y. F.; Wang, J. Y.; Gu, X. D.; Lei, T., Revealing the Role of Polaron Distribution on the Performance of n-Type Organic Electrochemical Transistors. *Chemistry of Materials* **2022,** *34* (2), 864-872.

155. Feng, K.; Shan, W.; Wang, J.; Lee, J. W.; Yang, W.; Wu, W.; Wang, Y.; Kim, B. J.; Guo, X.; Guo, H., Cyano-Functionalized n-Type Polymer with High Electron Mobility for High-Performance Organic Electrochemical Transistors. *Adv Mater* **2022,** *34* (24), e2201340.

156. Wang, Y.; Zhu, G.; Zeglio, E.; Castillo, T. C. H.; Haseena, S.; Ravva, M. K.; Cong, S.; Chen, J.; Lan, L.; Li, Z.; Herland, A.; McCulloch, I.; Inal, S.; Yue, W., n-Type Organic Electrochemical Transistors with High Transconductance and Stability. *Chem Mater* **2023,** *35* (2), 405-415.

157. Feng, K.; Shan, W.; Ma, S.; Wu, Z.; Chen, J.; Guo, H.; Liu, B.; Wang, J.; Li, B.; Woo, H. Y.; Fabiano, S.; Huang, W.; Guo, X., Fused Bithiophene Imide Dimer-Based n-Type Polymers for High-Performance Organic Electrochemical Transistors. *Angew Chem Int Ed Engl* **2021,** *60* (45), 24198-24205.

158. Sun, H.; Vagin, M.; Wang, S.; Crispin, X.; Forchheimer, R.; Berggren, M.; Fabiano, S., Complementary Logic Circuits Based on High-Performance n-Type Organic Electrochemical Transistors. *Adv Mater* **2018,** *30* (9), 1704916.

159. Butler, J. A. V., Studies in heterogeneous equilibria. Part II - The kinetic interpretation of the nernst theory of electromotive force. *T Faraday Soc* **1924,** *19* (3), 0729-0733.

160. Butler, J. A. V., Studies in heterogeneous equilibria. Part III. A kinetic theory of reversible oxidation potentials at inert electrodes. *T Faraday Soc* **1924,** *19* (3), 0734-0739.

161. Erdey-Grúz, T.; Volmer, M., Zur Theorie der Wasserstoff Überspannung. *Zeitschrift für Physikalische Chemie* **1930,** *150A* (1), 203-213.

162. Bischak, C. G.; Flagg, L. Q.; Yan, K.; Rehman, T.; Davies, D. W.; Quezada, R. J.; Onorato, J. W.; Luscombe, C. K.; Diao, Y.; Li, C. Z.; Ginger, D. S., A Reversible Structural Phase Transition by Electrochemically-Driven Ion Injection into a Conjugated Polymer. *J Am Chem Soc* **2020,** *142* (16), 7434-7442.

163. Yamamoto, S.; Malliaras, G. G., Controlling the Neuromorphic Behavior of Organic Electrochemical Transistors by Blending Mixed and Ion Conductors. *Acs Appl Electron Ma* **2020,** *2* (7), 2224-2228.

164. Gkoupidenis, P.; Schaefer, N.; Garlan, B.; Malliaras, G. G., Neuromorphic Functions in PEDOT:PSS Organic Electrochemical Transistors. *Adv Mater* **2015,** *27* (44), 7176-80.

165. Friedlein, J. T.; Shaheen, S. E.; Malliaras, G. G.; McLeod, R. R., Optical Measurements Revealing Nonuniform Hole Mobility in Organic Electrochemical Transistors. *Advanced Electronic Materials* **2015,** *1* (11), 1500189.

166. Tanase, C.; Meijer, E. J.; Blom, P. W.; De Leeuw, D. M., Unification of the hole transport in polymeric field-effect transistors and light-emitting diodes. *Phys Rev Lett* **2003,** *91* (21), 216601.

167. Flagg, L. Q.; Bischak, C. G.; Onorato, J. W.; Rashid, R. B.; Luscombe, C. K.; Ginger, D. S., Polymer Crystallinity Controls Water Uptake in Glycol Side-Chain Polymer Organic Electrochemical Transistors. *J Am Chem Soc* **2019,** *141* (10), 4345-4354.

168. Colucci, R.; Barbosa, H. F. D.; Gunther, F.; Cavassin, P.; Faria, G. C., Recent advances in modeling organic electrochemical transistors. *Flexible and Printed Electronics* **2020,** *5* (1), 013001.

169. West, S. M.; Tran, D. K.; Guo, J. J.; Chen, S. E.; Ginger, D. S.; Jenekhe, S. A., Phenazine-Substituted Poly(benzimidazobenzophenanthrolinedione): Electronic Structure, Thin Film Morphology, Electron Transport, and Mechanical Properties of an n-Type Semiconducting Ladder Polymer. *Macromolecules* **2023,** *56* (5), 2081-2091.

170. Zhang, Z. Q.; Fu, W. F.; Ding, H. H.; Ju, H. X.; Yan, K. R.; Zhang, X. Q.; Ding, F. Z.; Li, C. Z.; Chen, H. Z., Modulate Molecular Interaction between Hole Extraction Polymers and Lead Ions toward Hysteresis-Free and Efficient Perovskite Solar Cells. *Adv Mater Interfaces* **2018,** *5* (15), 1800090.

171. Stein, E.; Nahor, O.; Stolov, M.; Freger, V.; Petruta, I. M.; Mcculloch, I.; Frey, G. L., Ambipolar blend-based organic electrochemical transistors and inverters. *Nature communications* **2022,** *13* (1).

172. Rivnay, J.; Owens, R. M.; Malliaras, G. G., The Rise of Organic Bioelectronics. *Chem Mater* **2014,** *26* (1), 679-685.

173. Hidalgo Castillo, T. C.; Moser, M.; Cendra, C.; Nayak, P. D.; Salleo, A.; Mcculloch, I.; Inal, S., Simultaneous Performance and Stability Improvement of a p-Type Organic Electrochemical Transistor through Additives. *Chem Mater* **2022,** *34* (15), 6723-6733.

174. Schafer, E. A.; Wu, R.; Meli, D.; Tropp, J.; Moser, M.; Mcculloch, I.; Paulsen, B. D.; Rivnay, J., Sources and Mechanism of Degradation in p-Type Thiophene-Based Organic Electrochemical Transistors. *Acs Appl Electron Ma* **2022,** *4* (4), 1391-1404.

175. Wang, X.; Chen, K.; De Vasconcelos, L. S.; He, J.; Shin, Y. C.; Mei, J.; Zhao, K., Mechanical breathing in organic electrochromics. *Nature communications* **2020,** *11* (1).

176. Li, X.; Wang, X.; You, L.; Zhao, K.; Mei, J., Improving Electrochemical Cycling Stability of Conjugated Yellow-to-Transmissive Electrochromic Polymers by Regulating Effective Overpotentials. *Acs Mater Lett* **2022,** *4* (2), 336-342.

177. Zhang, S.; Ding, P.; Ruoko, T. P.; Wu, R.; Stoeckel, M. A.; Massetti, M.; Liu, T.; Vagin, M.; Meli, D.; Kroon, R.; Rivnay, J.; Fabiano, S., Toward Stable p‐Type Thiophene‐Based Organic Electrochemical Transistors. *Adv Funct Mater* **2023**.

178. Giovannitti, A.; Thorley, K. J.; Nielsen, C. B.; Li, J.; Donahue, M. J.; Malliaras, G. G.; Rivnay, J.; Mcculloch, I., Redox-Stability of Alkoxy-BDT Copolymers and their Use for Organic Bioelectronic Devices. *Adv Funct Mater* **2018,** *28* (17), 1706325.

179. Roberts, M. F.; Jenekhe, S. A., Lewis-Acid Coordination-Complexes of Polymers .3. Poly(Benzobisimidazobenzophenanthroline) Ladder and Semiladder Polymers. *Polymer* **1994,** *35* (20), 4313-4325.

180. Lu, Y.; Wang, J. Y.; Pei, J., Strategies To Enhance the Conductivity of n-Type Polymer Thermoelectric Materials. *Chem. Mater.* **2019,** *31* (17), 6412-6423.

181. Kline, R. J.; McGehee, M. D.; Kadnikova, E. N.; Liu, J. S.; Frechet, J. M. J.; Toney, M. F., Dependence of regioregular poly(3-hexylthiophene) film morphology and field-effect mobility on molecular weight. *Macromolecules* **2005,** *38* (8), 3312-3319.

182. Wenderott, J. K.; Dong, B. X.; Green, P. F., Morphological design strategies to tailor out-of-plane charge transport in conjugated polymer systems for device applications. *Phys. Chem. Chem. Phys.* **2021,** *23* (48), 27076-27102.

183. Nakano, K.; Kaji, Y.; Tajima, K., Highly Sensitive Evaluation of Density of States in Molecular Semiconductors by Photoelectron Yield Spectroscopy in Air. *ACS Appl. Mater. Interfaces* **2021,** *13*, 28574--28582.

184. Bssler, H.; Kroh, D.; Schauer, F.; Ndady, V.; Khler, A., Mapping the Density of States Distribution of Organic Semiconductors by Employing Energy Resolved–Electrochemical Impedance Spectroscopy. *Adv Funct Mater* **2021,** *31* (9), 2007738.

185. Hase, H.; Berteau-Rainville, M.; Charoughchi, S.; Orgiu, E.; Salzmann, I., Doping-related broadening of the density of states governs integer-charge transfer in P3HT. *Appl Phys Lett* **2021,** *118* (20), 203301.

186. Friedlein, J. T.; McLeod, R. R.; Rivnay, J., Device physics of organic electrochemical transistors. *Org Electron* **2018,** *63*, 398-414.

187. Paudel, P. R.; Tropp, J.; Kaphle, V.; Azoulay, J. D.; Lssem, B., Organic electrochemical transistors-from device models to a targeted design of materials. *J. Mater. Chem. C* **2021,** *9*, 9761--9790.

188. Lago, N.; Cester, A.; Wrachien, N.; Natali, M.; Quiroga, S. D.; Bonetti, S.; Barbato, M.; Rizzo, A.; Benvenuti, E.; Benfenati, V.; Muccini, M.; Toffanin, S.; Meneghesso, G., A physical-based equivalent circuit model for an organic/electrolyte interface. *Org Electron* **2016,** *35*, 176--185.

VITA

EDUCATION

2023 Ph.D. in Molecular Engineering: Data Science – University of Washington
Advisor: Prof. David S. Ginger

2016 B.S. in Macromolecular Science and Engineering – Fudan University, China
Advisor: Prof. Huisheng Peng

PUBLICATIONS

1. West, S.M., Tran, D.K., **Guo, J.**, Chen, S.E., Ginger, D.S. and Jenekhe, S.A. p-Type Semiconducting Ladder Poly(pyrrolobenzothiazine)s: Effects of N-Alkyl Side Chains on the Chain Conformation, Electronic Structure, and Charge Transport Properties. Submitted.
2. **Guo, J.**[*], Chen, S.E.[*], Giridharagopa, R., Bischak, C.G., Onorato, J.W., Yan, K., Shen, Z., Li, C.Z., Luscombe, C.K. and Ginger, D.S.Why accumulation mode organic electrochemical transistors turn off much faster than they turn on. Under Review.
3. West, S.M., Tran, D.K., **Guo, J.**, Chen, S.E., Ginger, D.S. and Jenekhe, S.A. Phenazine-Substituted Poly (benzimidazobenzophenanthrolinedione): Electronic Structure, Thin Film Morphology, Electron Transport, and Mechanical Properties of an n-Type Semiconducting Ladder Polymer, 2023. Macromolecules, 56(5), pp.2081-2091.
4. **Guo, J.**, Flagg, L., Tran, D., Chen, S., Li, R., Kolhe, N., Giridharagopal, R., Jenekhe, S.A., Richter, L.J. and Ginger, D. Hydration of a side-chain-free n-type ladder semiconducting polymer driven by electrochemical doping. 2023. Journal of the American Chemical Society, 145(3), pp.1866-1876.
5. Chen, S.E., Flagg, L.Q., Onorato, J.W., Richter, L.J., **Guo, J.**, Luscombe, C.K. and Ginger, D.S. Impact of varying side chain structure on organic electrochemical transistor performance: a series of oligoethylene glycol-substituted polythiophenes. 2022. Journal of Materials Chemistry A, 10(19), pp.10738-10749.
6. Giridharagopal, R., **Guo, J.**, Kong, J. and Ginger, D.S. Nanowire Architectures Improve Ion Uptake Kinetics in Conjugated Polymer Electrochemical Transistors. 2021. ACS Applied Materials & Interfaces, 13(29), pp.34616-34624.
7. Flagg, L.Q., Giridharagopal, R., **Guo, J.** and Ginger, D.S. Anion-dependent doping and charge transport in organic electrochemical transistors. 2018. Chemistry of Materials, 30(15), pp.5380-5389.